AN ABSTRACT OF THE THESIS OF

Thanat Jitpraphai for the degree of Doctor of Philosophy in Mechanical Engineering presented on July 19, 2001. Title: Lateral Pulse Jet Control of a Direct Fire Atmospheric Rocket Using an Inertial Measurement Unit Sensor System.

Redacted for Privacy

Abstract approved: _____

Mark F. Costello

Impact point dispersion of a direct fire rocket can be drastically reduced with a ring of appropriately sized lateral pulse jets coupled to a trajectory tracking flight control system. The system is shown to work well against uncertainty in the form of initial off-axis angular velocity perturbations as well as atmospheric winds. For an example case examined, dispersion was reduced by a factor of one hundred. Dispersion reduction and mean miss distance are strong functions of the number of individual pulse jets, the pulse jet impulse, and the trajectory tracking window size. Proper selection of these parameters for a particular rocket and launcher combination is required to achieve optimum dispersion reduction to the pulse jet control mechanism. For the lateral pulse jet control mechanism that falls into the category of an impulse control mechanism, the trajectory tracking flight control law provides better reduction in dispersion and mean miss distance than the proportional navigation guidance law especially when small number of individual pulse jets is used.

Estimation of body frame components of angular velocity and angular acceleration of a rigid body projectile undergoing general three-dimensional motion using linear acceleration measurements is considered. The results are comparable to those obtained from a conventional Inertial Measurement Unit (IMU) that composes of accelerometers and gyroscopes. From the study of the effect of sensor errors to the measurement and the control performance, the sensitivity of the

angular rate estimation to the sensor noise is a strong function of the constellation of these three accelerometers. When more than three point measurements are used, the most effective method to fuse data is with one cluster that contains all sensors. In the conventional IMU, the dispersion and miss distance are less sensitive to the errors from accelerometers than to the gyroscopes. The estimation of angular rates plays essential roles in the performance of the control system in the reduction of dispersion and miss distance. The use of many accelerometers does not guarantee to reduce the sensitivity to errors. The selection of constellation among accelerometers in the data fusion process must be carefully taken into account.

LATERAL PULSE JET CONTROL OF A DIRECT FIRE ATMOSPHERIC ROCKET USING AN INERTIAL MEASUREMENT UNIT SENSOR SYSTEM

By

Thanat Jitpraphai

A THESIS

submitted to

Oregon State University

in partial fulfillment of
the requirements for the
degree of

Doctor of Philosophy

Presented July 19, 2001

Commencement June 2002

Doctor of Philosophy thesis of Thanat Jitpraphai presented on July 19, 2001.

APPROVED:

Redacted for Privacy

Major Professor, representing Mechanical Engineering

Redacted for Privacy

Chair of Department of Mechanical Engineering

Redacted for Privacy

Dean of the Graduate School

I understand that my thesis will become part of the permanent collection of Oregon State University libraries. My signature below authorizes release of my thesis to any reader upon request.

Redacted for Privacy

Thanat Jitpraphai, Author

ACKNOWLEDGEMENT

I would like to express my sincere gratitude to Dr.Mark F. Costello for his guidance and support during my graduate study. I would also like to thank Dr.Swavik A.Spiewak for his support and advice. Thank my graduate committee for the guidance in my degree pursuing. Thank the U.S.Army Research Laboratory at Aberdeen Proving Ground for the support of this research and the Department of Mechanical Engineering at OSU for providing the facilities. Thanks to all my friends in research groups and in Mechanical Engineering for their help.

I would like to thank sincerely to my parents, Dr.Phaibul and Dr.Chattaya Jitpraphai, as well as my brothers, Peera and Siros, for their encouragement and support for my study. I would like to thank to my wife, Dr.Waranush (Sorasuchart) Jitpraphai, for her care, love, and support in every aspect.

TABLE OF CONTENTS

Page

1. INTRODUCTION 1

2. LITERATURE REVIEW 4

   2.1 Missile Control Systems 4

   2.2 Guidance Systems 6

   2.3 Determination of Angular Velocity and Angular Acceleration 8

3. ROCKET DYNAMIC MODEL 10

   3.1 Coordinate Systems 10

   3.2 Euler Angle Transformation 10

   3.3 Direct Fire Rocket Dynamic Model 12

      3.3.1 Weight Force 14
      3.3.2 Aerodynamic Forces and Moments 15
      3.3.3 Main Rocket Motor Thrust Forces and Moments 16
      3.3.4 Lateral Pulse Jet Forces and Moments 17

4. INERTIAL MEASUREMENT UNIT DYNAMIC MODEL 19

   4.1 Conventional Acceleration and Angular Velocity Measurement 21

   4.2 Unconventional Acceleration and Angular Velocity Measurement. 27

      4.2.1 Three Tri-axial Accelerometer Algorithm for Determining Angular Velocity and Angular Acceleration 28
      4.2.2 More Than Three Triaxial Accelerometers Clusters for Determining Angular Velocity and Angular Acceleration... 32
      4.2.3 Algebraic Sign Determination ..... .33

   4.3 Measurement Error Sensitivity Analysis 35

   4.4 Skin Mounted Triaxial Acceleration Measurement Sensor Fusion.. 54

TABLE OF CONTENTS (Continued)

Page

5. LATERAL PULSE JET CONTROL LAWS 66

5.1 Trajectory Tracking Flight Control System 66

5.1.1 Off-axis Trajectory Error 67
5.1.2 Control Firing Logic 68

5.2 Parabolic Proportional Navigation Guidance Law 70

5.2.1 Horizontal Plane Guidance Law 71
5.2.2 Vertical Plane Guidance Law 75

5.3 Comparison of Control Laws 81

6. PARAMETRIC STUDY OF CONTROL MECHANISM AND EFFECT OF SENSOR ERROR 92

6.1 Parametric Trade Study of Control Mechanism 92

6.2 Comparison of Control Algorithms 104

6.3 Effect of Sensor Errors in Control Performance 106

6.3.1 Sensor Errors in Conventional IMU 106
6.3.2 Sensor Errors in the Unconventional IMU Using Three Triaxial Accelerometer 114
6.3.3 Sensor Errors in the Unconventional IMU Using Skin Mounted Sensor Fusion Algorithm 118

7. CONCLUSIONS 122

7.1 Conclusions 122

7.2 Recommendations for the Future Research 124

BIBLIOGRAPHY 125

LIST OF FIGURES

Figure — Page

1.1 Configuration of a direct fire rocket with lateral pulse jets and accelerometer-based IMU..... 2

3.1 Sequence of Euler's Angles Transformation..... 11

3.2 Schematic of a Direct Fire Rocket with a Lateral Pulse Jets..... 12

4.1 Schematic Diagram of IMU Mounted in the Rocket..... 19

4.2 General Sensor Configuration..... 28

4.3 Computational Plane Geometry..... 29

4.4 Configuration L..... 38

4.5 Configuration T..... 39

4.6 Configuration O..... 40

4.7 Configuration L Error Sensitivity Ratio versus Roll Rate and Sensor Constellation Angle (q = 0.0001 r/s, r = 0.0001 r/s)..... 44

4.8 Configuration L Error Sensitivity Ratio versus Roll Rate and Sensor Constellation Angle (q = 1 r/s, r = 1 r/s)..... 45

4.9 Configuration L Error Sensitivity Ratio versus Roll Rate and Sensor Constellation Angle (q = 0 r/s, r = 1.414 r/s)..... 46

4.10 Configuration T Error Sensitivity Ratio versus Roll Rate and Sensor Constellation Angle (q = 0.0001 r/s, r = 0.0001 r/s)..... 47

4.11 Configuration T Error Sensitivity Ratio versus Roll Rate and Sensor Constellation Angle (q = 1 r/s, r = 1 r/s)..... 48

LIST OF FIGURES (Continued)

Figure — Page

4.12 Configuration T Error Sensitivity Ratio versus Roll Rate and Sensor Constellation Angle (q = 0 r/s, r = 1.414 r/s)..... 49

4.13 Configuration O Error Sensitivity Ratio versus Roll Rate and Sensor Constellation Angle (q = 0.0001 r/s, r = 0.0001 r/s)..... 50

4.14 Configuration O Error Sensitivity Ratio versus Roll Rate and Sensor Constellation Angle (q = 1 r/s, r = 1 r/s)..... 51

4.15 Configuration O Error Sensitivity Ratio versus Roll Rate and Sensor Constellation Angle (q = 0 r/s, r = 1.414 r/s)..... 52

4.16 Error Sensitivity of Yaw Rate versus Pitch and Yaw Rate for θ = 0, 45, 90°..... 53

4.17 Acceleration Measurement Sensor Configuration..... 54

4.18 Actual and Estimated Roll Rate versus Time..... 56

4.19 Actual and Estimated Pitch Rate versus Time..... 57

4.20 Actual and Estimated Yaw Rate versus Time..... 58

4.21 Actual and Estimated Roll Acceleration versus Time..... 59

4.22 Actual and Estimated Pitch Acceleration versus Time..... 60

4.23 Actual and Estimated Yaw Acceleration versus Time..... 61

4.24 Average Error Magnitude versus Sensor Configuration..... 63

4.25 Average Error Magnitude versus Sensor Fusion Technique..... 64

4.26 Average Error Magnitude versus Quantization Level..... 65

5.1 Trajectory Tracking Flight Control System..... 67

LIST OF FIGURES (Continued)

Figure Page

5.2 i^{th} Individual Lateral Pulse Jet Firing Logic..... 69

5.3 Line of Sight Frame Configuration..... 71

5.4 Proportional Navigation Guidance Law for the Horizontal Flight Control..... 74

5.5 Parabolic trajectory in the LOS frame..... 75

5.6 Parabolic Proportional Navigation Guidance Law for the Vertical Control.... 77

5.7 i^{th} Individual Lateral Pulse Jet Firing Logic..... 80

5.8 Altitude versus Range..... 83

5.9 Cross Range versus Range..... 84

5.10 Trajectory Tracking Error versus Time of the Trajectory Tracking Controlled Rocket..... 85

5.11 Trajectory Tracking Error versus Time of the Proportional Navigation Guidance Controlled Rocket..... 86

5.12 Pulse Jet Firing Time..... 87

5.13 Roll Angle versus Time..... 88

5.14 Euler Pitch Angle versus Time..... 89

5.15 Euler Yaw Angle versus Time..... 90

5.16 Aerodynamic Angle of Attack versus Time..... 91

6.1 Impact Point Dispersion (Perturbed Initial Pitch and Yaw Rate)..... 94

6.2 Dispersion Radius and Mean of Miss Distance versus Number of Pulse Jets and Pulse Jets Impulse for Trajectory Tracking Window Size of 0.3 m..... 96

LIST OF FIGURES (Continued)

Figure Page

6.3 Dispersion Radius and Mean of Miss Distance versus Number of Pulse Jets and Pulse Jets Impulse for Trajectory Tracking Window Size of 1.5 m..... 97

6.4 Dispersion Radius and Mean of Miss Distance versus Number of Pulse Jets and Pulse Jets Impulse for Trajectory Tracking Window Size of 3.0 m..... 98

6.5 Dispersion Radius versus Number of Pulse Jets and Total Ring Impulse (Trajectory Tracking Window Size = 1.5 m)..... 100

6.6 Dispersion Radius versus Number of Pulse Jets and Trajectory Tracking Window Size (Total Ring Impulse = 80 N-s)..... 101

6.7 Dispersion Radius versus Atmospheric Wind Direction for the Uncontrolled Rocket (Atmospheric Wind Speed = 7.6 m/s, Number of Pulse Jets = 32, Pulse Jet Impulse = 20 N-s, Trajectory Tracking Window Size = 1.5 m).... 102

6.8 Dispersion Radius versus Atmospheric Wind Direction for the Controlled Rocket (Atmospheric Wind Speed = 7.6 m/s, Number of Pulse Jets = 32, Pulse Jet Impulse = 20 N-s, Trajectory Tracking Window Size = 1.5 m).... 103

6.9 Comparison of Control Navigation System..... 105

6.10 Effect of Accelerometer Noises on Conventional IMU..... 107

6.11 Effect of Accelerometer Bias on Conventional IMU..... 108

6.12 Effect of Accelerometer Cross Axis Sensitivity on Conventional IMU..... 109

6.13 Effect of Gyroscope Noises on Conventional IMU..... 111

6.14 Effect of Gyroscope Bias on Conventional IMU..... 112

6.15 Effect of Gyroscope Cross Axis Sensitivity on Conventional IMU.....113

6.16 Effect of Accelerometer Noises on Three Triaxial Accelerometer Method..115

LIST OF FIGURES (Continued)

Figure Page

6.17 Effect of Accelerometer Bias on Three Triaxial Accelerometer Method..... 116

6.18 Effect of Accelerometer Cross Axis Sensitivity on Three Triaxial Accelerometer Method..... 117

6.19 Effect of Accelerometer Noises on Skin Mounted Sensor Fusion Method.. 119

6.20 Effect of Accelerometer Bias on Skin Mounted Sensor Fusion Method..... 120

6.21 Effect of Accelerometer Cross Axis Sensitivity on Skin Mounted Sensor Fusion Method..... 121

LIST OF TABLES

Table Page

4.1 Error sensitivity for L configuration..... 42

4.2 Error sensitivity for T configuration..... 42

4.3 Error sensitivity for O configuration..... 43

NOMENCLATURE

$[I]$ = Inertia matrix with respected to the B frame.

$[R_1(\psi)], [R_2(\theta)], [R_3(\phi)]$ = Single axis rotation matrices.

$[T_{Ai}]$ = Body to sensor transformation matrix of the i[th] accelerometer.

$[T_{Gi}]$ = Body to sensor transformation matrix of the i[th] gyroscope.

$[T_I^B]$ = Inertial to body transformation matrix.

$[T_L^I]$ = Line of sight to inertial reference frame transformation matrix.

A = Relative acceleration matrix.

A_C = Command acceleration.

A_{CL} = Acceleration command vector in the line of sight frame.

$A_{X_{CB}}, A_{Y_{CB}}, A_{Z_{CB}}$ = Components of command acceleration in the B frame.

A_{YC}, A_{ZC} = Horizontal and vertical command accelerations.

$\hat{a}_{IMU/_I}$ = IMU reading of acceleration of point S.

a_{iX}, a_{iY}, a_{iZ} = Components of acceleration of the i[th] accelerometer in the i[th] sensor frame.

a_{iX}^B = Sensor bias of the i[th] accelerometer.

a_{iX}^N = Sensor noise of the i[th] accelerometer.

$\tilde{a}_{iX}$ = $\vec{I}_{Ai}$ component of acceleration of the i[th] accelerometer.

$\tilde{a}_{X_i}, \tilde{a}_{Y_i}, \tilde{a}_{Z_i}$ = Components of acceleration of the i[th] accelerometer in the computational frame.

$\hat{a}_{X_{S/I}}, \hat{a}_{Y_{S/I}}, \hat{a}_{Z_{S/I}}$ = Components of $\hat{a}_{IMU/I}$ in the B frame.

B = Body reference frame.

C = Computational frame.

C_{DD} = Fin cant roll moment aerodynamic coefficient.

C_{iY}^{A}, C_{iZ}^{A} = $\vec{J}_{Ai}$ and $\vec{K}_{Ai}$ cross axis sensitivity of the ith accelerometer.

C_{iY}^{G}, C_{iZ}^{G} = $\vec{J}_{Ai}$ and $\vec{K}_{Ai}$ cross axis sensitivity of the ith gyroscope.

C_{LP} = Roll damping aerodynamic coefficient.

C_{MQ} = Pitch damping aerodynamic coefficient.

C_{NA} = Normal force aerodynamic coefficient.

C_{X0} = Zero yaw axial force aerodynamic coefficient.

C_{X2} = Yaw axial force aerodynamic coefficient.

D = Rocket reference diameter.

e_{THRES} = Trajectory tracking window size.

e_x, e_y, e_z = Components of trajectory error in the B frame.

G = Sensitivity matrix.

g = Gravitational constant.

I = Inertial reference frame.

$\vec{I}_1, \vec{J}_1, \vec{K}_1$ = Unit vectors of the intermediate frame 1.

$\vec{I}_2, \vec{J}_2, \vec{K}_2$ = Unit vectors of the intermediate frame 2.

$\vec{I}_{Ai}, \vec{J}_{Ai}, \vec{K}_{Ai}$ = Unit vectors of the ith accelerometer frame.

$\bar{I}_B, \bar{J}_B, \bar{K}_B$ = Unit vectors of the body reference frame.

$\bar{I}_C, \bar{J}_C, \bar{K}_C$ = Unit vectors of the computational plane.

$\bar{I}_{Gi}, \bar{J}_{Gi}, \bar{K}_{Gi}$ = Unit vectors of the ith gyroscope frame.

$\bar{I}_I, \bar{J}_I, \bar{K}_I$ = Unit vectors of the *I* frame.

$\bar{I}_T, \bar{J}_T, \bar{K}_T$ = Unit vectors of the target frame.

K_1, K_2 = Parabolic constants.

L, M, N = Total applied moments about rocket mass center.
L_J, M_J, N_J = Moments from lateral pulse jet forces.

L_{UA}, M_{UA}, N_{UA} = Moments from unsteady air loads.

L_R, M_R, N_R = Moments from main rocket thrusts.

L_{SA}, M_{SA}, N_{SA} = Moments from steady air loads.

l = Number of cluster groups of accelerometers in the sensor fusion method.

M = Matrix contains angular velocities and angular acceleration in the computational plane.

m = Mass of the rocket.

N' = Proportional navigation constant.

n_J = Number of individual lateral pulse jets.

$n_{RXi}, n_{RYi}, n_{RZi}$ = ith main rocket motor direction cosines in the *B* frame.

p, q, r = Components of the angular velocity vector of the projectile in the *B* frame.

$\tilde{p}, \tilde{q}, \tilde{r}$ = Components of estimated angular rate in the computational plane.

$\hat{p}, \hat{q}, \hat{r}$ = Components of IMU reading of rocket angular rate in the B frame.

R = Matrix contains relative position of accelerometers in the computational plane.

$R_{P \to T}$ = Magnitude of the distance from the projectile to the target.

$\vec{r}_{T/I}, \vec{r}_{P/I}$ = Positions of the target and the projectile in the I frame.

$\vec{r}_{\varphi \to \beta}$ = Distance vector from φ to β in B frame.

S = Location of inertial measurement unit (IMU).

T = $\dot{\gamma}$ time constant.

T_{J_i} = i^{th} lateral pulse jet thrust.

T_{R_i} = i^{th} main rocket motor thrust.

t^* = Time of the most recent pulse jet firing.

U = Vector contains components of input acceleration in accelerometers.

u, v, w = Components of the velocity vector of the mass center of the projectile body in the B frame.

u_A, v_A, w_A = Components of the relative aerodynamic velocity of the mass center of the projectile expressed in the B frame.

u_L, v_L, w_L = Components of rocket velocity in the line of sight frame.

$\hat{u}_{S/I}, \hat{v}_{S/I}, \hat{w}_{S/I}$ = Estimated velocity of the rocket at IMU location in the B frame.

V_D = Magnitude of the projectile velocity on the line of sight frame.

X, Y, Z = Total applied force components in the body reference frame.

X_A, Y_A, Z_A = Air loads.

X_J, Y_J, Z_J = Lateral pulse jet force.

X_R, Y_R, Z_R = Main rocket thrust force.

X_W, Y_W, Z_W = Rocket weight.

x, y, z = Components of the position vector of center of mass of the projectile body in the I frame.

$\tilde{x}_1, \tilde{x}_2, \tilde{y}$ = Geometric distance of the computational plane.

$\hat{x}, \hat{y}, \hat{z}$ = Estimated position of the rocket IMU in the inertial reference frame.

x_C, y_C, z_C = Components of the command trajectory in the I frame.

$\hat{x}_P, \hat{z}_P, \hat{z}_T$ = Components of the projectile position and the target position that are defined in a target frame.

x_T, y_T, z_T = Components of $\vec{r}_{T/I}$.

Y = Output vector contains estimated angular rate and angular acceleration.

V_A = Magnitude of the relative aerodynamic velocity vector of the mass center of the projectile.

V_C = Rocket closing velocity.

V_{MW}, σ_{MW} = Magnitude and wind factor of the mean atmospheric wind expressed in the I frame.

Δ_{J_i} = Pulse jet firing duration.

Δt_{THRES} = Minimum required elapsed time between successive pulse jet firing.

Γ_e, γ_e = Magnitude and phase angle of the error in the off-axis plane of the rocket.

φ, β, χ = Locations of accelerometers in the body.

$\vec{\alpha}_{B/I}$ = Angular acceleration of the body reference frame with respect to the inertial reference frame.

$\tilde{\alpha}_x, \tilde{\alpha}_y, \tilde{\alpha}_z$ = Components of estimated angular acceleration in the computational plane.

δ_{THRES} = Pulse jet angle threshold.

ϕ, θ, ψ = Euler roll, pitch and yaw angles of the projectile.

$\hat{\phi}, \hat{\theta}, \hat{\psi}$ = Estimated Euler roll, pitch, and yaw angles of the rocket.

ϕ_{J_i} = Angle between $\bar{J}_B$ and the ith pulse jet.

γ = Flight path angle of the projectile velocity in the line of sight frame.

γ_D = Desired flight path angle.

γ_F = Terminal flight path angle.

$\lambda, \dot{\lambda}$ = Line of sight angle and its time derivative.

ρ = Air density.

τ = Acceleration command time constant.

$\vec{\omega}_{B/I}$ = Angular velocity of the body reference frame with respect to the *I* frame.

$\omega_{iX}, \omega_{iY}, \omega_{iZ}$ = Components of angular velocity of the ith gyroscope in the ith sensor frame.

$\tilde{\omega}_{iX}$ = $\bar{I}_{Ai}$ component of angular velocity of the ith gyroscope.

ω_{iX}^{B} = Sensor bias of the ith gyroscope.

ω_{iX}^{N} = Sensor noise of the ith gyroscope.

LATERAL PULSE JET CONTROL OF A DIRECT FIRE ATMOSPHERIC ROCKET USING AN INERTIAL MEASUREMENT UNIT SENSOR SYSTEM

CHAPTER 1
INTRODUCTION

Direct fire rockets are categorized as missiles that are directed at a target that is visible to the firing unit using the target as a point of aim. These weapons are relatively inexpensive and are launched from fixed and rotary wing aircraft as well as ground based launchers. Direct fire rockets are commonly used on the battlefield. Unfortunately these projectiles exhibit high impact point dispersion, even at relatively short range, and as such have been employed as area weapons. Because direct fire rockets exit the launcher with low velocity, any aerodynamic disturbances presented to the rocket near the launcher create relatively large angles of attack, leading to large aerodynamic jump and increased target dispersion. Furthermore, main rocket motor thrust during the initial portion of flight tends to amplify the effect of initial transverse and angular velocity perturbations on dispersion. The integrated effect over the trajectory of initial disturbances as the rocket enters atmospheric flight and high sensitivity to atmospheric disturbances all lead to large impact point dispersion.

Increased design requirements being placed on direct fire ammunition, including direct fire rockets, call for surgical removal of select targets on the battlefield. Economic realities now stipulate that improved capability be delivered at reduced unit cost. Small, rugged, and inexpensive microelectromechanical sensors (MEMS) coupled to a suitable and inexpensive control mechanism offer the potential to meet these increasingly stringent design requirements. A potential control mechanism that is small, durable, and can be located in close proximity to

the sensor suite is a lateral pulse jet ring mounted forward on the rocket body. The pulse jet ring consists of a finite number of individual pulse jets. Each pulse jet on the ring imparts a single, short duration, large force to the rocket in the plane normal to the rocket axis of symmetry. The diagram of the described potential improved rocket is shown in Figure 1.1.

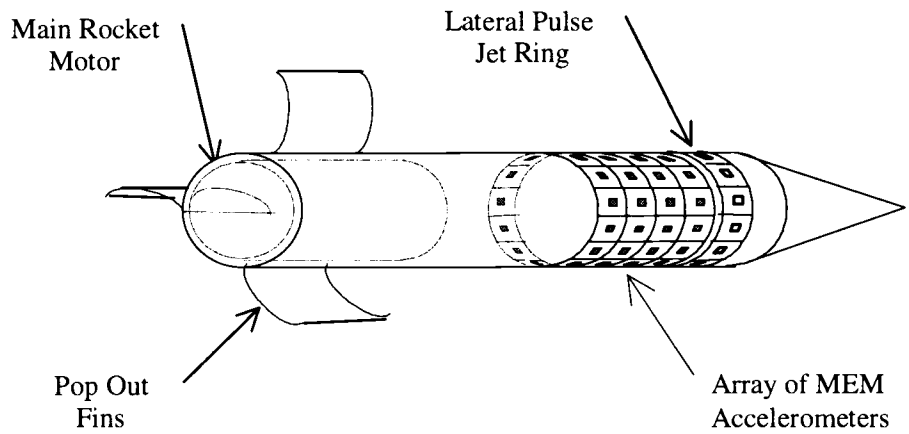

Figure 1.1 Configuration of a direct fire rocket with lateral pulse jets and accelerometer-based IMU.

An essential factor in realization of a flight control system is accuracy of the sensor system. Flight control systems in guided missiles incorporate an Inertial Navigation System (INS) or Inertial Measurement Unit (IMU) to estimate position and orientation of the missile over the engagement trajectory. Conventional accelerometers and rate gyroscopes coupled with associated signal processing make current commercial IMU systems too costly for application to future inexpensive actively controlled direct fire rockets. However, recent development of small and rugged microelectromechanical sensors (MEMS) offer the potential solution to

employ active flight control systems onboard medium and even small caliber projectiles in a fiscally acceptable manner.

This thesis develops a flight control system for a direct fire rocket equipped with a ring of lateral pulse jets and an IMU. The works seeks to reduce dispersion of an atmospheric rocket using a flight control system specialized to a latarel pulse jet control mechanism. Pulse jet firing logic is engaged when the tracking errors exceed a specific threshold. Parametric trade studies that consider the effect of the number of pulse jets, pulse jet impulse, and tracking window size on impact point dispersion using different guidance schemes are reported.

The thesis is organized as follows. Chapter 2 provides a review of relevant literature. The development of a mathematical model for a direct fire rocket is described in Chapter 3. This model is deployed in all simulation studies in this thesis. The model of a traditional IMU is described in Chapter 4. Also, Chapter 4 describes a new IMU concept that consists of a set of MEMs linear accelerometers and no angular rate sensors. Chapter 5 develops a trajectory tracking flight control system for the lateral pulse jet controlled rocket. Results using the proposed control system are compared to a proportional navigation guidance control. Parametric trade studies for the lateral pulse jet control system are reported in Chapter 6. Chapter 7 provides the conclusions to the thesis.

CHAPTER 2
LITERATURE REVIEW

2.1 Missile Control Systems

Various control mechanisms have been developed for tactical missiles. Example systems include aerodynamic control, thrust vector control, and gas jet injection control.

Standard aerodynamic control achieves required maneuver ability through fin movement. Fin rotation induces aerodynamic lift to the body, causing a change in the total body force vector (Garnell, 1980). Limitations for fin actuator control of a direct fire rocket include the response time due to delay between the command and execution, as well as maneuverability when dynamic pressure is low (Champigny and Lakau, 1994). A complicated mechanism is also required to stabilize the roll channel before correction from the fins can be acheived (Blakelock, 1991).

Another control mechanism is thrust vector control in which the direction of the efflux from the propulsion motor is altered. The mechanism behind the thrust direction controller can be a gimbaled motor, a flexible nozzle, moving vans, or gas injection into the motor venturi (Gilman, 1971; Garnell, 1980). This system is attractive in its ability to rapidly turnover which is required in some applications such as in a vertical launch from the ground or a submarine. The thrust vector control system is also insensitive to aerodynamic pressure. However its high cost and complexity are severe limitations, particular for a low cost direct fire rocket.

Lateral pulse jet provides another possible solution as a direct fire rocket control mechanism. This control mechanism is attractive due to low dynamic pressure maneuverability. The lateral pulse jet mechanism consists of a ring of small thrusters mounted near the nose of the rocket. Each thruster on the ring imparts a single, short duration, large lateral force to the rocket. Design of a lateral pulse jet flight control system simplifies to determining the firing time for each thruster. A significant body of literature has amassed in the area of aerodynamics of a gas jet injected through the side wall of the missile to the high speed external air flow. The force amplification factor is defined as the upstream interaction force plus the jet thrust normalized by the vacuum thrust of a sonic jet (Spaid, 1975). The force amplification factor is a function of Reynolds and Mach number as well as the body angle of attack. Jet interaction effect are summarized by Champigny and Lakau (1994). An experimental study of a lateral sonic gas jet into a Mach 13 airstream was conducted by Reiecke (1975). The results showed that the jet behaved as a point source and that the nozzle cross-section shape was unimportant. Spaid and Zukoski (1968) conducted an experiment on sonic jet interaction of a gas jet through a transverse slot nozzle into a supersonic external flow (Spaid and Zukoski, 1968). The study concludes that the amplification factor is relatively insensitive to variations in the external flow Mach number and variations in injectant gas properties. It was later confirmed by the study in two dimensional jet interaction at high Reynolds and Mach numbers (Spaid 1975). An experiment by Gilman (1971) indicated that the force amplification factor depends on the missile configuration. The results show that a fin configuration rocket has higher amplification factor than that of the body without fins (Gilman, 1971). Srivastava (1997) used computational fluid dynamics (CFD) to study of lateral jet interactions in variety of conditions including Mach number, angle of attack, and missile configuration. The results showed good agreement between computational and experimental results for the normal force and pitching moment of a lateral jet on a supersonic missile. Later, Srivastava (1997, 1998, 1999) showed that lateral thrust

jet effectiveness diminished as jet thrust is gradually rolled toward the windward side of the missile (Srivastava, 1997, 1998, 1999). Brandeis and Gill (1998) showed the effect of missile configuration on the relationships between the force amplification factor, Mach number and angle of attack. This investigation showed that jet force amplification is strongly dependant on the size and location of lifting surfaces of the missile and that jet force amplification is inversely proportional to jet pressure (Brandeis and Gill, 1998). The effect of the angle of attack on the force amplification factor at various Mach numbers in is compared with the experiment by Kurita, Okada, and Nakamura (2001). It was found that at high angle of attack there is the possibility that the pressure decreases largely due to vortices produced behind the jet separation shock (Kurita, Okada, and Nakamura, 2001).

The use of lateral pulse jets to improve target dispersion performance has been investigated by Harkins and Brown (1999). They used a set of lateral pulse jets to eliminate the off-axis angular rate of the projectile just after exiting the launcher. For the notional concepts considered, dispersion was reduced by a factor of four (Harkins and Brown, 1999). Lateral pulse jet is attractive in its simplicity for installation and deployment. In this thesis, a simplified model of the pulse jet is considered.

2.2 Guidance Systems

Missile guidance technology has been long developed but mostly for missiles that require commanded acceleration for feedback forces and moments. Such systems are typically configured with aerodynamic fins or with thrust vector control. Two classes of algorithms have emerged, Bank-to-Turn (BTT), and Skid-to-Turn (STT) (Redriquez and Sonne, 1997). The most widely used algorithms for generating acceleration commands is proportional navigation guidance (PNG). This algorithm determines commanded acceleration for the missile in proportion to

target maneuver acceleration. It requires knowledge of the position between the missile and the target. Line of sight (LOS) is formed between these two points implying desired direction of the missile. Rate of change of the LOS frame provides command acceleration that creates feedback to the fin actuator (Zarchan, 1990). Many improvements in this method have been developed including switching of guidance to account for nonlinearity of the system and variability of target maneuver (Shin, 1997; Kuo and Chiou, 2000; Liaw, Liang, and Cheng, 2000). Other missile guidance system that can be an alternative to the proportional navigation system is the use of H_∞ controller design (Wang, Xie, and Zhong, 1997). The lateral pulse jet control mechanism falls into the category of an impulse control mechanism. This is in contrast to the vast majority of flight control mechanisms, such as for example, deflecting fins that continuously generate a control force to track a specific trajectory. While highly developed techniques such as Proportional Navigation Guidance (PNG) are well known in missile guidance where continuous control is available, few have focused attention on the use of impulse control mechanisms, particularly for direct fire rockets. Harkins and Brown (1999) developed a simple control scheme to reduce dispersion of a direct fire rocket which only required angular rate feedback. For the example configuration considered, impact point dispersion was reduced by a factor of four (Harkins and Brown, 1999). Jitpraphai and Costello (2001) studied the same problem using a trajectory tracking flight control law which required an Inertial Measurement Unit (IMU). Rocket dispersion was reduced by as much as a factor of 100, depending on the lateral pulse jet configuration (Jitpraphai and Costello, 2001). Calise and El-Shirbiny (2001) developed a lateral pulse jet control law for a spin stabilized gun launched projectile based on proportional navigation guidance, but modified to account for trajectory bending due to gravity (Calise and El-Shirbiny, 2001).

2.3 Determination of Angular Velocity and Angular Acceleration

The flight control system requires knowledge of rocket position and orientation that is determined on the projectile using the IMU. The computational algorithm in the IMU demands linear acceleration as well as angular rates as input. A wide variety of sensor technologies are used to sense these quantities such as, linear accelerometers, magnetic roll sensors, tuning fork gyroscopes, magnetohydrodynamic angular rate sensors, and diaphragm strain gage surface pressure sensors, to name a few (Davis, 1996; David, Harlems, and Burkey, 1997; D'Amico, 1998). Several studies have been conducted regarding potential performance improvements in large, medium, and small caliber projectile performance that utilize some form of an active flight control system (Costello, 1999; Costello and Agarwalla, 2000; Harkins and Brown, 1999; Harkins, 1999). The potential performance enhancements are significant. However, for practical design implementation, the sensors must be highly cost competitive so that the sensor suite does not dominate the cost of the entire projectile, which is of course a one-time use item. While MEMS technology is rapidly changing with innovative sensor configurations regularly entering the market, currently linear accelerometers are by far the least expensive and most developed devices.

Rigid body kinematics provide a link between linear acceleration, angular velocity, and angular acceleration that can be exploited in an IMU. Since angular velocity and angular acceleration are body properties and linear acceleration is a point property, the linear acceleration at several points on a rigid body can be used to compute the angular velocity and acceleration of the body (Ginsberg, 1995). Several algorithms have been developed for different applications. For example, Padgaonkar, Krieger, and King (1975) used nine single axis acceleration measurements at four different non-coplanar points to compute angular velocity and acceleration components (Padgaonkar, Krieger, and King, 1975). Merhav described the possibility of using triaxial accelerometers to construct a low cost

IMU that can function like a more expensive INS (Merhav, 1982). Errors due to sampling, accelerometer noise, nonlinearity, misalignment, and cross-axis sensitivity can be avoided by using signal separation technique. Nusholtz (1993) proposed a method based on spherical geometric analysis. Using the properties of acceleration components on a sphere the method determines both angular velocity and angular acceleration with three triaxial accelerometers (Nusholtz, 1993). A methodology using six linear accelerometers in the determination of an angular acceleration is developed by Chen, Lee, and Debra, (1992). A cube construction of these accelerometers where sensors are placed at the center of each face of the cube is used. The results are comparable to the traditional method using nine accelerometers. Genin, Hong, and Xu (1997) proposed an alternative configuration, using an array of nine linear accelerometers (Genin, Hong, and Xu, 1997). The study emphasized using the invertiblity of a matrix of sensor locations to prove that the minimum number of nine sensors is necessary. Harkins and Brown (1998) explored the use of four single axis linear accelerometers aligned with the body axis of a projectile to compute angular velocity and acceleration (Harkins and Brown, 1998). When applied to a direct fire atmospheric rocket, digital accelerometer output at 16-bit resolution was necessary. Costello and Jitpraphai (2000) developed a method using clusters of three, triaxial axis accelerometers to compute the angular rates and accelerations. In contrast to those algorithms that require placements of sensors in specific configuration, this proposed method utilizes a general non-coplanar placement of 3 triaxial accelerometers to estimate the angular rate and acceleration (Costello and Jitpraphai, 2001).

CHAPTER 3
ROCKET DYNAMIC MODEL

3.1 Coordinate Systems

Two coordinate systems are defined in the description of the rocket dynamic model. The inertial reference frame $(\bar{I}_I, \bar{J}_I, \bar{K}_I)$ is defined to be fixed to the surface of the Earth. The unit vector $\bar{I}_I$ lies in the x direction and points downrange and $\bar{J}_I$ lies in the y direction and points cross range. A plane formed by the $\bar{I}_I$ and $\bar{J}_I$ vectors are parallel to the Earth's surface. The unit vector $\bar{K}_I$ is perpendicular to this plane and points down into the ground. Since most atmospheric rockets spin rapidly during flight, a rotating frame is defined to be fixed to the rocket body. A body reference frame $(\bar{I}_B, \bar{J}_B, \bar{K}_B)$ is defined such that its origin is located at the mass center of the rocket and the $\bar{I}_B$ axis is directed along the rocket's axis of symmetry and points toward the nose. This body reference frame rotates with the rocket. When all body orientation angles equal zero, the body and inertial reference frame unit vectors are aligned.

3.2 Euler Angle Transformation

The relationships between the inertial reference frame and the body reference frame unit vectors is described using the aerospace convention for defining Euler angles (Etkin, 1972; Ginsberg, 1995). It proceeds with sequences of body-fixed rotations as shown in Figure 3.1.

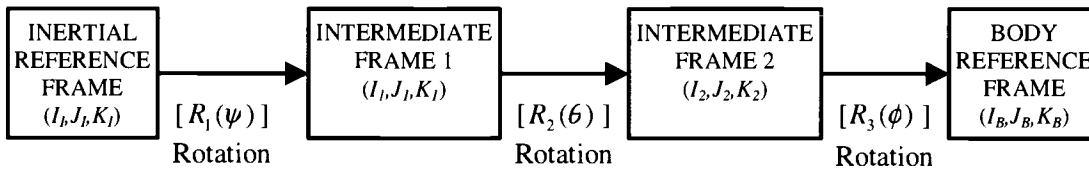

Figure 3.1 Sequence of Euler's Angles Transformation.

The transformation from the inertial reference frame to intermediate frame 1 $(\bar{I}_1, \bar{J}_1, \bar{K}_1)$ is defined by Equation (3.1).

$$\begin{Bmatrix} \bar{I}_1 \\ \bar{J}_1 \\ \bar{K}_1 \end{Bmatrix} = [R_1(\psi)] \begin{Bmatrix} \bar{I}_I \\ \bar{J}_I \\ \bar{K}_I \end{Bmatrix} = \begin{bmatrix} c_\psi & s_\psi & 0 \\ -s_\psi & c_\psi & 0 \\ 0 & 0 & 1 \end{bmatrix} \begin{Bmatrix} \bar{I}_I \\ \bar{J}_I \\ \bar{K}_I \end{Bmatrix} \tag{3.1}$$

In Equation (3.1), short hand notation for trigonometric sine and cosine is employed: $c_\psi \equiv \cos(\psi), s_\psi \equiv \sin(\psi)$. The rotation matrices $R_2(\theta)$ and $R_3(\phi)$ are the transformation from intermediate frame 1 to intermediate frame 2 and from intermediate frame 2 to body fixed reference frame, respectively. These transformations are defined by Equation (3.2) and (3.3).

$$\begin{Bmatrix} \bar{I}_2 \\ \bar{J}_2 \\ \bar{K}_2 \end{Bmatrix} = [R_2(\theta)] \begin{Bmatrix} \bar{I}_1 \\ \bar{J}_1 \\ \bar{K}_1 \end{Bmatrix} = \begin{bmatrix} c_\theta & 0 & -s_\theta \\ 0 & 1 & 0 \\ s_\theta & 0 & c_\theta \end{bmatrix} \begin{Bmatrix} \bar{I}_1 \\ \bar{J}_1 \\ \bar{K}_1 \end{Bmatrix} \tag{3.2}$$

$$\begin{Bmatrix} \bar{I}_B \\ \bar{J}_B \\ \bar{K}_B \end{Bmatrix} = [R_3(\phi)] \begin{Bmatrix} \bar{I}_2 \\ \bar{J}_2 \\ \bar{K}_2 \end{Bmatrix} = \begin{bmatrix} 1 & 0 & 0 \\ 0 & c_\phi & s_\phi \\ 0 & -s_\phi & c_\phi \end{bmatrix} \begin{Bmatrix} \bar{I}_2 \\ \bar{J}_2 \\ \bar{K}_2 \end{Bmatrix} \tag{3.3}$$

By direct substitution, overall transformation can be determined by Equation (3.4). An expansion of the result yields the transformation from the inertial reference frame to the body reference frame as shown in Equation (3.5).

$$\begin{Bmatrix} \vec{I}_B \\ \vec{J}_B \\ \vec{K}_B \end{Bmatrix} = [R_3(\phi)][R_2(\theta)][R_1(\psi)] \begin{Bmatrix} \vec{I}_I \\ \vec{J}_I \\ \vec{K}_I \end{Bmatrix} \tag{3.4}$$

$$\begin{Bmatrix} \vec{I}_B \\ \vec{J}_B \\ \vec{K}_B \end{Bmatrix} = \begin{bmatrix} c_\theta c_\psi & c_\theta s_\psi & -s_\theta \\ s_\phi s_\theta c_\psi - c_\phi s_\psi & s_\phi s_\theta s_\psi + c_\phi c_\psi & s_\phi c_\theta \\ c_\phi s_\theta c_\psi + s_\phi s_\psi & c_\phi s_\theta s_\psi - s_\phi c_\psi & c_\phi c_\theta \end{bmatrix} \begin{Bmatrix} \vec{I}_I \\ \vec{J}_I \\ \vec{K}_I \end{Bmatrix} = [T_I^B] \begin{Bmatrix} \vec{I}_I \\ \vec{J}_I \\ \vec{K}_I \end{Bmatrix} \tag{3.5}$$

3.3 Direct Fire Rocket Dynamic Model

A fin stabilized rocket with thrust propulsion is modeled as a rigid body described by six degrees of freedom. A schematic of the direct fire rocket configuration with major elements of the system identified is shown in Figure 3.2.

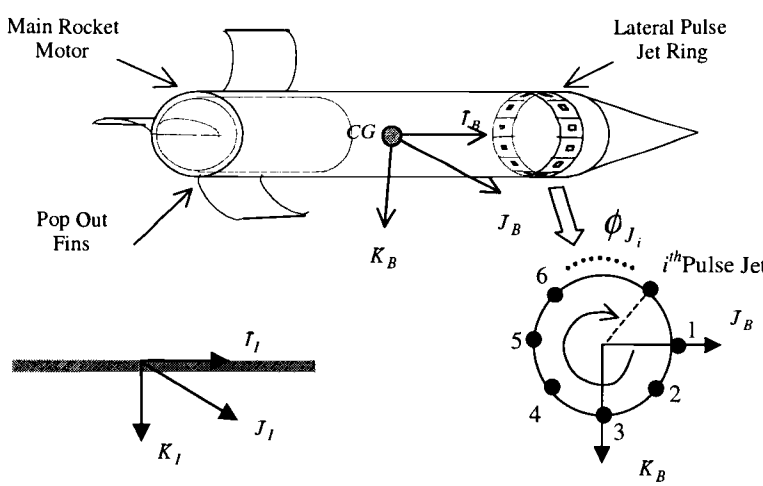

Figure 3.2 Schematic of a Direct Fire Rocket with a Lateral Pulse Jets

The six degrees of freedom include three position components of the mass center of the rocket as well as three Euler orientation angles of the body. The equations of motion are provided in Equations (3.6) through (3.9) (Gast, Morris, and Costello, 2000; Costello and Anderson, 1996).

$$\begin{Bmatrix} \dot{x} \\ \dot{y} \\ \dot{z} \end{Bmatrix} = \begin{bmatrix} c_\theta c_\psi & s_\phi s_\theta c_\psi - c_\phi s_\psi & c_\phi s_\theta c_\psi + s_\phi s_\psi \\ c_\theta s_\psi & s_\phi s_\theta s_\psi + c_\phi c_\psi & c_\phi s_\theta s_\psi - s_\phi c_\psi \\ -s_\theta & s_\phi c_\theta & c_\phi c_\theta \end{bmatrix} \begin{Bmatrix} u \\ v \\ w \end{Bmatrix} \tag{3.6}$$

$$\begin{Bmatrix} \dot{\phi} \\ \dot{\theta} \\ \dot{\psi} \end{Bmatrix} = \begin{bmatrix} 1 & s_\phi t_\theta & c_\phi t_\theta \\ 0 & c_\phi & -s_\phi \\ 0 & s_\phi / c_\theta & c_\phi / c_\theta \end{bmatrix} \begin{Bmatrix} p \\ q \\ r \end{Bmatrix} \tag{3.7}$$

$$\begin{Bmatrix} \dot{u} \\ \dot{v} \\ \dot{w} \end{Bmatrix} = \begin{Bmatrix} X/m \\ Y/m \\ Z/m \end{Bmatrix} - \begin{bmatrix} 0 & -r & q \\ r & 0 & -p \\ -q & p & 0 \end{bmatrix} \begin{Bmatrix} u \\ v \\ w \end{Bmatrix} \tag{3.8}$$

$$\begin{Bmatrix} \dot{p} \\ \dot{q} \\ \dot{r} \end{Bmatrix} = [I]^{-1} \left[\begin{Bmatrix} L \\ M \\ N \end{Bmatrix} - \begin{bmatrix} 0 & -r & q \\ r & 0 & -p \\ -q & p & 0 \end{bmatrix} [I] \begin{Bmatrix} p \\ q \\ r \end{Bmatrix} \right] \tag{3.9}$$

Equation (3.6) represents the translational kinematic differential equations that describe the relationship of the time derivative of the mass center position and the mass center velocity components. Equation (3.7) is the rotational kinematic differential equations that relate the time derivatives of the Euler's angles with the rocket's angular velocity components. Equations (3.8) and (3.9) are the translational kinetic differential equations and the rotational kinetic differential equations described in the body reference frame.

The applied loads appearing in Equation (3.8) contains contributions from rocket weight, $[X_W, Y_W, Z_W]^T$, air loads, $[X_A, Y_A, Z_A]^T$, main rocket thrust, $[X_R, Y_R, Z_R]^T$, and lateral pulse jet forces, $[X_J, Y_J, Z_J]^T$.

$$\begin{Bmatrix} X \\ Y \\ Z \end{Bmatrix} = \begin{Bmatrix} X_W \\ Y_W \\ Z_W \end{Bmatrix} + \begin{Bmatrix} X_A \\ Y_A \\ Z_A \end{Bmatrix} + \begin{Bmatrix} X_R \\ Y_R \\ Z_R \end{Bmatrix} + \begin{Bmatrix} X_J \\ Y_J \\ Z_J \end{Bmatrix} \tag{3.10}$$

The applied moments about the rocket mass center contains contributions from steady air loads, $[L_{SA}, M_{SA}, N_{SA}]^T$, unsteady air loads, $[L_{UA}, M_{UA}, N_{UA}]^T$, main rocket thrust, $[L_R, M_R, N_R]^T$, and lateral pulse jet forces, $[L_J, M_J, N_J]^T$.

$$\begin{Bmatrix} L \\ M \\ N \end{Bmatrix} = \begin{Bmatrix} L_{SA} \\ M_{SA} \\ N_{SA} \end{Bmatrix} + \begin{Bmatrix} L_{UA} \\ M_{UA} \\ N_{UA} \end{Bmatrix} + \begin{Bmatrix} L_R \\ M_R \\ N_R \end{Bmatrix} + \begin{Bmatrix} L_J \\ M_J \\ N_J \end{Bmatrix} \tag{3.11}$$

The following subsections develop the functional forms of these applied external loads.

3.3.1 Weight Force

Since the translational kinetic equations are written in the rocket body reference frame, the weight along $\bar{K}_I$ must be transformed to the body frame. The rocket weight contribution is given by Equation (3.12).

$$\begin{Bmatrix} X_W \\ Y_W \\ Z_W \end{Bmatrix} = \left[T_I^B\right] \begin{Bmatrix} 0 \\ 0 \\ mg \end{Bmatrix} = mg \begin{Bmatrix} -s_\theta \\ s_\phi c_\theta \\ c_\phi c_\theta \end{Bmatrix} \tag{3.12}$$

When the rocket motors are active, the mass of the rocket is updated continuously.

3.3.2 Aerodynamic Forces and Moments

The integrated effect of surface tractions on the rocket caused by air in the atmospheric is modeled as a point force which depends on Mach number at the mass center of the rocket and the aerodynamic angle of attack of the rocket. The formula for the aerodynamic force is given by Equation (3.13).

$$\begin{Bmatrix} X_A \\ Y_A \\ Z_A \end{Bmatrix} = -\frac{\pi}{8}\rho V_A^2 D^2 \begin{Bmatrix} C_{X0} + C_{X2}(v_A^2 + w_A^2)/V_A^2 \\ C_{NA} v_A / V_A \\ C_{NA} w_A / V_A \end{Bmatrix} \tag{3.13}$$

The steady state air load moment is the cross product between the distance vector from the mass center to the center of pressure (COP) and the steady air load, as shown in Equation (3.14).

$$\begin{Bmatrix} L_A \\ M_A \\ N_A \end{Bmatrix} = \begin{bmatrix} 0 & -r_{Z_{CG\to COP}} & r_{Y_{CG\to COP}} \\ r_{Z_{CG\to COP}} & 0 & -r_{X_{CG\to COP}} \\ -r_{Y_{CG\to COP}} & r_{X_{CG\to COP}} & 0 \end{bmatrix} \begin{Bmatrix} X_A \\ Y_A \\ Z_A \end{Bmatrix} \tag{3.14}$$

The unsteady body aerodynamic moment provides a damping source for projectile angular motion and is given by Equation (3.15).

$$\begin{Bmatrix} L_{UA} \\ M_{UA} \\ N_{UA} \end{Bmatrix} = \frac{\pi}{8}\rho V_A^2 D^3 \begin{Bmatrix} C_{DD} + \dfrac{pDC_{LP}}{2V_A} \\ \dfrac{qDC_{MQ}}{2V_A} \\ \dfrac{rDC_{MQ}}{2V_A} \end{Bmatrix} \tag{3.15}$$

The center of pressure location and all aerodynamic coefficients depend on local Mach number. Computationally, they are computed by linear interpolation of a table of data corresponding to different Mach numbers. The air velocity of the mass center of the rocket includes contributions from inertial motion of the rocket and atmospheric mean wind. The mean atmospheric wind acts in the horizontal plane and is directed at an angle ψ_{MW} from the $\bar{I}_I$ axis. Equation (3.16) provides an expression for the aerodynamic velocity experienced by the mass center that includes body motion and mean atmospheric wind.

$$\begin{Bmatrix} u_A \\ v_A \\ w_A \end{Bmatrix} = \begin{Bmatrix} u \\ v \\ w \end{Bmatrix} + \begin{bmatrix} c_\theta c_\psi & c_\theta s_\psi & -s_\theta \\ s_\phi s_\theta c_\psi - c_\phi s_\psi & s_\phi s_\theta s_\psi + c_\phi c_\psi & s_\phi c_\theta \\ c_\phi s_\theta c_\psi + s_\phi s_\psi & c_\phi s_\theta s_\psi - s_\phi c_\psi & c_\phi c_\theta \end{bmatrix} \begin{Bmatrix} V_{MW} c_{\psi_{MW}} \\ V_{MW} s_{\psi_{MW}} \\ 0 \end{Bmatrix} \tag{3.16}$$

As shown in Equation (3.16), the magnitude of the atmospheric mean wind velocity is a function of projectile altitude.

$$V_{MW} = 0.636619 \sigma_{MW} \tan^{-1}\left(\frac{z}{1000}\right) \tag{3.17}$$

3.3.3 Main Rocket Motor Thrust Forces and Moments

The main rocket motor increases the velocity of the rocket by providing high thrust levels during the initial portion of the trajectory. In some direct fire rocket designs, the exhaust nozzle contains several flutes such that the exiting flow is turned which causes, in aggregate, a rolling moment. To account for this effect, the main rocket motor is considered to be a set of four smaller rocket motors that act as point forces on the body. The position and thrust orientation of each small rocket motor on the body are determined to match known inertial properties before

and after burn and to match a specified roll time trace. Equation 8 provides the main rocket motor force formula.

$$\begin{Bmatrix} X_R \\ Y_R \\ Z_R \end{Bmatrix} = \sum_{i=1}^{4} T_{Ri} \begin{Bmatrix} n_{RX\,i} \\ n_{RY\,i} \\ n_{RZ\,i} \end{Bmatrix} \tag{3.18}$$

In Equation (3.18), the thrust amplitude profile, T_{R_i}, is a known function of time. The thrust moments are the sum of the cross products between the distances from the mass center to individual force points (R_i) and the individual thrust forces.

$$\begin{Bmatrix} L_R \\ M_R \\ N_R \end{Bmatrix} = \sum_{i=1}^{4} T_{Ri} \begin{bmatrix} 0 & -r_{Z_{CG\to R_i}} & r_{Y_{CG\to R_i}} \\ r_{Z_{CG\to R_i}} & 0 & -r_{X_{CG\to R_i}} \\ -r_{Y_{CG\to R_i}} & r_{X_{CG\to R_i}} & 0 \end{bmatrix} \begin{Bmatrix} n_{RX\,i} \\ n_{RY\,i} \\ n_{RZ\,i} \end{Bmatrix} \tag{3.19}$$

3.3.4 Lateral Pulse Jet Forces and Moments

The lateral pulse jet forces act around the pulse jet ring as shown in Figure (3.2). The pulse jet ring is located on the skin of the projectile and near the nose of the rocket. Individual pulse jets are uniformly distributed azimuthally around the lateral pulse jet ring. A key feature of the pulse jet configuration considered here is that each pulse jet can be fired only once. Since the lateral pulse jets are active over a very short duration of time when compared to the time scale of a complete rocket trajectory, the thrust force is modeled as a constant when active. Also, since by definition a lateral pulse jet acts in the $\bar{J}_B$ and $\bar{K}_B$ plane, the $\bar{I}_B$ component of the lateral pulse jet force is zero. Equation (3.20) provides the lateral pulse jet force formula.

$$\begin{Bmatrix} X_J \\ Y_J \\ Z_J \end{Bmatrix} = \sum_{i=1}^{n_J} T_{J_i} \begin{Bmatrix} 0 \\ -\cos(\phi_{J_i}) \\ -\sin(\phi_{J_i}) \end{Bmatrix} \tag{3.20}$$

where

$\phi_{J_i} = \dfrac{2\pi(i-1)}{n_J}$ - Angle between $\vec{J}_B$ axis and the i^{th} pulse jet.

The pulse jet moment is the sum of the products between the distances from the mass center to individual pulse jets.

$$\begin{Bmatrix} L_J \\ M_J \\ N_J \end{Bmatrix} = \sum_{i=1}^{n_J} T_{J_i} \begin{bmatrix} 0 & -r_{Z_{CG\to J_i}} & r_{Y_{CG\to J_i}} \\ r_{Z_{CG\to J_i}} & 0 & -r_{X_{CG\to J_i}} \\ -r_{Y_{CG\to J_i}} & r_{X_{CG\to J_i}} & 0 \end{bmatrix} \begin{Bmatrix} 0 \\ -\cos(\phi_{J_i}) \\ -\sin(\phi_{J_i}) \end{Bmatrix} \tag{3.21}$$

CHAPTER 4
INERTIAL MEASUREMENT UNIT DYNAMIC MODEL

The purpose of the Inertial Measurement Unit (IMU) is to estimate the state of rocket during flight using sensor measurements provided by three linear accelerometers and three rate gyros. Consider an IMU located at a point S on the rocket as shown in Figure 4.1.

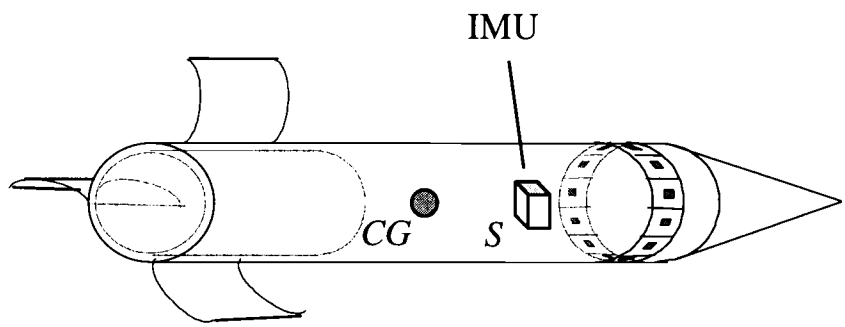

Figure 4.1 Schematic Diagram of IMU Mounted in the Rocket.

The sensitive axes of the IMU are aligned to the body reference frame. Therefore the IMU obtains an inertial reading of acceleration $\hat{a}_{IMU/I} = \hat{a}_{x_{SII}}\vec{I}_B + \hat{a}_{y_{SII}}\vec{J}_B + \hat{a}_{z_{SII}}\vec{K}_B$ and the reading in angular rates, $\hat{p}\vec{I}_B + \hat{q}\vec{J}_B + \hat{r}\vec{K}_B$, with all quantities expressed in the body reference frame. The superscript (^) denotes that the quantity is measured or estimated using sensor data. Estimation of the IMU location in inertial space can be obtained by integrating the translational kinematic equations.

$$\begin{Bmatrix} \dot{\hat{x}} \\ \dot{\hat{y}} \\ \dot{\hat{z}} \end{Bmatrix} = \begin{bmatrix} c_{\hat{\theta}}c_{\hat{\psi}} & s_{\hat{\phi}}s_{\hat{\theta}}c_{\hat{\psi}} - c_{\hat{\phi}}s_{\hat{\psi}} & c_{\hat{\phi}}s_{\hat{\theta}}c_{\hat{\psi}} + s_{\hat{\phi}}s_{\hat{\psi}} \\ c_{\hat{\theta}}s_{\hat{\psi}} & s_{\hat{\phi}}s_{\hat{\theta}}s_{\hat{\psi}} + c_{\hat{\phi}}c_{\hat{\psi}} & c_{\hat{\phi}}s_{\hat{\theta}}s_{\hat{\psi}} - s_{\hat{\phi}}c_{\hat{\psi}} \\ -s_{\hat{\theta}} & s_{\hat{\phi}}c_{\hat{\theta}} & c_{\hat{\phi}}c_{\hat{\theta}} \end{bmatrix} \begin{Bmatrix} \hat{u}_S \\ \hat{v}_S \\ \hat{w}_S \end{Bmatrix} \tag{4.1}$$

Integration of the rotational kinematic equation yields estimations of the Euler angles of the rocket.

$$\begin{Bmatrix} \dot{\hat{\phi}} \\ \dot{\hat{\theta}} \\ \dot{\hat{\psi}} \end{Bmatrix} = \begin{bmatrix} 1 & s_{\hat{\phi}}t_{\hat{\theta}} & c_{\hat{\phi}}t_{\hat{\theta}} \\ 0 & c_{\hat{\phi}} & -s_{\hat{\phi}} \\ 0 & s_{\hat{\phi}}/c_{\hat{\theta}} & c_{\hat{\phi}}/c_{\hat{\theta}} \end{bmatrix} \begin{Bmatrix} \hat{p} \\ \hat{q} \\ \hat{r} \end{Bmatrix} \tag{4.2}$$

The kinematic formulas for the acceleration of point on a rotating body yield differential equations for the velocity components of the IMU point with respect to the inertial reference frame expressed in the rocket body coordinate system.

$$\begin{Bmatrix} \dot{\hat{u}}_{S/I} \\ \dot{\hat{v}}_{S/I} \\ \dot{\hat{w}}_{S/I} \end{Bmatrix} = \begin{Bmatrix} \hat{a}_{X_{S/I}} \\ \hat{a}_{Y_{S/I}} \\ \hat{a}_{Z_{S/I}} \end{Bmatrix} - \begin{bmatrix} 0 & -\hat{r} & \hat{q} \\ \hat{r} & 0 & -\hat{p} \\ -\hat{q} & \hat{p} & 0 \end{bmatrix} \begin{Bmatrix} \hat{u}_{S/I} \\ \hat{v}_{S/I} \\ \hat{w}_{S/I} \end{Bmatrix} \tag{4.3}$$

The set of Equations (4.1), (4.2) and (4.3) provide differential equations which when integrated, provide an estimate of the rocket position and orientation which can be used for the flight control.

4.1 Conventional Acceleration and Angular Velocity Measurement

The acceleration of a sensor point, S_i, located on the rocket body with respect to inertial space can be computed at any time instant using the state of the rocket and its time derivatives.

$$\vec{a}_{S_i/I} = a_{X_{S_i}} \vec{I}_B + a_{Y_{S_i}} \vec{J}_B + a_{Z_{S_i}} \vec{K}_B \tag{4.4}$$

$$\begin{Bmatrix} a_{X_{S/I}} \\ a_{Y_{S/I}} \\ a_{Z_{S/I}} \end{Bmatrix} = \begin{Bmatrix} \dot{u} \\ \dot{v} \\ \dot{w} \end{Bmatrix} + [N] \begin{Bmatrix} u \\ v \\ w \end{Bmatrix} + [M] \begin{Bmatrix} r_{X_{CG \to S_i}} \\ r_{Y_{CG \to S_i}} \\ r_{Z_{CG \to S_i}} \end{Bmatrix} \tag{4.5}$$

where,

$$[N] = \begin{bmatrix} 0 & -r & q \\ r & 0 & -p \\ -q & p & 0 \end{bmatrix}$$

$$[M] = \begin{bmatrix} -q^2 - r^2 & pq - \alpha_Z & pr + \alpha_Y \\ pq + \alpha_Z & -p^2 - r^2 & qr - \alpha_X \\ pr - \alpha_Y & qr + \alpha_X & -p^2 - q^2 \end{bmatrix}$$

Since accelerometers are seismic devices, gravity is not included in the raw measurement and must be subtracted for processing measurements. The measured acceleration at the location of the IMU, or point S_i, is the combination of the actual acceleration and the acceleration due to the gravity, as shown in Equation (4.6).

$$\begin{Bmatrix} \hat{a}_{X_{S/I}} \\ \hat{a}_{Y_{S/I}} \\ \hat{a}_{Z_{S/I}} \end{Bmatrix} = \begin{Bmatrix} \dot{u} \\ \dot{v} \\ \dot{w} \end{Bmatrix} + [N] \begin{Bmatrix} u \\ v \\ w \end{Bmatrix} + [M] \begin{Bmatrix} r_{X_{CG \to S_i}} \\ r_{Y_{CG \to S_i}} \\ r_{Z_{CG \to S_i}} \end{Bmatrix} - \begin{Bmatrix} -s_{\hat{\theta}} g \\ s_{\hat{\phi}} c_{\hat{\theta}} g \\ c_{\hat{\phi}} c_{\hat{\theta}} g \end{Bmatrix} \tag{4.6}$$

The differential equations for the IMU require measurement of the translational acceleration of the IMU and angular velocity of the rocket, both with respect to inertial space. Data acquisition is typically implemented with 3 single axis accelerometers and 3 single axis gyros embedded inside the IMU system. In practice, however, the signals from these sensors is distorted by various disturbance sources, including noise, bias, cross axis sensitivity, and misalignment. To accurately model the actual signal output by a sensor, consider one sensor which is located at a point, S_i. A sensor reference frame ($\vec{I}_{S_i}, \vec{J}_{S_i}, \vec{K}_{S_i}$) is associated with each individual sensor such that the sensor frame origin is located at the sensor point, S_i, and is aligned such that the $\vec{I}_{S_i}$ axis is directed along the sensitive axis of the sensor. The transformation from the body reference frame to the sensor frame for each individual sensor is defined by a matrix [T_{S_i}] as shown in Equation (4.7).

$$\begin{Bmatrix} \vec{I}_i \\ \vec{J}_i \\ \vec{K}_i \end{Bmatrix} = [T_{S_i}] \begin{Bmatrix} \vec{I}_B \\ \vec{J}_B \\ \vec{K}_B \end{Bmatrix} \tag{4.7}$$

Six sensor coordinate systems are utilized corresponding to the axis systems of the linear accelerometers and three rate gyroscopes contained in the IMU. The subscripts for the sensors are *A1, A2, A3, G1, G2*, and *G3*, respectively. With an assumption that the alignment of the sensor reference frames and the body frame are perfect, the detailed definitions of these matrices for all individual sensors are presented in Equations (4.8) to (4.13).

$$\begin{Bmatrix} \vec{I}_{A1} \\ \vec{J}_{A1} \\ \vec{K}_{A1} \end{Bmatrix} = [T_{A1}] \begin{Bmatrix} \vec{I}_B \\ \vec{J}_B \\ \vec{K}_B \end{Bmatrix} = \begin{bmatrix} 1 & 0 & 0 \\ 0 & 1 & 0 \\ 0 & 0 & 1 \end{bmatrix} \begin{Bmatrix} \vec{I}_B \\ \vec{J}_B \\ \vec{K}_B \end{Bmatrix} \tag{4.8}$$

$$\begin{Bmatrix} \vec{I}_{A2} \\ \vec{J}_{A2} \\ \vec{K}_{A2} \end{Bmatrix} = [T_{A2}] \begin{Bmatrix} \vec{I}_B \\ \vec{J}_B \\ \vec{K}_B \end{Bmatrix} = \begin{bmatrix} 0 & 1 & 0 \\ -1 & 0 & 0 \\ 0 & 0 & 1 \end{bmatrix} \begin{Bmatrix} \vec{I}_B \\ \vec{J}_B \\ \vec{K}_B \end{Bmatrix} \tag{4.9}$$

$$\begin{Bmatrix} \vec{I}_{A3} \\ \vec{J}_{A3} \\ \vec{K}_{A3} \end{Bmatrix} = [T_{A3}] \begin{Bmatrix} \vec{I}_B \\ \vec{J}_B \\ \vec{K}_B \end{Bmatrix} = \begin{bmatrix} 0 & 0 & 1 \\ -1 & 0 & 0 \\ 0 & -1 & 0 \end{bmatrix} \begin{Bmatrix} \vec{I}_B \\ \vec{J}_B \\ \vec{K}_B \end{Bmatrix} \tag{4.10}$$

$$\begin{Bmatrix} \vec{I}_{G1} \\ \vec{J}_{G1} \\ \vec{K}_{G1} \end{Bmatrix} = [T_{G1}] \begin{Bmatrix} \vec{I}_B \\ \vec{J}_B \\ \vec{K}_B \end{Bmatrix} = \begin{bmatrix} 1 & 0 & 0 \\ 0 & 1 & 0 \\ 0 & 0 & 1 \end{bmatrix} \begin{Bmatrix} \vec{I}_B \\ \vec{J}_B \\ \vec{K}_B \end{Bmatrix} \tag{4.11}$$

$$\begin{Bmatrix} \vec{I}_{G2} \\ \vec{J}_{G2} \\ \vec{K}_{G2} \end{Bmatrix} = [T_{G2}] \begin{Bmatrix} \vec{I}_B \\ \vec{J}_B \\ \vec{K}_B \end{Bmatrix} = \begin{bmatrix} 0 & 1 & 0 \\ -1 & 0 & 0 \\ 0 & 0 & 1 \end{bmatrix} \begin{Bmatrix} \vec{I}_B \\ \vec{J}_B \\ \vec{K}_B \end{Bmatrix} \tag{4.12}$$

$$\begin{Bmatrix} \vec{I}_{G3} \\ \vec{J}_{G3} \\ \vec{K}_{G3} \end{Bmatrix} = [T_{G3}] \begin{Bmatrix} \vec{I}_B \\ \vec{J}_B \\ \vec{K}_B \end{Bmatrix} = \begin{bmatrix} 0 & 0 & 1 \\ -1 & 0 & 0 \\ 0 & -1 & 0 \end{bmatrix} \begin{Bmatrix} \vec{I}_B \\ \vec{J}_B \\ \vec{K}_B \end{Bmatrix} \tag{4.13}$$

In addition to recording the actual acceleration at the sensor point along the sensitive axis, the signals from the accelerometers contain noise, sensor bias, and cross axis sensitivity. Furthermore, the sensor axis may be misaligned. Moreover, the component of the gravity load on the proof mass inside the accelerometer contributes to the accelerometer signal output. Thus, the output of each single axis linear accelerometer within the IMU is given in Equations (4.14) through (4.16).

$$\tilde{a}_{1X} = a_{1X}^N + a_{1X}^B + a_{1X} + a_{1Y} C_{1Y}^A + a_{1Z} C_{1Z}^A + s_\theta g \tag{4.14}$$

$$\tilde{a}_{2X} = a_{2X}^N + a_{2X}^B + a_{2X} + a_{2Y} C_{2Y}^A + a_{2Z} C_{2Z}^A - s_\phi c_\theta g \tag{4.15}$$

$$\tilde{a}_{3X} = a_{3X}^N + a_{3X}^B + a_{3X} + a_{3Y} C_{3Y}^A + a_{3Z} C_{3Z}^A - c_\phi c_\theta g \tag{4.16}$$

In Equations (4.14) through (4.16), a_{iX}^{N} represents sensor noise of the i^{th} accelerometer which is modeled as an independent Gaussian random variable, a_{iX}^{B} represents bias of the i^{th} accelerometer which is assumed constant throughout a trajectory, C_{iY}^{A} represents the $\bar{J}_{A_i}$ cross axis sensitivity of the i^{th} accelerometer, while C_{iZ}^{A} represent the $\bar{K}_{A_i}$ cross axis sensitivity of the i^{th} accelerometer. Both cross axis sensitivity constants are assumed to be constant throughout a trajectory. The component of the acceleration of the i^{th} sensor point with respect to the ground, expressed in the i^{th} accelerometer frame, are denoted a_{iX}, a_{iY}, and a_{iZ}. These components of the acceleration of a sensor point are related to the acceleration of sensor point expressed in the rocket body frame through a simple transformation defined previously.

$$\begin{Bmatrix} a_{iX} \\ a_{iY} \\ a_{iZ} \end{Bmatrix} = [T_{Ai}] \begin{Bmatrix} a_{X_{S/I}} \\ a_{Y_{S/I}} \\ a_{Z_{S/I}} \end{Bmatrix} \qquad , i = 1, 2, 3 \tag{4.17}$$

By expressing acceleration of individual sensors in terms of the body acceleration at the IMU location and using relationships established in Equation (4.17), Equations (4.14) to (4.16) can be rewritten in matrix form (4.17)

$$\begin{Bmatrix} \tilde{a}_{1X} \\ \tilde{a}_{2X} \\ \tilde{a}_{3X} \end{Bmatrix} = \begin{Bmatrix} a_{1X}^{N} \\ a_{2X}^{N} \\ a_{3X}^{N} \end{Bmatrix} + \begin{Bmatrix} a_{1X}^{B} \\ a_{2X}^{B} \\ a_{3X}^{B} \end{Bmatrix} + [T^{A}] \begin{Bmatrix} a_{X_{S/I}} \\ a_{Y_{S/I}} \\ a_{Z_{S/I}} \end{Bmatrix} - \begin{Bmatrix} -s_{\hat{\theta}} g \\ s_{\hat{\phi}} c_{\hat{\theta}} g \\ c_{\hat{\phi}} c_{\hat{\theta}} g \end{Bmatrix} \tag{4.18}$$

where

$$[T_A] = [T_S^A] + [T_{CAY}^A] + [T_{CAZ}^A]$$

$$[T_S^A]=\begin{bmatrix} T_{A1}(1,1) & T_{A1}(1,2) & T_{A1}(1,3) \\ T_{A2}(1,1) & T_{A2}(1,2) & T_{A2}(1,3) \\ T_{A3}(1,1) & T_{A3}(1,2) & T_{A3}(1,3) \end{bmatrix}$$

$$[T_{CAY}^A]=\begin{bmatrix} C_{1Y}^A T_{A1}(2,1) & C_{1Y}^A T_{A1}(2,2) & C_{1Y}^A T_{A1}(2,3) \\ C_{2Y}^A T_{A2}(2,1) & C_{2Y}^A T_{A2}(2,2) & C_{2Y}^A T_{A2}(2,3) \\ C_{3Y}^A T_{A3}(2,1) & C_{3Y}^A T_{A3}(2,2) & C_{3Y}^A T_{A3}(2,3) \end{bmatrix}$$

$$[T_{CAZ}^A]=\begin{bmatrix} C_{1Z}^A T_{A1}(3,1) & C_{1Z}^A T_{A1}(3,2) & C_{1Z}^A T_{A1}(3,3) \\ C_{2Z}^A T_{A2}(3,1) & C_{2Z}^A T_{A2}(3,2) & C_{2Z}^A T_{A2}(3,3) \\ C_{3Z}^A T_{A3}(3,1) & C_{3Z}^A T_{A3}(3,2) & C_{3Z}^A T_{A3}(3,3) \end{bmatrix}$$

Signals from the rate gyroscopes also contain noise, bias, and cross axis sensitivity in addition to recording the actual angular rate at the sensor location. Thus, the output of each single axis rate gyroscope in the IMU is given in Equations (4.19).

$$\tilde{\omega}_{1X} = \omega_{1X}^N + \omega_{1X}^B + \omega_{1X} + \omega_{1Y} C_{1Y}^G + \omega_{1Z} C_{1Z}^G \tag{4.19}$$

$$\tilde{\omega}_{2X} = \omega_{2X}^N + \omega_{2X}^B + \omega_{2X} + \omega_{2Y} C_{2Y}^G + \omega_{2Z} C_{2Z}^G \tag{4.20}$$

$$\tilde{\omega}_{3X} = \omega_{3X}^N + \omega_{3X}^B + \omega_{3X} + \omega_{3Y} C_{3Y}^G + \omega_{3Z} C_{3Z}^G \tag{4.21}$$

In Equations (4.19) through (4.21), ω_{iX}^N represents sensor noise of the i^{th} gyroscope which is modeled as an independent Gaussian random variable, ω_{iX}^B represents bias of the i^{th} gyroscope which is assumed constant throughout a trajectory, C_{iY}^G represents the $\vec{J}_{S_i}$ cross axis sensitivity of the i^{th} gyroscope, while C_{iZ}^G represent the $\vec{K}_{S_i}$ cross axis sensitivity of the i^{th} gyroscope. Both cross axis

sensitivity constants are assumed to be constant throughout a trajectory. The component of the gyro of i^{th} sensor point with respect to the ground, expressed in the i^{th} gyro frame, are denoted ω_{iX}, ω_{iY}, and ω_{iZ}. These components of the angular velocity of a sensor point are related to the angular velocity of sensor point expressed in the rocket body frame through a simple transformation defined previously.

$$\begin{Bmatrix} \omega_{iX} \\ \omega_{iY} \\ \omega_{iZ} \end{Bmatrix} = [T_{Gi}] \begin{Bmatrix} p \\ q \\ r \end{Bmatrix} \qquad , i = 1, 2, 3 \tag{4.22}$$

By expressing angular velocity of individual sensors in terms of the body angular velocity at the IMU location using relationships established in Equation (4.22), Equations (4.19) to (4.21) can be rewritten in matrix form (4.23).

$$\begin{Bmatrix} \tilde{\omega}_{1X} \\ \tilde{\omega}_{2X} \\ \tilde{\omega}_{3X} \end{Bmatrix} = \begin{Bmatrix} \omega_{1X}^{N} \\ \omega_{2X}^{N} \\ \omega_{3X}^{N} \end{Bmatrix} + \begin{Bmatrix} \omega_{1X}^{B} \\ \omega_{2X}^{B} \\ \omega_{3X}^{B} \end{Bmatrix} + [T_G] \begin{Bmatrix} p \\ q \\ r \end{Bmatrix} \tag{4.23}$$

where

$$[T_G] = [T_S^G] + [T_{CAY}^G] + [T_{CAZ}^G]$$

$$[T_S^G] = \begin{bmatrix} T_{G1}(1,1) & T_{G1}(1,2) & T_{G1}(1,3) \\ T_{G2}(1,1) & T_{G2}(1,2) & T_{G2}(1,3) \\ T_{G3}(1,1) & T_{G3}(1,2) & T_{G3}(1,3) \end{bmatrix}$$

$$[T_{CAY}^G] = \begin{bmatrix} C_{1Y}^G T_{G1}(2,1) & C_{1Y}^G T_{G1}(2,2) & C_{1Y}^G T_{G1}(2,3) \\ C_{2Y}^G T_{G2}(2,1) & C_{2Y}^G T_{G2}(2,2) & C_{2Y}^G T_{G2}(2,3) \\ C_{3Y}^G T_{G3}(2,1) & C_{3Y}^G T_{G3}(2,2) & C_{3Y}^G T_{G3}(2,3) \end{bmatrix}$$

$$\left[T_{CAZ}^{G}\right]=\begin{bmatrix} C_{1Z}^{G}T_{G1}(3,1) & C_{1Z}^{G}T_{G1}(3,2) & C_{1Z}^{G}T_{G1}(3,3) \\ C_{2Z}^{G}T_{G2}(3,1) & C_{2Z}^{G}T_{G2}(3,2) & C_{2Z}^{G}T_{G2}(3,3) \\ C_{3Z}^{G}T_{G3}(3,1) & C_{3Z}^{G}T_{G3}(3,2) & C_{3Z}^{G}T_{G3}(3,3) \end{bmatrix}$$

In a practical setting, sensor noise cannot be estimated. The bias and the cross axis sensitivity can, however, be approximated from manufacturer specifications and preflight testing. Therefore, the model equations for the accelerometer readings and the gyroscope readings are derived in Equation (4.24) and (4.25).

$$\begin{Bmatrix} \hat{a}_{X_{SII}} \\ \hat{a}_{Y_{SII}} \\ \hat{a}_{Z_{SII}} \end{Bmatrix} = \left[\hat{T}_A\right]^{-1}\left(\begin{Bmatrix} \tilde{a}_{1X} \\ \tilde{a}_{2X} \\ \tilde{a}_{3X} \end{Bmatrix} - \begin{Bmatrix} \hat{a}_{1X}^{B} \\ \hat{a}_{2X}^{B} \\ \hat{a}_{3X}^{B} \end{Bmatrix}\right) + \begin{Bmatrix} -s_{\hat{\theta}}g \\ s_{\hat{\phi}}c_{\hat{\theta}}g \\ c_{\hat{\phi}}c_{\hat{\theta}}g \end{Bmatrix} \tag{4.24}$$

$$\begin{Bmatrix} \hat{p} \\ \hat{q} \\ \hat{r} \end{Bmatrix} = \left[\hat{T}_G\right]^{-1}\left(\begin{Bmatrix} \tilde{\omega}_{1X} \\ \tilde{\omega}_{2X} \\ \tilde{\omega}_{3X} \end{Bmatrix} - \begin{Bmatrix} \hat{\omega}_{1X}^{B} \\ \hat{\omega}_{2X}^{B} \\ \hat{\omega}_{3X}^{B} \end{Bmatrix}\right) \tag{4.25}$$

where $\left[\hat{T}_A\right]\left[\hat{T}_G\right]\hat{a}_{iX}^{B},\hat{\omega}_{iX}^{B}$ are approximated from manufacturer specifications.

4.2 Unconventional Acceleration and Angular Velocity Measurement

This section describes development of a general technique to estimate body frame components of angular velocity and acceleration of a rigid body using triaxial acceleration measurements which is free from numerical integration and its inherent drift errors. An error analysis is conducted to establish how acceleration measurements errors propagate into angular rate estimation errors. Using a realistic direct fire atmospheric rocket trajectory, angular rates and accelerations are estimated with clusters of accelerometers placed on the skin of the rocket.

Practical issues such as the required number of sensors, sensor arrangement, data fusion, and quantization errors are addressed.

4.2.1 Three Tri-axial Accelerometer Algorithm for Determining Angular Velocity and Angular Acceleration

Consider Figure 4.2 that shows three triaxial accelerometers mounted arbitrarily on a rigid body. The accelerometers are located at points φ , β , and χ . The computational plane is defined as the plane formed by the sensor location points φ , β , and χ .

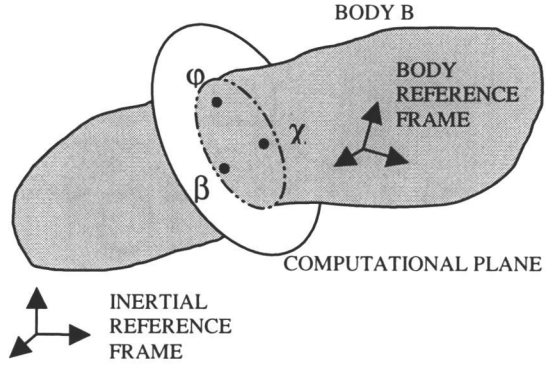

Figure 4.2 General Sensor Configuration

The computational frame, C, is aligned with the computational plane but is co-located with the body reference frame, B. Figure 4.3 details the geometry of the computational plane.

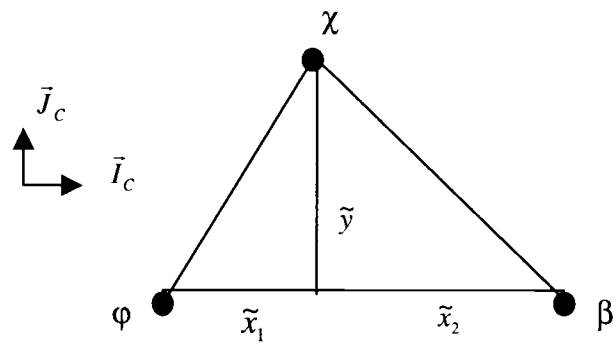

Figure 4.3 Computational Plane Geometry

It is assumed that the position of each sensor is known in the body frame. Using this data, the unit vectors of the computational frame are determined. The unit vector $\vec{I}_C$ is parallel to the distance vector from φ to β while the $\vec{K}_C$ axis is perpendicular to the computational plane and the unit vector $\vec{J}_C$ completes the right-handed triad. Using these definitions, an orthogonal transformation from the body frame to the computational frame can be formed. The difference in the linear acceleration of two points fixed on a rotating body reference frame with respect to inertial reference frame is given by Equation (4.26),

$$\vec{a}_{\beta/I} - \vec{a}_{\varphi/I} = \vec{\alpha}_{B/I} \times \vec{r}_{\varphi\to\beta} + \vec{\omega}_{B/I} \times \left(\vec{\omega}_{B/I} \times \vec{r}_{\varphi\to\beta}\right) \tag{4.26}$$

where, $\vec{\alpha}_{B/I}$ is the angular acceleration of B with respect to the initial reference frame, I, $\vec{\omega}_{B/I}$ is the angular velocity of the body reference frame B with respect to the inertial reference frame I, and $\vec{r}_{\varphi\to\beta}$ is the distance vector from φ to β. Measure numbers with a tilde symbol (~) refer to the computation frame while those without refer to the body frame.

Application of Equation (4.26) to body point combinations φ - β, φ - χ, and β - χ generates three sets of equations which are concatenated into matrix form as shown in Equations (4.27) through (4.30).

$$A = MR \tag{4.27}$$

$$A = \begin{bmatrix} \tilde{a}_{X_\beta} - \tilde{a}_{X_\varphi} & \tilde{a}_{X_\chi} - \tilde{a}_{X_\varphi} & \tilde{a}_{X_\chi} - \tilde{a}_{X_\beta} \\ \tilde{a}_{Y_\beta} - \tilde{a}_{Y_\varphi} & \tilde{a}_{Y_\chi} - \tilde{a}_{Y_\varphi} & \tilde{a}_{Y_\chi} - \tilde{a}_{Y_\beta} \\ \tilde{a}_{Z_\beta} - \tilde{a}_{Z_\varphi} & \tilde{a}_{Z_\chi} - \tilde{a}_{Z_\varphi} & \tilde{a}_{Z_\chi} - \tilde{a}_{Z_\beta} \end{bmatrix} \tag{4.28}$$

$$M = \begin{bmatrix} -\tilde{q}^2 - \tilde{r}^2 & -\tilde{\alpha}_Z + \tilde{p}\tilde{q} & \tilde{\alpha}_Y + \tilde{p}\tilde{r} \\ \tilde{\alpha}_Z + \tilde{p}\tilde{q} & -\tilde{p}^2 - \tilde{r}^2 & -\tilde{\alpha}_X + \tilde{q}\tilde{r} \\ -\tilde{\alpha}_Y + \tilde{p}\tilde{r} & \tilde{\alpha}_X + \tilde{q}\tilde{r} & -\tilde{p}^2 - \tilde{q}^2 \end{bmatrix} \tag{4.29}$$

$$R = \begin{bmatrix} \tilde{x}_1 + \tilde{x}_2 & \tilde{x}_1 & -\tilde{x}_2 \\ 0 & \tilde{y} & \tilde{y} \\ 0 & 0 & 0 \end{bmatrix} \tag{4.30}$$

Unfortunately, the distance matrix R is singular due to the fact that any two of the three distance vectors can be either added or subtracted to obtain the third vector. For three non colinear points, the distance matrix has rank two. As shown by Equation (4.31), if the kinematic equations are written in the computational frame as shown above, the generalized inverse allows the first two columns of M to be reconstructed.

$$RR^{-1} = \begin{bmatrix} 1 & 0 & 0 \\ 0 & 1 & 0 \\ 0 & 0 & 0 \end{bmatrix} \tag{4.31}$$

The property given in Equation (4.31) is not unique to the computational frame as defined above. Any computational frame with one axis perpendicular to the plane formed by the three points that locate the accelerometers will permit two of the columns of M to be reconstructed. Multiplication of Equation (4.27) by R^{-1} yields Equation (4.32).

$$AR^{-1} = \begin{bmatrix} M_{1,1} & M_{1,2} & 0 \\ M_{2,1} & M_{2,2} & 0 \\ M_{3,1} & M_{3,2} & 0 \end{bmatrix} \tag{4.32}$$

Using sensor position and accelerometer measurement data, Equation (4.32) provides a method to compute the first two columns of the matrix of unknowns, M, and as such furnishes six equations. While M consists of nine elements, the matrix is generated with six parameters that appear in a non-linear manner. The solution of these equations is given by Equations (4.33) through (4.38).

$$\tilde{p} = SIGN_{\tilde{p}} \sqrt{\frac{1}{2}\left[(M_{1,1} - M_{2,2}) + \sqrt{(M_{1,1} - M_{2,2})^2 + (M_{1,2} + M_{2,1})^2} \right]} \tag{4.33}$$

$$\tilde{q} = SIGN_{\tilde{q}} \sqrt{\frac{1}{2}\left[(M_{2,2} - M_{1,1}) + \sqrt{(M_{1,1} - M_{2,2})^2 + (M_{1,2} + M_{2,1})^2} \right]} \tag{4.34}$$

$$\tilde{r} = SIGN_{\tilde{r}} \sqrt{-\frac{1}{2}\left[(M_{1,1} + M_{2,2}) + \sqrt{(M_{1,1} - M_{2,2})^2 + (M_{1,2} + M_{2,1})^2} \right]} \tag{4.35}$$

$$\tilde{\alpha}_X = -SIGN_{\tilde{q}} SIGN_{\tilde{r}} \sqrt{-\frac{1}{4}(M_{1,2} + M_{2,1})^2 - \frac{1}{2} M_{2,2} \left(M_{2,2} - M_{1,1} + \sqrt{\begin{matrix} (M_{1,1} - M_{2,2})^2 \\ + (M_{1,2} + M_{2,1})^2 \end{matrix}} \right) + M_{3,2}} \tag{4.36}$$

$$\tilde{\alpha}_Y = SIGN_{\tilde{p}} SIGN_{\tilde{r}} \sqrt{-\frac{1}{4}(M_{1,2}+M_{2,1})^2 - \frac{1}{2}M_{1,1}\left(M_{1,1}-M_{2,2}+\sqrt{(M_{1,1}-M_{2,2})^2+(M_{1,2}+M_{2,1})^2}\right)} - M_{3,1} \quad (4.37)$$

$$\tilde{\alpha}_Z = \frac{1}{2}(M_{2,1}-M_{1,2}) \quad (4.38)$$

Where $SIGN_{\tilde{p}}$, $SIGN_{\tilde{q}}$, and $SIGN_{\tilde{r}}$ are the algebraic signs of $\tilde{p}$, $\tilde{q}$, and $\tilde{r}$, respectively. The kinematic formulas cannot isolate the algebraic signs of $\tilde{p}$, $\tilde{q}$, and $\tilde{r}$. To see this fact, note that if $\tilde{p}$, $\tilde{q}$, and $\tilde{r}$ is a solution to Equation (4.27), then $-\tilde{p}$, $-\tilde{q}$, and $-\tilde{r}$ must also be a solution as the M matrix is identical in both cases. Thus, two valid solutions to this inverse problem exist.

4.2.2 More Than Three Triaxial Accelerometers Clusters for Determining Angular Velocity and Angular Acceleration

When more than three non coplanar triaxial accelerometers are employed, there is no need to transform the geometric and measurement data to a computational plane since the distance matrix R is full rank. The distance matrix will be full rank provided at least four of the points in the cluster are non coplanar. In this case, all three columns of M can be completely reconstructed directly in the body reference frame. If n body point combinations are generated, then application of Equation (4.26) generates n columns of data in the acceleration matrix A and the distance matrix R. Equations (4.39) through (4.44) provide the solution formulas.

$$p = SIGN_p \sqrt{\frac{1}{2}\left[(M_{1,1}-M_{2,2})+\sqrt{(M_{1,1}-M_{2,2})^2+(M_{1,2}+M_{2,1})^2}\right]} \quad (4.39)$$

$$q = SIGN_q \sqrt{\frac{1}{2}\left[(M_{2,2}-M_{1,1})+\sqrt{(M_{1,1}-M_{2,2})^2+(M_{1,2}+M_{2,1})^2}\right]} \quad (4.40)$$

$$r = SIGN_r \sqrt{-\frac{1}{2}\left[(M_{1,1} + M_{2,2}) + \sqrt{(M_{1,1} - M_{2,2})^2 + (M_{1,2} + M_{2,1})^2}\right]} \tag{4.41}$$

$$\alpha_X = \frac{1}{2}(M_{3,2} - M_{2,3}) \tag{4.42}$$

$$\alpha_Y = \frac{1}{2}(M_{1,3} - M_{3,1}) \tag{4.43}$$

$$\alpha_Z = \frac{1}{2}(M_{2,1} - M_{1,2}) \tag{4.44}$$

where $SIGN_p$, $SIGN_q$, and $SIGN_r$ are the algebraic signs of p, q, and r, respectively.

Like the three triaxial cluster case, two valid solutions are possible depending on the algebraic sign of p, q, and r. Notice that the angular acceleration components can be directly computed without knowledge of the algebraic sign of the angular velocity components whereas in the three point case, α_X and α_Y required knowledge of the algebraic sign.

4.2.3 Algebraic Sign Determination

Success of both estimation algorithms discussed above fundamentally relies on knowledge of the algebraic sign of the angular velocity components. Regrettably, Equation (4.27) has no means to distinguish between the two possible solutions. Additional auxiliary conditions or information must be introduced for this specific purpose. For sensor clusters using more than three non coplanar points, knowledge of the algebraic sign of one of the angular velocity components is sufficient to establish the remaining algebraic signs. In a practical setting this is often the case as gun riffling or fin cant tend to produce very predictable roll rate time histories which are typically positive or negative over the duration of flight.

With a fully reconstructed M matrix, products of angular velocity components can be readily formed.

$$qr = \frac{1}{2}\left(M_{3,2} + M_{2,3}\right) \tag{4.45}$$

$$pr = \frac{1}{2}\left(M_{1,3} + M_{3,1}\right) \tag{4.46}$$

$$pq = \frac{1}{2}\left(M_{2,1} + M_{1,2}\right) \tag{4.47}$$

For example, if the roll rate algebraic sign is known to be positive at some time instant from an external sensor and the sum of $M_{12} + M_{21}$ is negative, then $SIGN_q$ must be negative. This logic can be used to establish the algebraic sign of the yaw rate as well. When the minimum set of three triaxial accelerometers is employed in a sensor cluster, if $SIGN_p$ is known then $SIGN_q$ can be inferred and visa-versa. However, $SIGN_r$ must be established independently.

If the algebraic sign of select components of angular velocity are not known then previous recent states of the body can be used to estimate the algebraic sign at a particular time instant. Denote x_p, x_q, and x_r as sequences of previous values of p, q, and r, respectively. Furthermore, denote δx_p, δx_q, and δx_r as the maximum expected change of p, q, and r during a given time interval. If $SIGN(Max(x_p) + \delta x_p) = SIGN(Min(x_p) - \delta x_p)$ then the algebraic sign of x_p is equal to the algebraic sign of p. Similar arguments apply to q and r. This techniques must be initialized with the correct algebraic sign and can fail to predict an algebraic sign estimate if all components of angular velocity are near zero. Once this condition is encountered, the algebraic signs must be reset by an external means. Other techniques based on numerically integrating the angular acceleration estimates can also be utilized. These methods have the disadvantage of

occasionally incorrectly predicting the algebraic sign and subsequently lock-in on the incorrect algebraic sign.

4.3 Measurement Error Sensitivity Analysis

Noisy accelerometer signals induce two distinct types of errors, namely, errors in the magnitude of the angular rate and acceleration components as well as errors in the algebraic sign of the angular rates. Here, we only consider magnitude errors. In the analysis to follow, it will be convenient to express the algorithm in a vector format. The outputs of the algorithm are the angular velocity and acceleration components expressed in the body frame which are placed in the vector Y as shown in Equation (4.48).

$$Y = [p \quad q \quad r \quad \alpha_X \quad \alpha_Y \quad \alpha_Z]^T \tag{4.48}$$

The input, U, to the algorithm consists of acceleration measurements.

$$U = [a_{X\varphi} \quad a_{Y\varphi} \quad a_{Z\varphi} \quad a_{X\beta} \quad a_{Y\beta} \quad a_{Z\beta} \quad a_{X\chi} \quad a_{Y\chi} \quad a_{Z\chi}]^T \tag{4.49}$$

The algorithm maps U to Y through a nonlinear operator, F.

$$Y = F(U) \tag{4.50}$$

The solution to Equation (4.50) can be approximated locally about Y_o and U_o using a Taylor series retaining only the linear term, to provide a relationship between measurement and estimation errors.

$$\delta Y = G \cdot \delta U \tag{4.51}$$

where

$$G = \left.\frac{\partial F}{\partial U}\right|_{U_o, Y_o} \tag{4.52}$$

The matrix G represents the sensitivity of computed angular velocities and acceleration components to errors in the input accelerometers. Note that the sensitivity matrix, G, is a non linear function of accelerometer and geometric parameters. This implies the sensitivity, G, is a function of the instantaneous angular rates, Y_0, and accelerations, U_0, as well as the sensor geometric location.

Consider a set of accelerometers where each of the nine measured acceleration components has noise superimposed. If each noise source is independent and all noise sources have the same *RMS* value, the *RMS* error of the i^{th} output is given by Equation (4.53).

$$\frac{RMS_{Y_i}}{RMS_U} = \sqrt{\sum_{j=1}^{9} G_{ij}^{\,2}} \tag{4.53}$$

Equation (4.53) furnishes an expression for the sensitivity of estimated angular velocity and acceleration component perturbations to accelerometer noise. In a practical setting, *RMS* values for accelerometer noise are known from manufacturer specifications and control system designers or system annalists require prescribed levels of fidelity in estimated angular velocity and acceleration components. Equation (4.53) provides a link between these two quantities.

In order to investigate acceleration measurement error propagation through the estimation algorithm, consider a typical direct fire atmospheric rocket which is 150 cm in length and has a diameter of 7.0 cm. Acceleration data is recorded at

three points on the rocket. The projectile body axis is defined such that the $\bar{I}_B$ axis emanates from the mass center of the projectile and points toward the nose. The $\bar{J}_B$ and $\bar{K}_B$ axes form an orthogonal set.

Three accelerometer geometric configurations are examined. These configurations are designated as "L", "T" and "O". The baseline L configuration is formed by mounting an accelerometer along each of the body frame axes. Each triaxial accelerometer is aligned with the body frame. The baseline T configuration consists of two sensors mounted along the $\bar{I}_B$ axis and one accelerometer mounted along the $\bar{J}_B$ axis. Configuration O employs two accelerometers mounted on opposite ends of the $\bar{K}_B$ axis and one accelerometer on the $\bar{J}_B$ axis. In the trade study results to follow, all configurations are altered by rotating the accelerometers along the $\bar{I}_B$ axis through the angle θ which in effect rotates the computational plane. However, the triaxial accelerometers remain aligned with the body axis. Each configuration is pictured in Figures 4.4, 4.5, and 4.6.

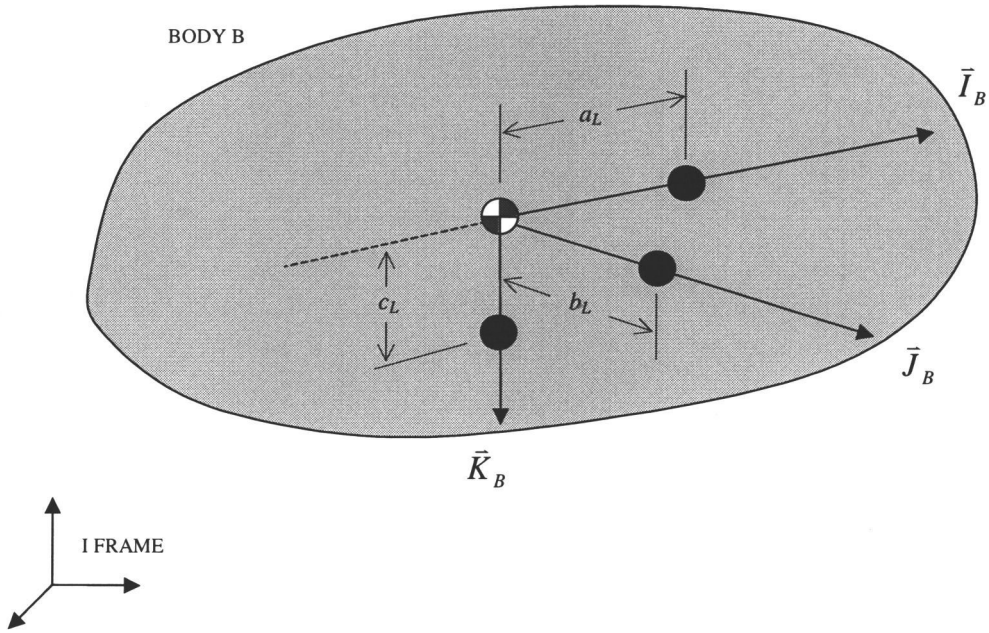

Figure 4.4 Configuration L.

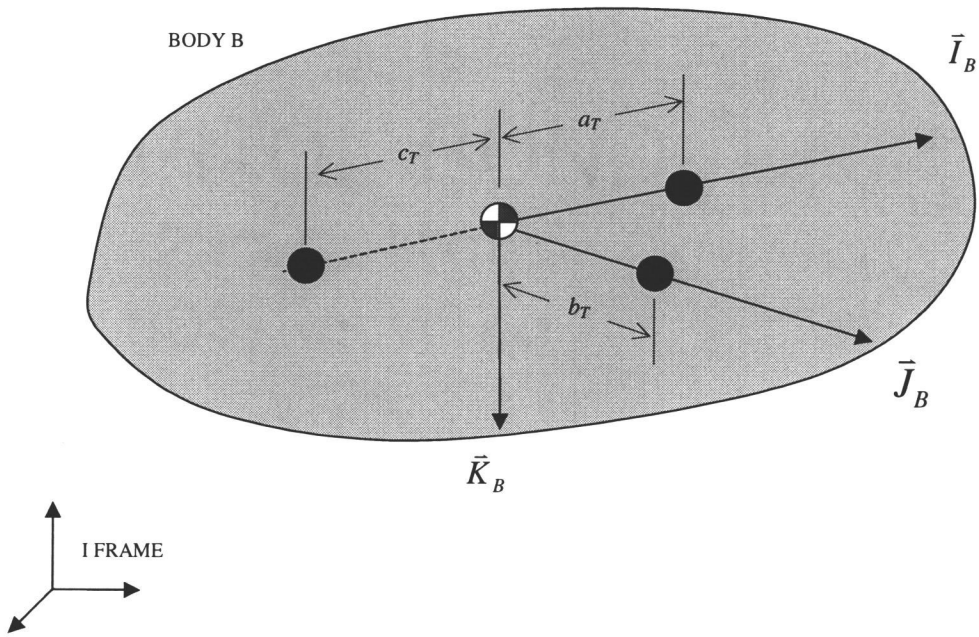

Figure 4.5 Configuration T.

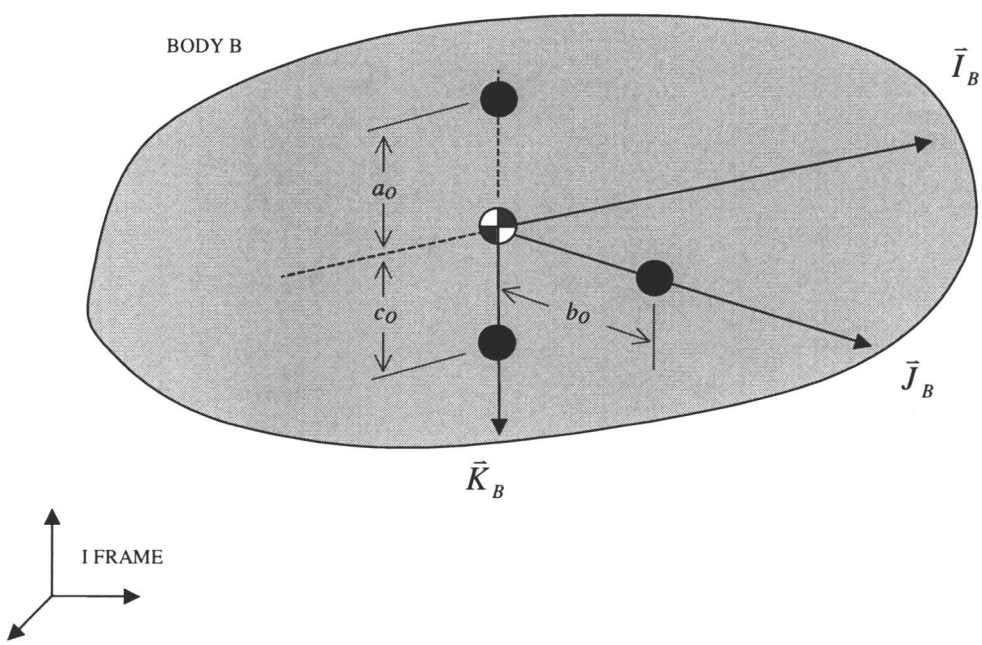

Figure 4.6 Configuration O.

For the representation of results shown here we shall consider a long slender rigid body with nominal accelerometer mounting positions: a_L = 0.85 m, b_L = 0.034 m, c_L = 0.034 m, a_T = 0.85 m, b_T = 0.55 m, c_T = 0.034 m, a_O = 0. 034 m, b_O = 0. 034 m, c_O = 0.034 m. Furthermore, for all results shown the nominal angular acceleration components are zero. Figure 4.7 shows the error sensitivity ratio for configuration L as a function of rigid body roll rate and the accelerometer constellation angle, θ. The plot is shown in polar form with roll rate from 0 to 20 r/s along the radial axis and constellation angle in the azimuthal direction. The nominal values for angular rates and acceleration are: q = 0.0001 r/s, r = 0.0001 r/s, $\alpha_x = \alpha_y = \alpha_z = 0$.

Figure 4.7 shows that when the rigid body is rotating slowly, the error sensitivity is greatest at zero roll rate and rapidly decays for all constellation angles. Figure 4.8 considers the same conditions that are plotted in Figure 4.7 except the nominal pitch and yaw rate are set to unity (q = 1 r/s, r = 1 r/s). Similar to the case shown in Figure 4.7 the largest error sensitivity occurs when the nominal roll rate is zero. For most constellation angles the error sensitivity decreases with increasing roll rates. However, Figure 4.8 also shows a nonlinear ridgeline emanating from p = 0. Figure 4.9 is similar to Figure 4.7 and 4.8 except the nominal pitch and yaw rates are modified to q = 0 r/s and r = 1.414 r/s. The same trends as Figure 4.8 are seen except the ridgeline or high error sensitivity has been rotated approximately 45°.

Figure 4.10, 4.11 and 4.12 show the same data as Figure 4.7, 4.8, and 4.9 except for the T configuration. When the magnitude of the angular velocity vector is small, error sensitivity of roll rate is large and rapidly decays as p is increased for all constellation angles θ. As shown in Figure 4.10, the error sensitivity of pitch and yaw rates contain sharp valleys along three constellation angles. In Figure 4.11 the nominal pitch rate and yaw rates are set to unity and a ridge in the error sensitivity of q and r is apparent. Like the L configuration the error sensitivity

ridge rotates as a function of the nominal q and r components, as shown by comparing Figure 4.11 and 4.12.

Figure 4.13, 4.14, and 4.15 provide error sensitivity results for the O configuration. The error sensitivity of roll rate is largest at $p = 0$ and decays as p is increased. When the pitch and yaw rates increased error sensitivity of q and r is flat for all constellation angles and nominal roll rates. The minimum, maximum, and average values of the error sensitivity for the L, T, and O configurations are shown in Tables 4.1, 4.2, and 4.3.

	RMS_p/RMS_a			**RMS_q/RMS_a**			**RMS_r/RMS_a**		
***q* rate / *r* rate (r/s)**	**0 / 0**	**1 / 1**	**0 / 1.414**	**0 / 0**	**1 / 1**	**0 / 1.414**	**0 / 0**	**1 / 1**	**0 / 1.414**
Maximum (dB)	52.8	53.5	52.2	60.9	77.5	79.2	60.9	77.5	47.4
Minimum (dB)	-12.3	-12.3	-12.3	-12.3	-19.3	-12.2	-12.3	-19.3	-16.3
Average (dB)	0.3	-3.0	-3.0	3.0	0.1	2.9	3.0	0.0	-8.5

Table 4.1 Error sensitivity for L configuration.

	RMS_p/RMS_a			**RMS_q/RMS_a**			**RMS_r/RMS_a**		
***q* rate / *r* rate (r/s)**	**0 / 0**	**1 / 1**	**0 / 1.414**	**0 / 0**	**1 / 1**	**0 / 1.414**	**0 / 0**	**1 / 1**	**0 / 1.414**
Maximum (dB)	54.6	54.6	54.6	65.5	80.9	82.0	65.5	80.9	11.6
Minimum (dB)	-10.5	-10.5	-10.5	-13.5	-22.3	-10.5	-13.5	-22.3	-19.3
Average (dB)	2.1	-1.8	-1.7	56.5	2.3	2.9	57.4	2.3	-18.8

Table 4.2 Error sensitivity for T configuration

	RMS_p/RMS_a			RMS_q/RMS_a			RMS_r/RMS_a		
q rate / r rate (r/s)	**0 / 0**	**1 / 1**	**0 / 1.414**	**0 / 0**	**1 / 1**	**0 / 1.414**	**0 / 0**	**1 / 1**	**0 / 1.414**
Maximum (dB)	55.0	54.6	54.6	84.1	14.6	12.8	84.1	14.6	12.8
Minimum (dB)	-11.3	-15.3	-15.3	78.6	9.8	12.8	78.6	9.8	12.8
Average (dB)	1.8	0.0	-0.1	81.7	12.8	12.8	81.5	12.8	12.8

Table 4.3 Error sensitivity for O configuration.

The above results underline the fact that error propagation is a strong function of the roll, pitch, and yaw rates as well as the geometric location of sensors. In order to further investigate error propagation as a function of pitch and yaw rates consider Figure 4.16. Figure 4.16 plots the error sensitivity of the yaw rate q for the L configuration as a function of q and r for three different constellation angles. The nominal roll rate is p = 2 r/s. A ridgeline in the error sensitivity which goes through $q = r = 0$ persists. The ridge rotates with the constellation angle θ. The algorithm yields the smallest error sensitivity to accelerometer noise when the measured angular vector is parallel to the combination of the position vectors from the origin of the body frame to all three sensors.

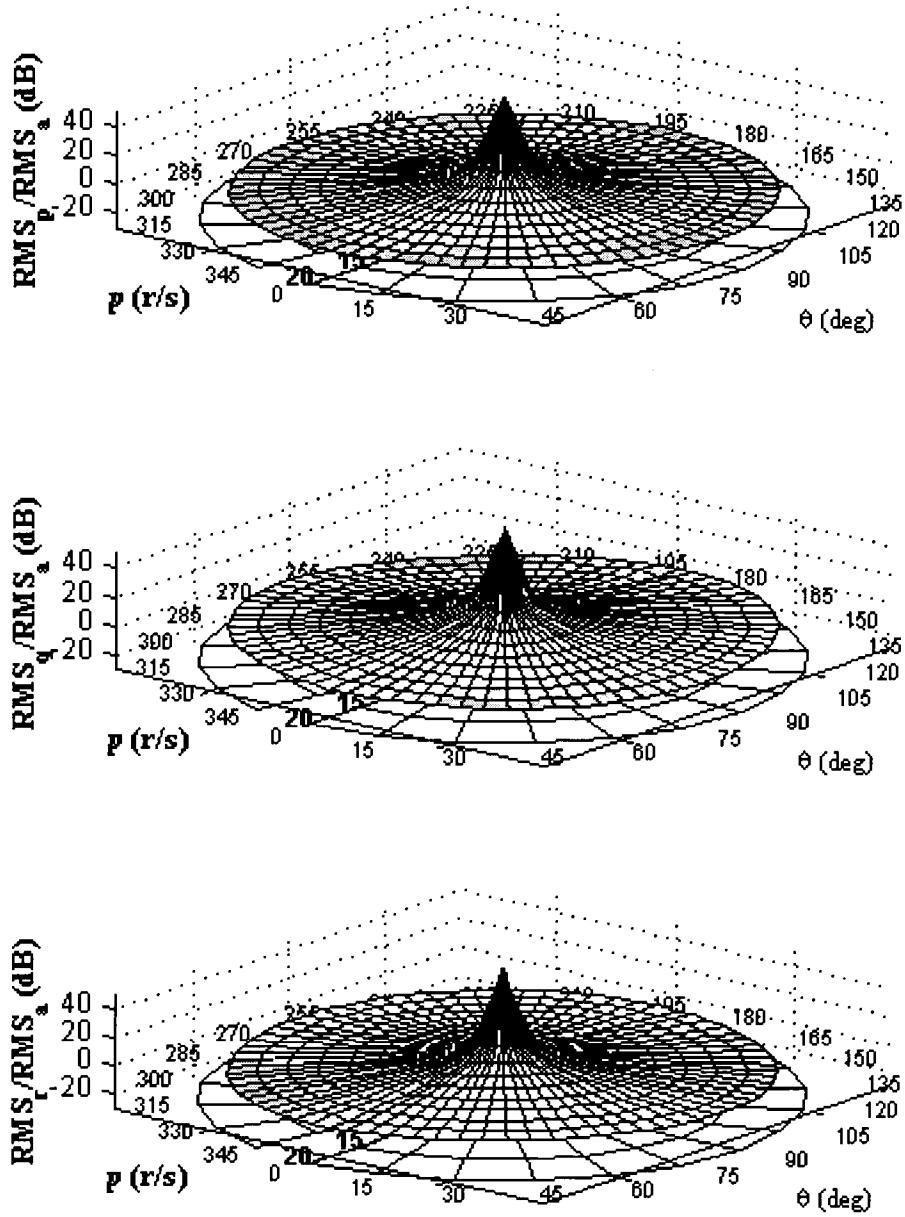

Figure 4.7 Configuration L Error Sensitivity Ratio versus Roll Rate and Sensor Constellation Angle (q = 0.0001 r/s, r = 0.0001 r/s).

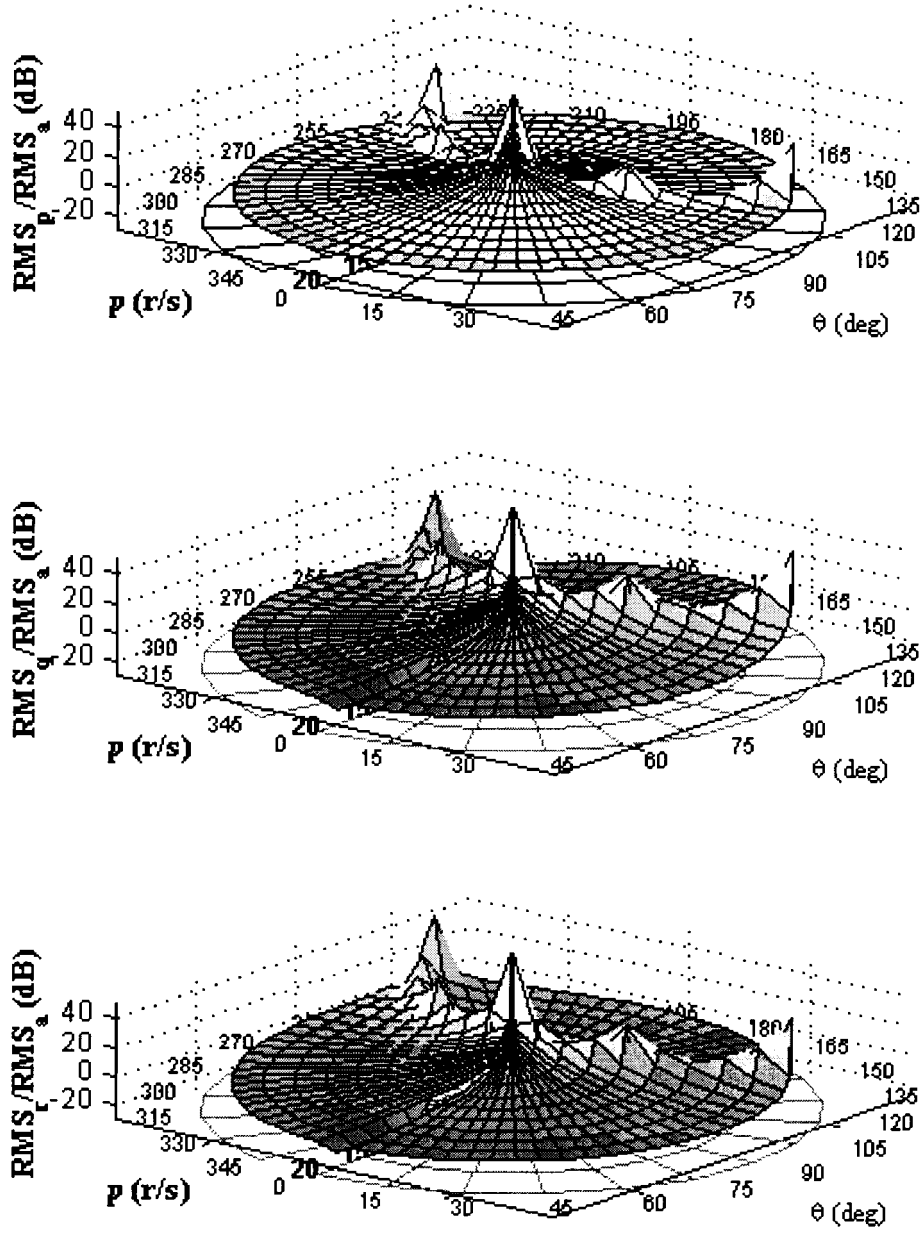

Figure 4.8 Configuration L Error Sensitivity Ratio versus Roll Rate and Sensor Constellation Angle (q = 1 r/s, r = 1 r/s).

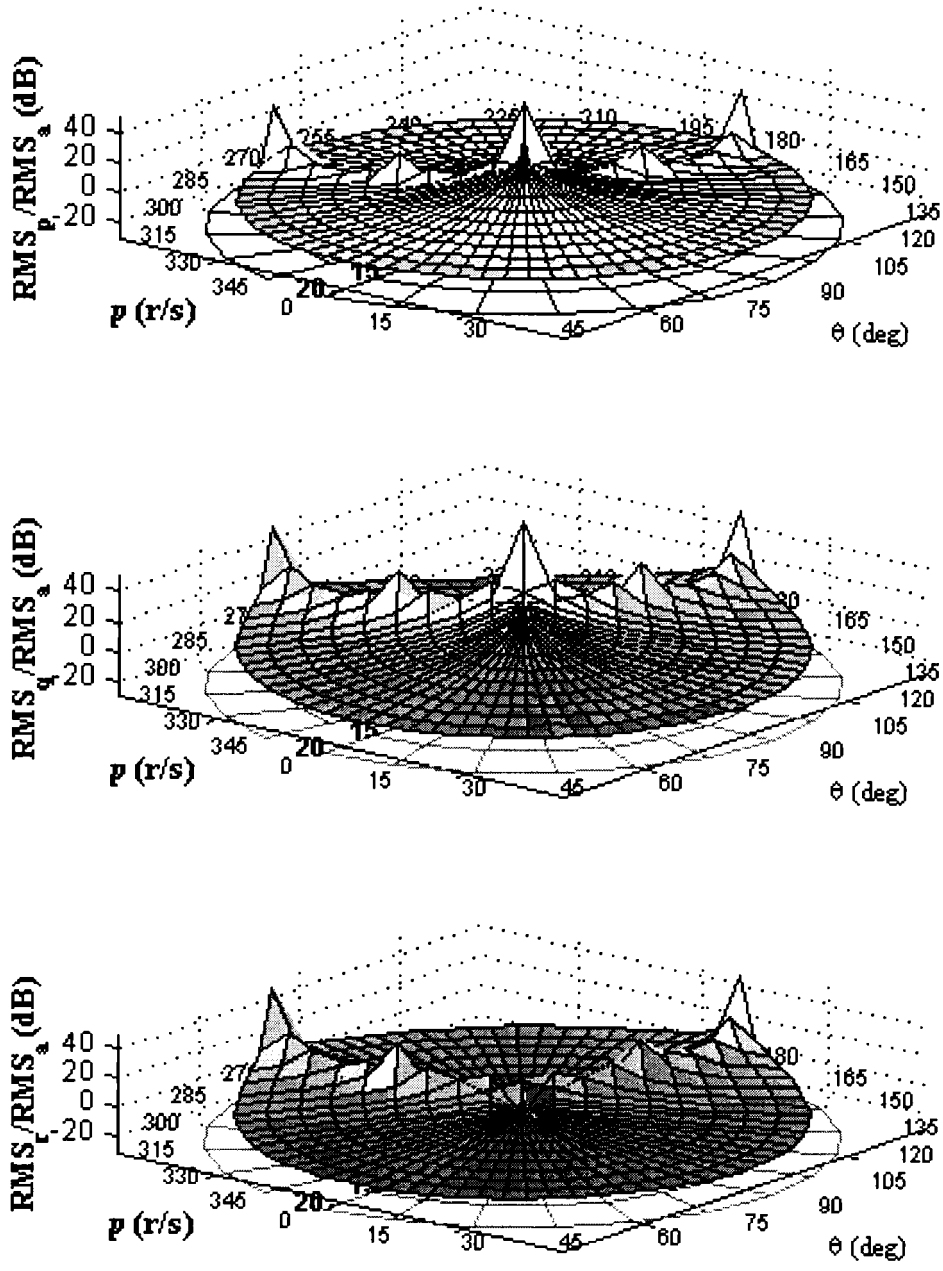

Figure 4.9 Configuration L Error Sensitivity Ratio versus Roll Rate and Sensor Constellation Angle (q = 0 r/s, r = 1.414 r/s).

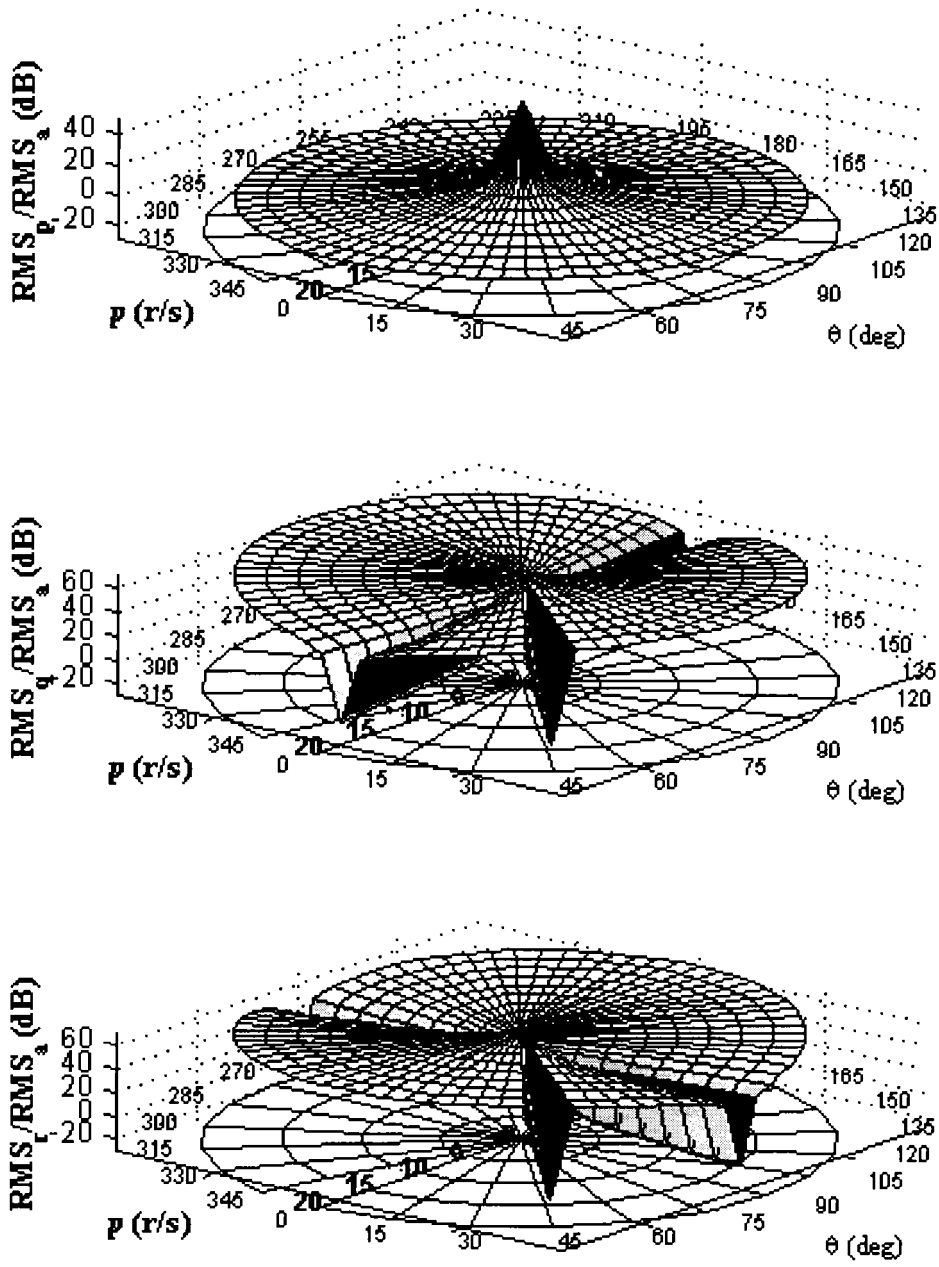

Figure 4.10 Configuration T Error Sensitivity Ratio versus Roll Rate and Sensor Constellation Angle (q = 0.0001 r/s, r = 0.0001 r/s).

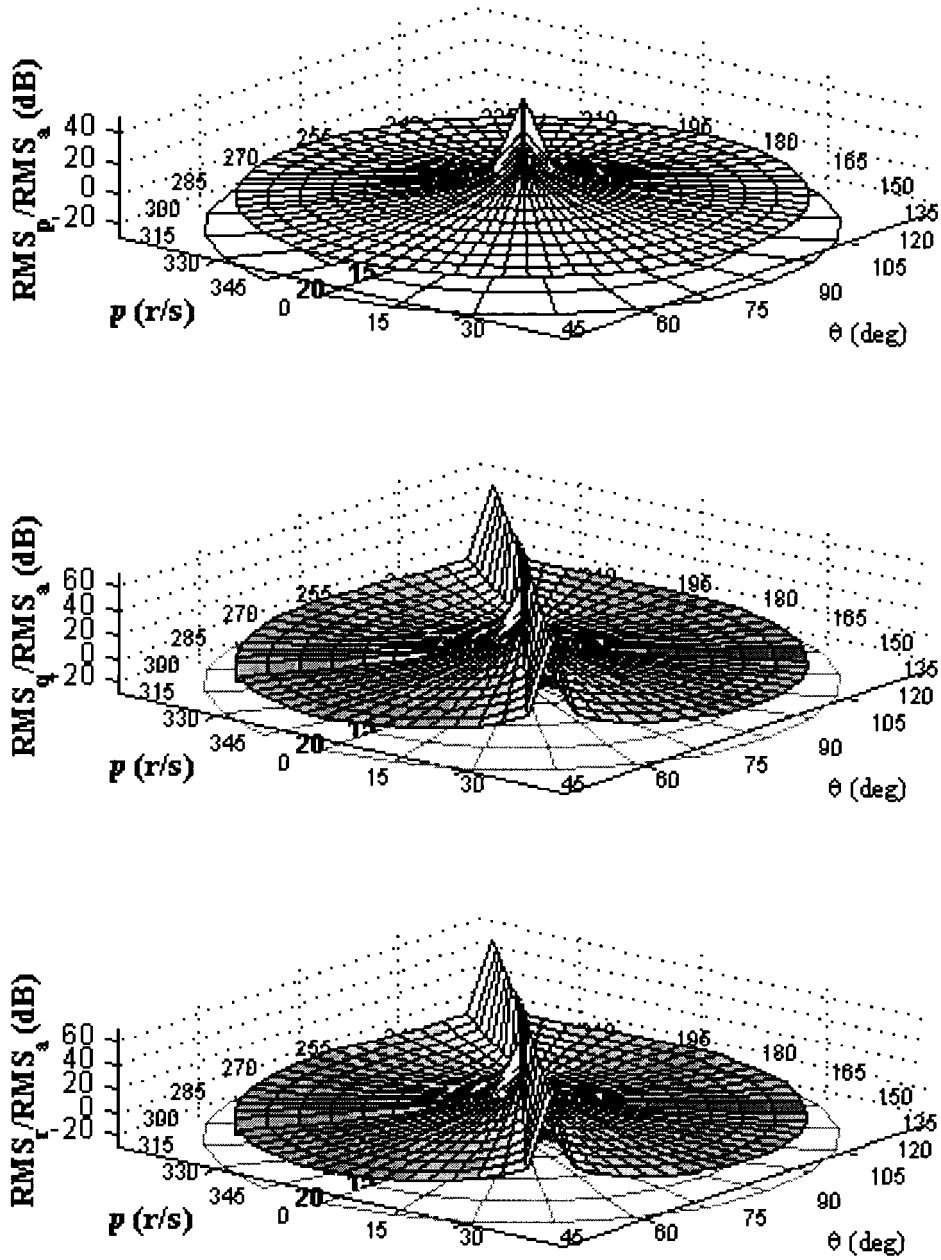

Figure 4.11 Configuration T Error Sensitivity Ratio versus Roll Rate and Sensor Constellation Angle (q = 1 r/s, r = 1 r/s).

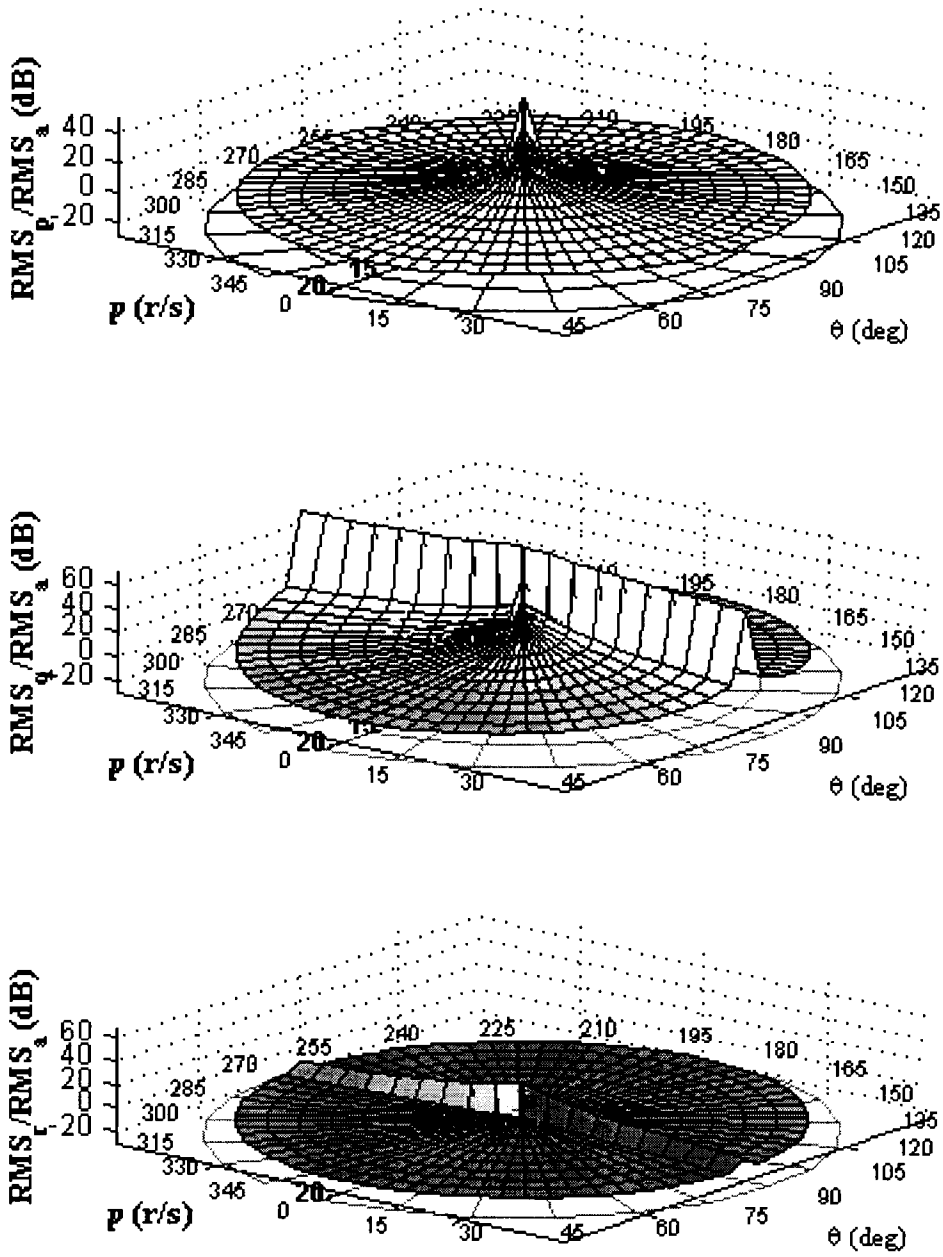

Figure 4.12 Configuration T Error Sensitivity Ratio versus Roll Rate and Sensor Constellation Angle (q = 0 r/s, r = 1.414 r/s).

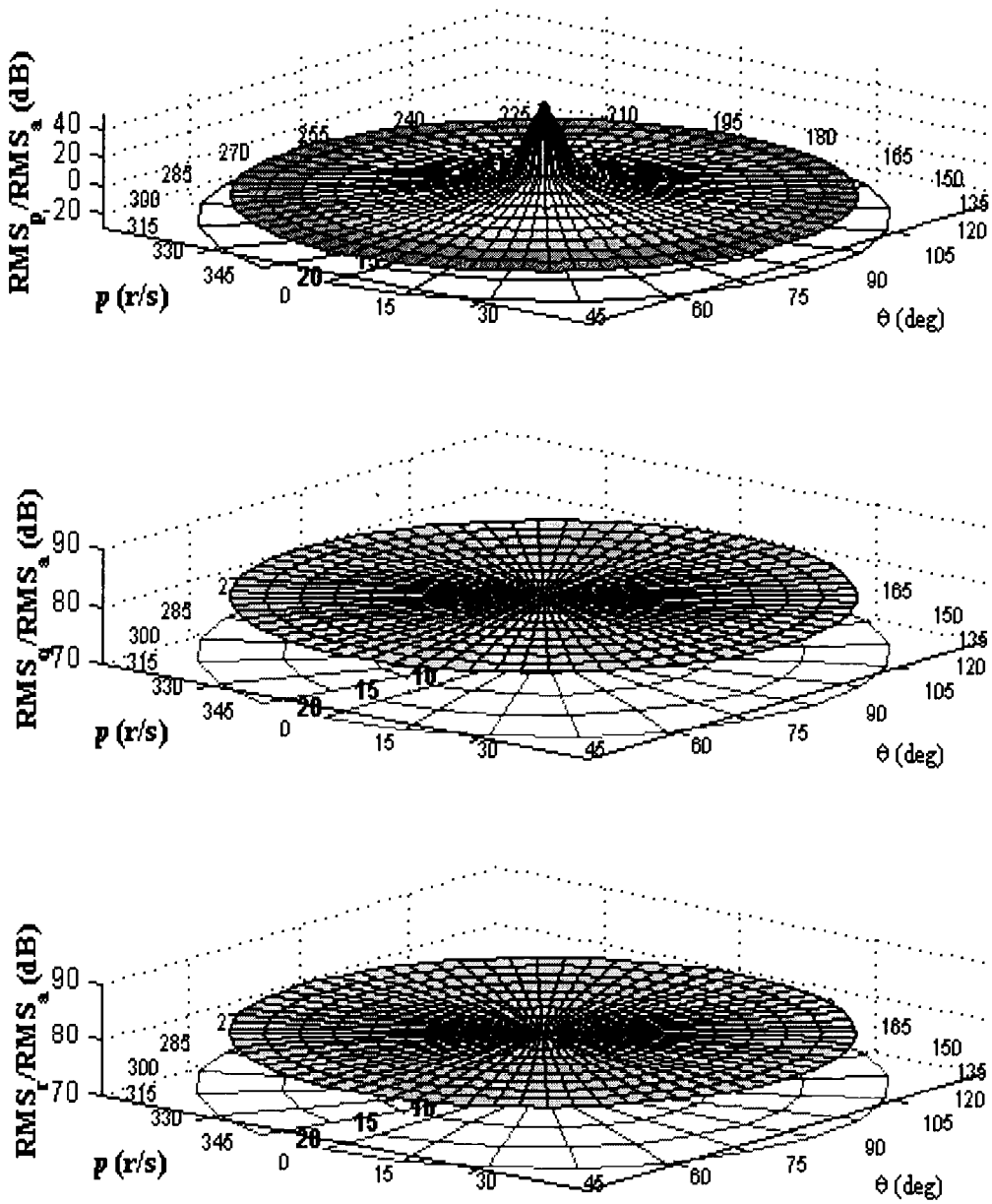

Figure 4.13 Configuration O Error Sensitivity Ratio versus Roll Rate and Sensor Constellation Angle (q = 0.0001 r/s, r = 0.0001 r/s).

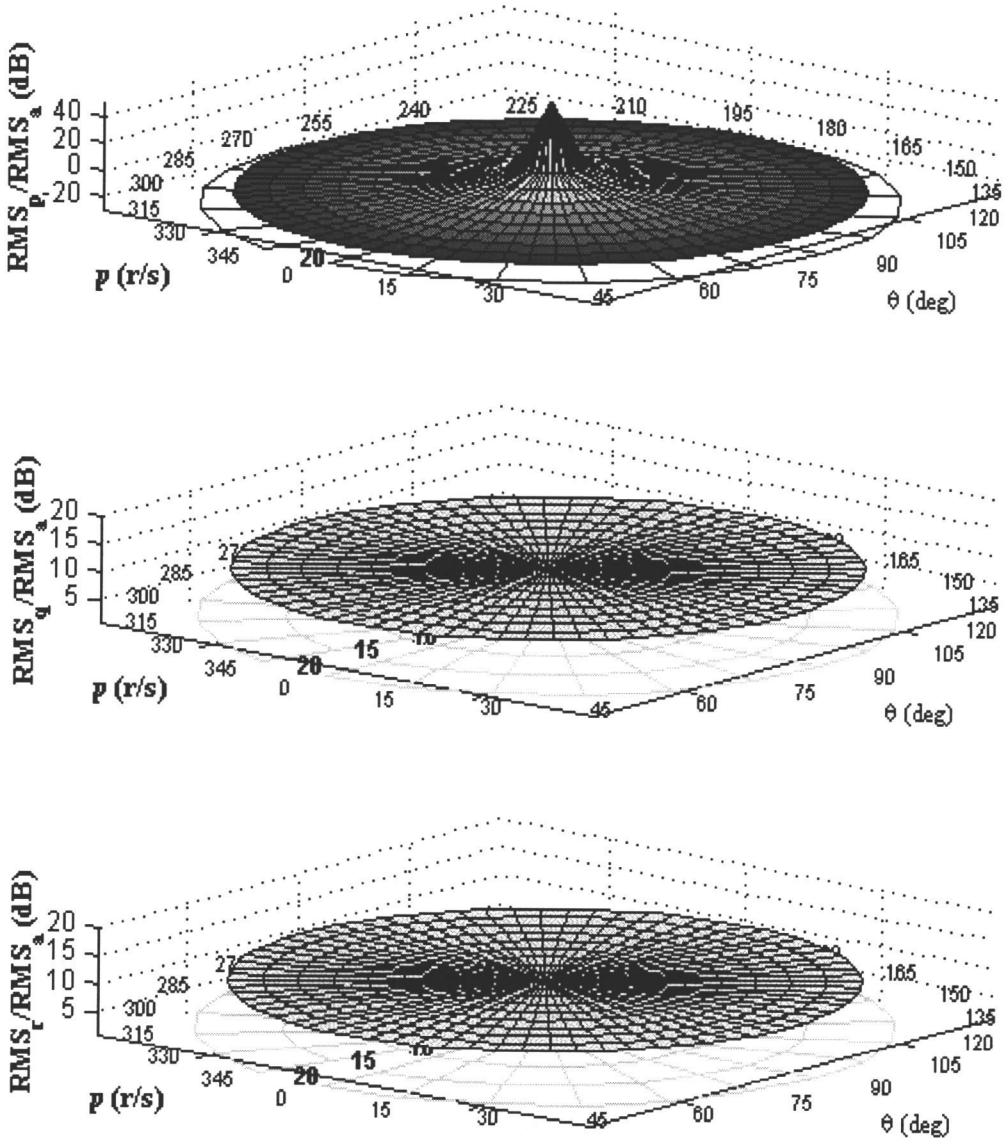

Figure 4.14 Configuration O Error Sensitivity Ratio versus Roll Rate and Sensor Constellation Angle (q = 1 r/s, r = 1 r/s).

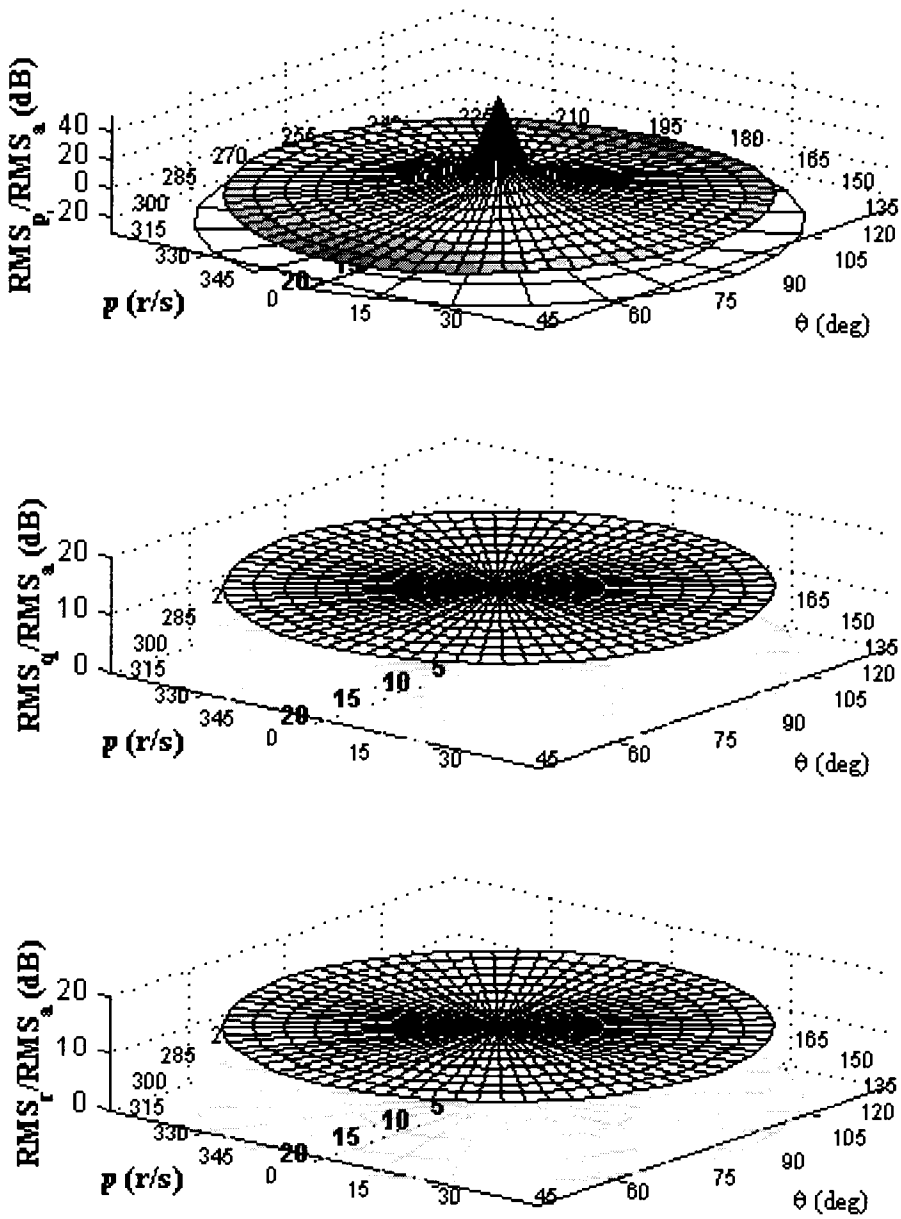

Figure 4.15 Configuration O Error Sensitivity Ratio versus Roll Rate and Sensor Constellation Angle (q = 0 r/s, r = 1.414 r/s)

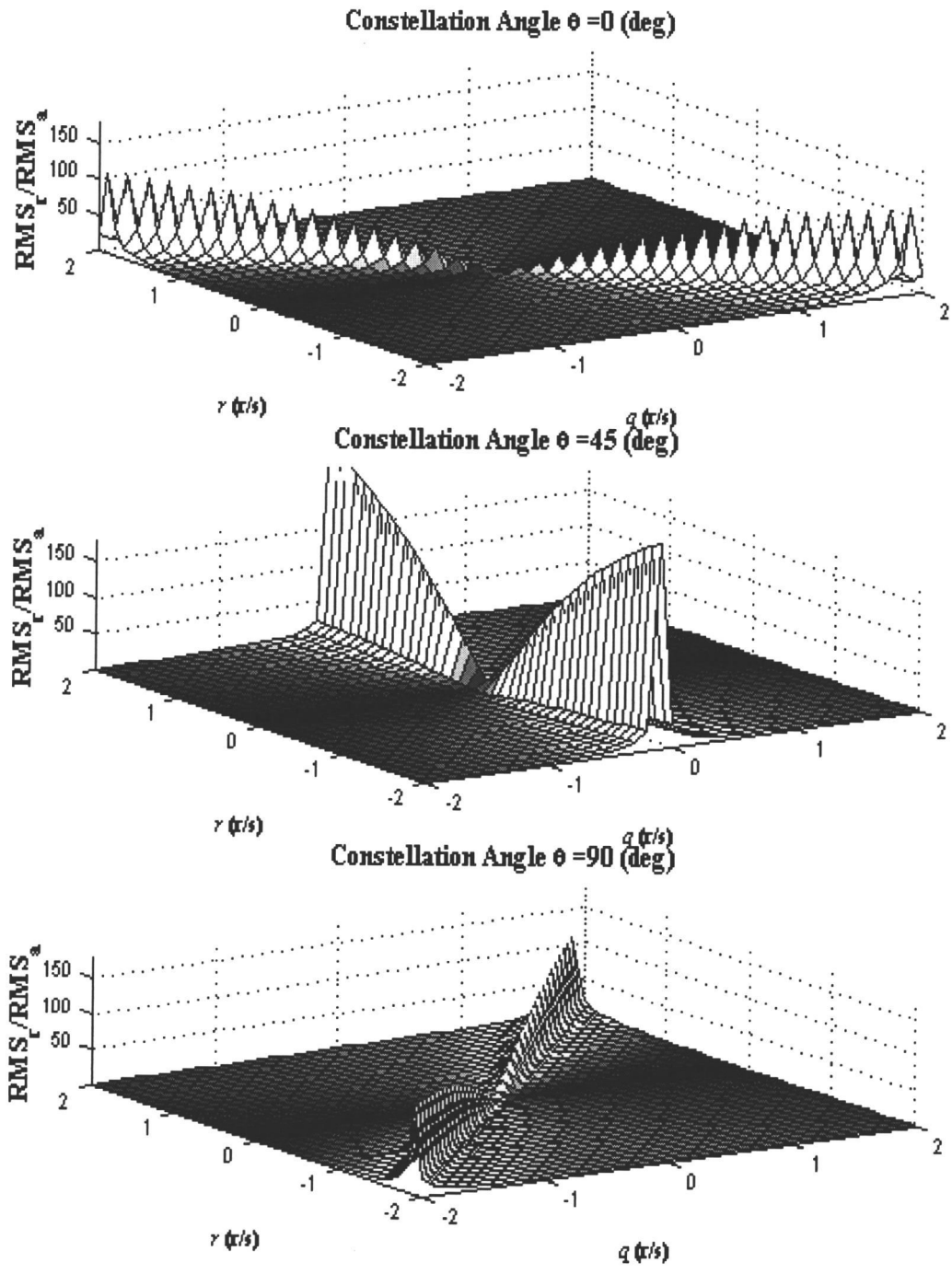

Figure 4.16 Error Sensitivity of Yaw Rate versus Pitch and Yaw Rate for $\theta = 0, 45, 90^{\circ}$.

4.4 Skin Mounted Triaxial Acceleration Measurement Sensor Fusion

The algorithms discussed above can be employed to estimate angular rates and acceleration of a projectile with an array of sensors mounted on the skin of the body. The sensor suite is composed of n rings of sensors with each ring containing m sensors where the sensors in a ring are equally spaced azimuthally. A schematic is shown in Figure 4.17.

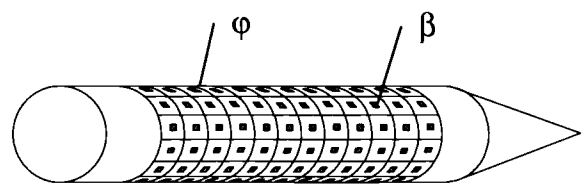

Figure 4.17 Acceleration Measurement Sensor Configuration.

With a large number of triaxial acceleration measurements available, several different options are possible to fuse the sensor data together. At one extreme, all acceleration measurements are used to estimate the M matrix defined above, followed by computation of the angular velocity and acceleration components using Equations (4.39) through (4.44). At the other extreme, l groups of three point measurements are used to calculate l different predictions of the angular velocity and acceleration components using Equations (4.33) through (4.38). Median values of the l estimated parameters are used to determine the final estimated value for a parameter. The l sensor clusters are randomly selected except for the constraint that the distance matrix , R, is full rank.

Figures 4.18 through 4.23 provide estimation results for a trajectory of a generic direct fire rocket in atmospheric flight. The rocket trajectory shown in the results to follow has been generated from a 6 degree of freedom projectile simulation. Normally distributed random noise, with a standard deviation of 0.1 ft/s^2, is added to each acceleration measurement to replicate actual noisy sensors. The signals are also quantized using 64 floating point bits to account for analog to digital conversion (Stoer and Bulirsh, 1992). Direct fire rockets generally possess a very predictable roll rate time history, thus the algebraic sign of the angular rates is computed assuming the algebraic sign of roll rate is known. The angular velocity and acceleration components are estimated using a single cluster of 80 triaxial sensors. For this typical example, roll rate and all angular acceleration components are estimated accurately over the entire trajectory in the presence of noise and quantization. However, the pitch and yaw rate estimations are notably less accurate. In particular, when pitch and yaw rate is small, the estimation errors are relatively large. Conversely, when the pitch and yaw rates are largest, the estimation is reasonably accurate.

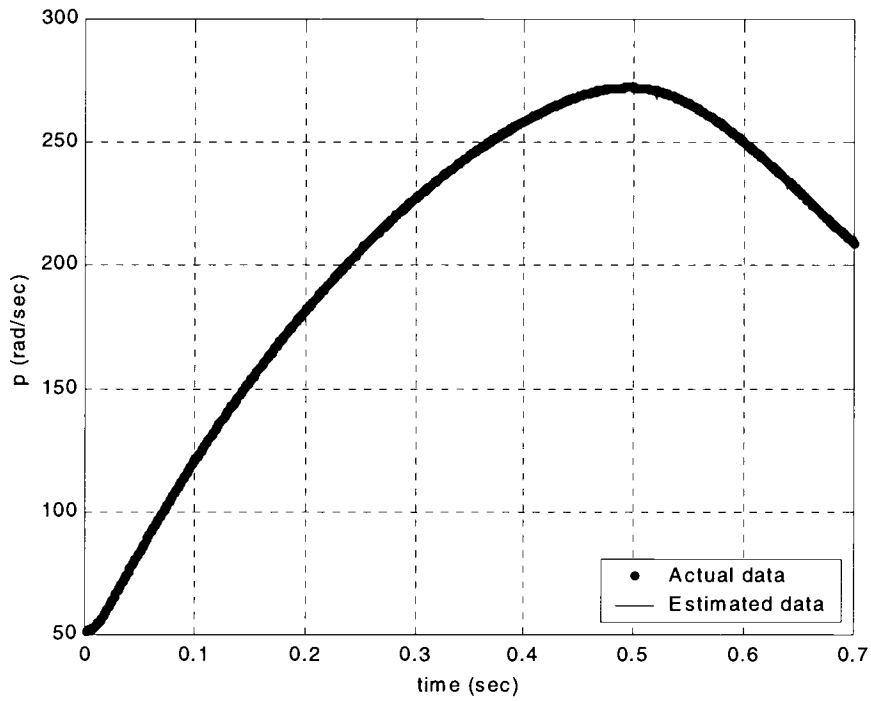

Figure 4.18 Actual and Estimated Roll Rate versus Time.

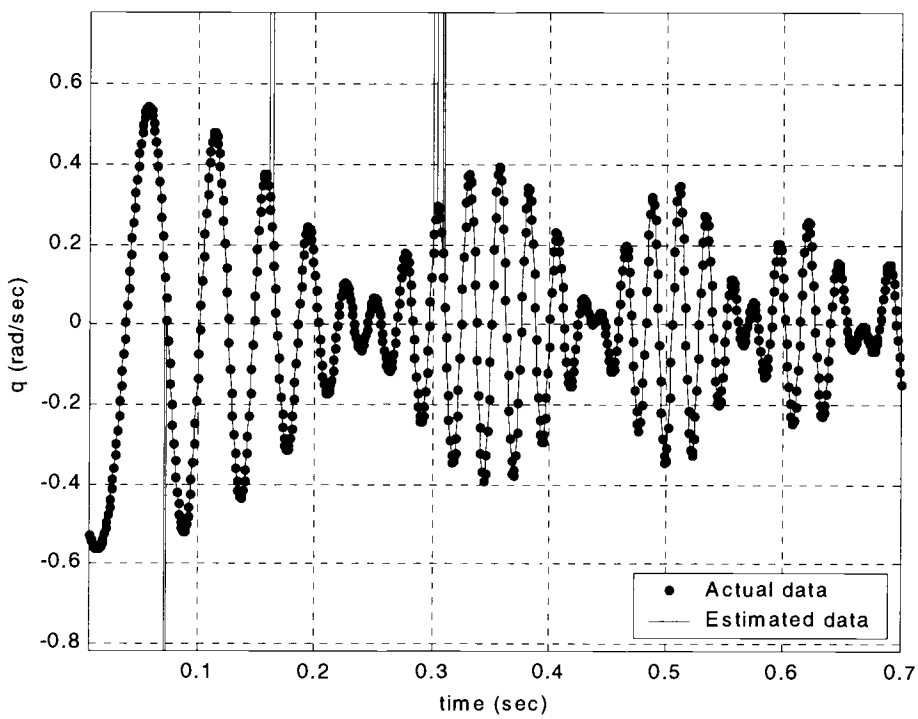

Figure 4.19 Actual and Estimated Pitch Rate versus Time.

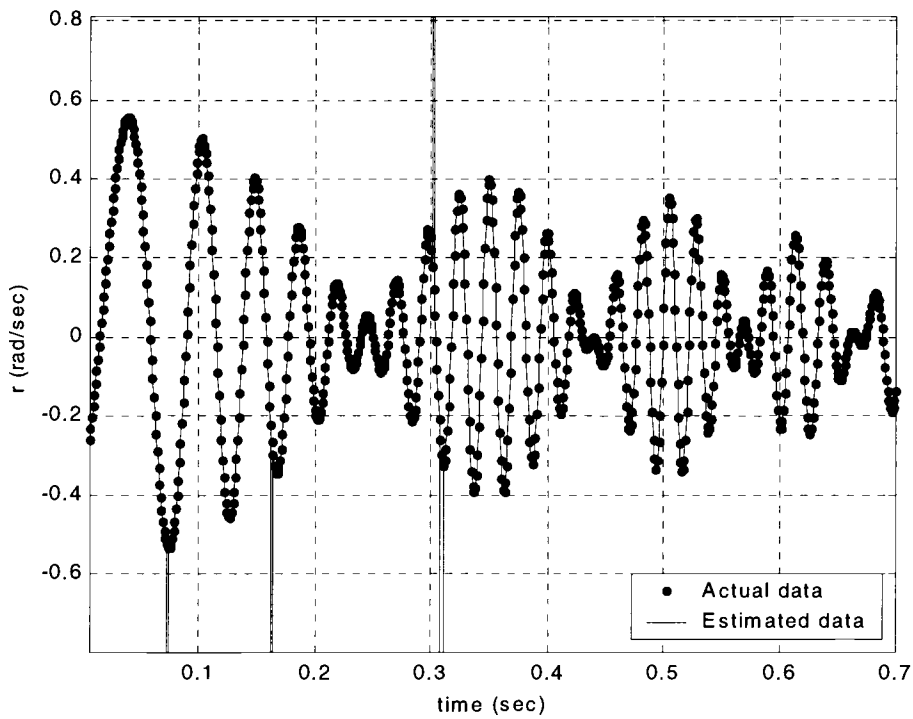

Figure 4.20 Actual and Estimated Yaw Rate versus Time.

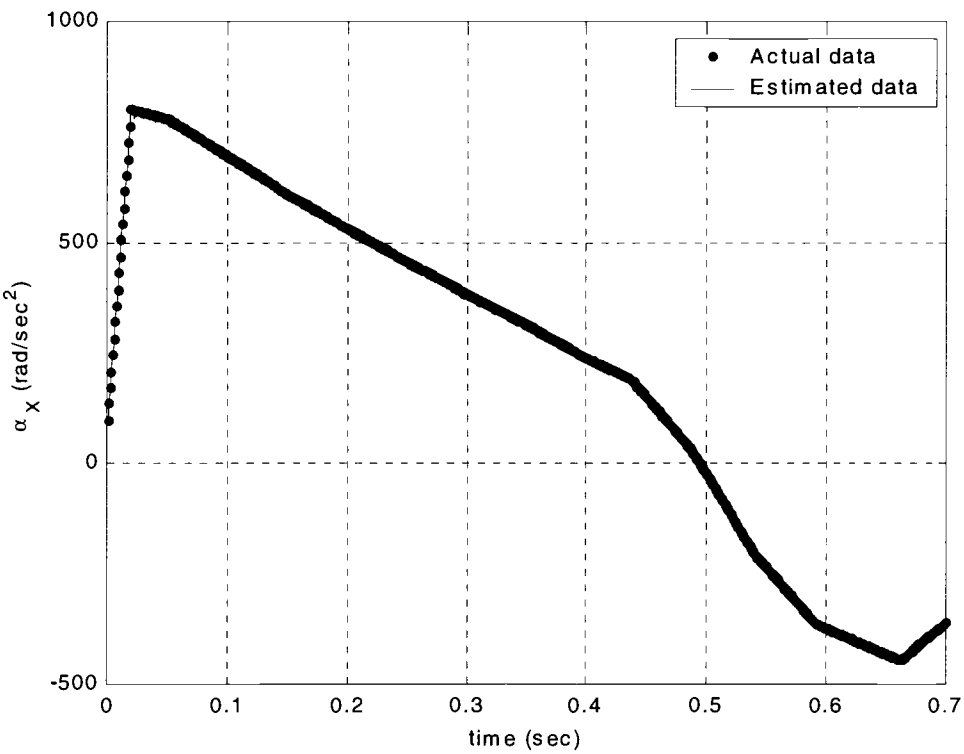

Figure 4.21 Actual and Estimated Roll Acceleration versus Time.

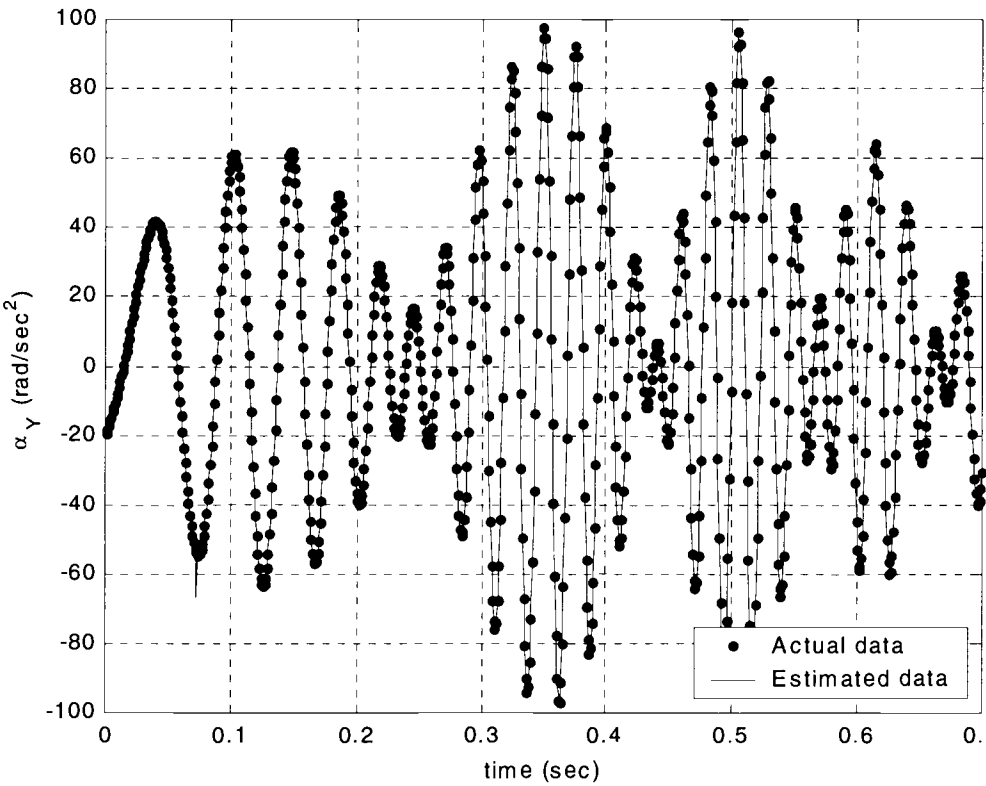

Figure 4.22 Actual and Estimated Pitch Acceleration versus Time.

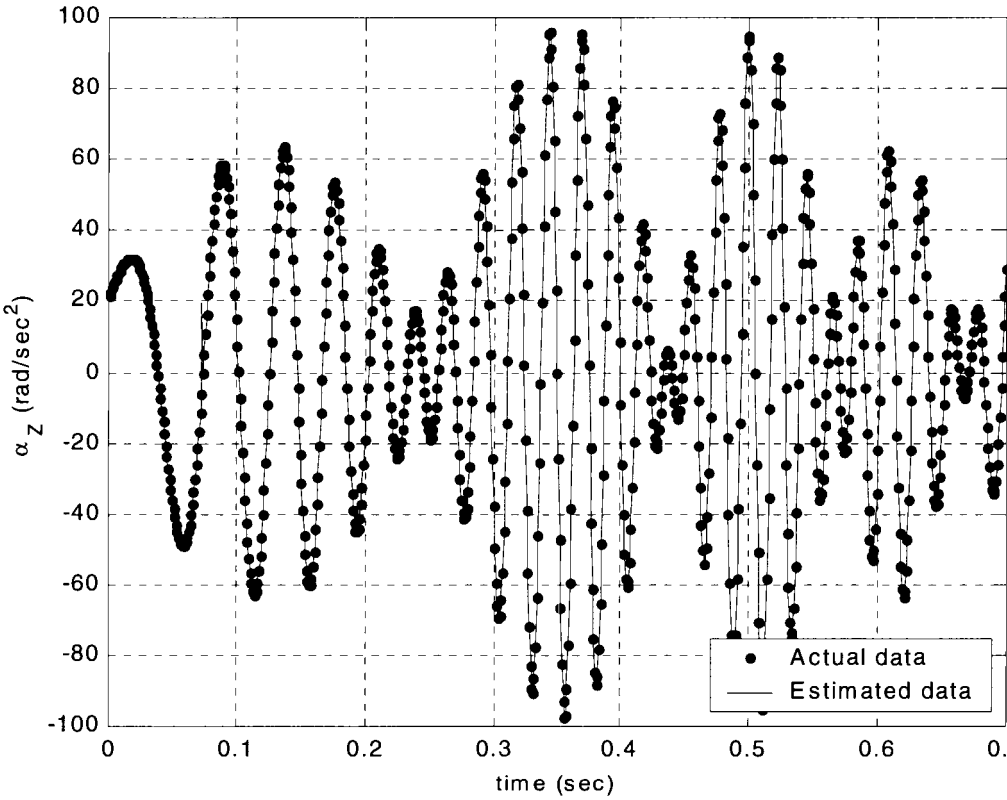

Figure 4.23 Actual and Estimated Yaw Acceleration versus Time.

Figures 4.24 through 4.26 investigate the errors encountered in estimating pitch rate for different sensor configurations. For these figures, the average absolute value of the error between the actual and estimated pitch rate over the entire trajectory is reported. Figure 4.24 plots the average pitch rate error as a function of the total number of sensors mounted on the projectile skin. As would be expected, as the number of sensors in increased, either from increasing the number of sensor rings or increasing the number of sensors per ring, pitch rate estimation steadily improves. Figure 4.25 plots the average pitch rate error versus the number of sensor clusters employed in the estimation process. Note that the total number of sensors is held constant in Figure 4.25, only the manner in which the sensor data is utilized is changed. Figure 4.25 suggests that the best sensor fusion strategy is one sensor cluster that contains all the sensors. Thus, the minimum error is found by utilizing all the sensor data to most accurately compute the M matrix. The estimation algorithm tends to magnify errors. Figure 4.26 plots the average pitch rate error versus the number of bits used when converting the acceleration measurement data to digital form. The average pitch rate error is a strong function of acceleration measurement quantization. Furthermore, the error reduces sharply until 16 bits and then reduces at a lower rate as the number of bits is further increased. For direct fire rocket applications, acceleration quantization should be performed at no less than 16 bits.

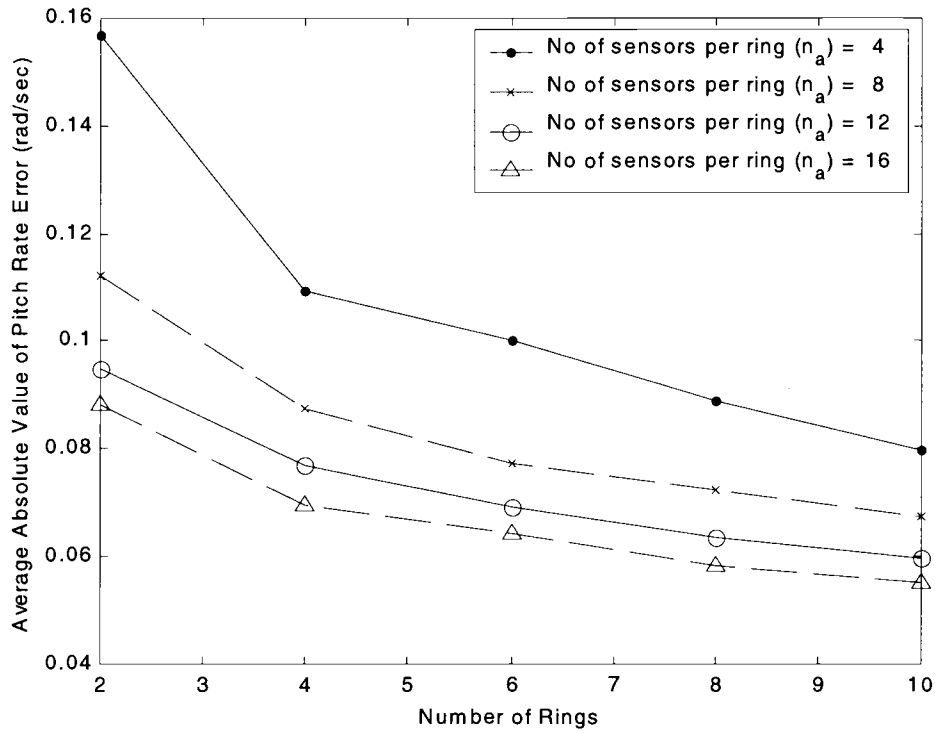

Figure 4.24 Average Error Magnitude versus Sensor Configuration.

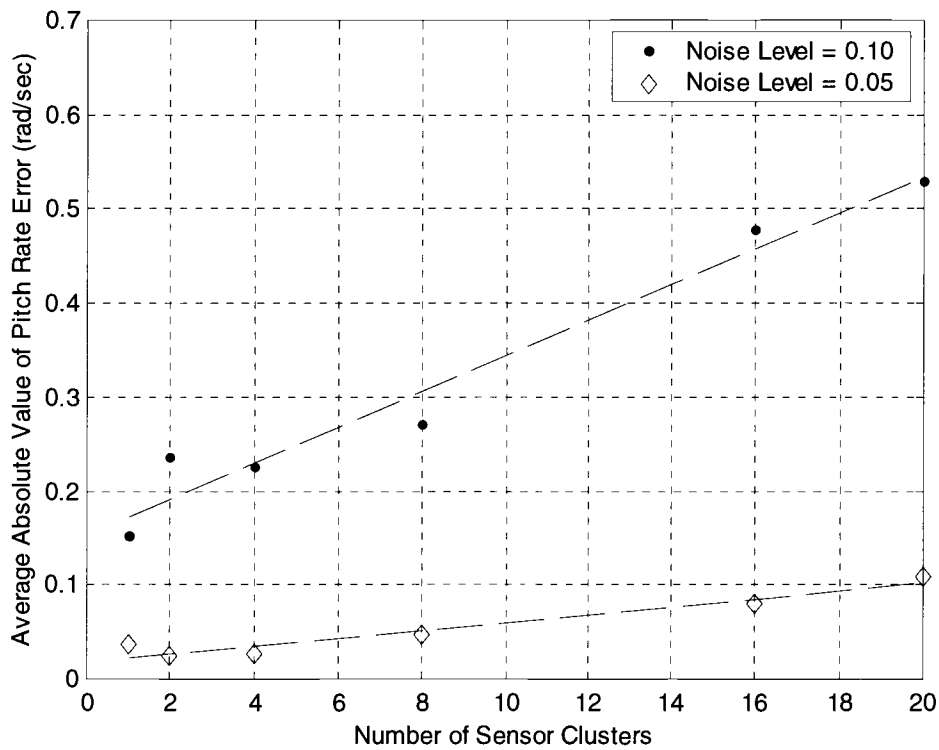

Figure 4.25 Average Error Magnitude versus Sensor Fusion Technique.

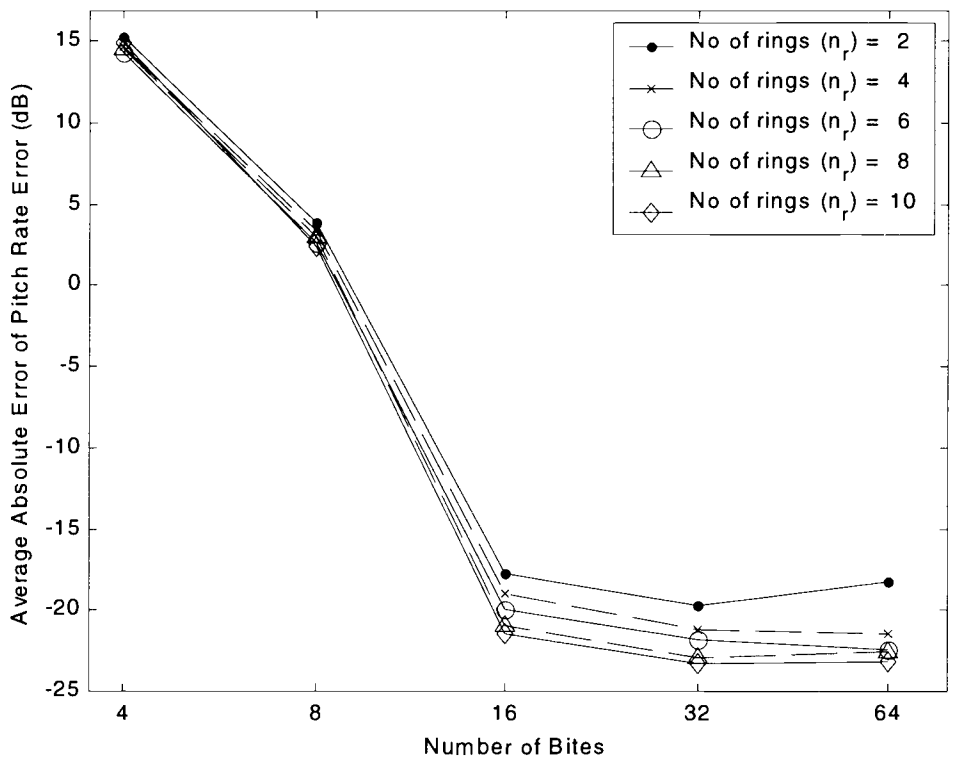

Figure 4.26 Average Error Magnitude versus Quantization Level.

CHAPTER 5
LATERAL PULSE JET CONTROL LAWS

In this thesis, two different control laws are considered for application to a direct fire rocket flight control law. The first control law algorithm seeks to track a commanded trajectory. Pulse jet firing is based on the position error between the commanded and IMU estimate of the actual position. The second technique is a proportional navigation guidance flight control law modified to account for trajectory bending due to gravity. Pulse jet firing is based on the line of sight rate and the closing velocity.

5.1 Trajectory Tracking Flight Control System

A predetermined command trajectory is assumed to be known prior the launch of the rocket. This command trajectory is a desired path of the rocket from the launcher to the target. The flight control system seeks to track a pre-specified command trajectory utilizing the control authority provided by the lateral pulse jets. It requires two procedures in the implementation: (1) the determination of off-axis trajectory tracking error and (2) the control decision using firing logic.

5.1.1 Off-axis Trajectory Error

A schematic of the flight control system block diagram is shown in Figure 5.1.

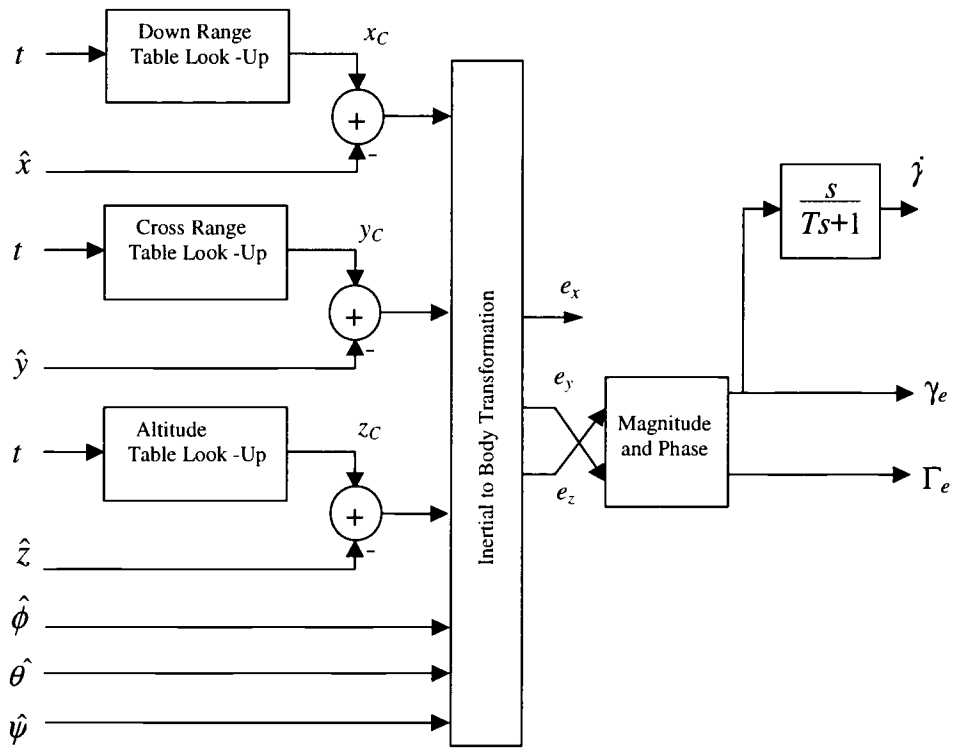

Figure 5.1 Trajectory Tracking Flight Control System.

For direct fire rockets, a command ballistic trajectory is available from the fire control system and can be downloaded to the round just prior to launch. The trajectory tracking flight control system first compares the measured position of the projectile ($\hat{x}, \hat{y}, \hat{z}$) to the commanded trajectory (x_C, y_C, z_C) to form a position error vector in the inertial frame. The trajectory error is converted to the rocket body frame using Equation (5.1).

$$\begin{Bmatrix} e_X \\ e_Y \\ e_Z \end{Bmatrix} = \begin{bmatrix} c_{\hat{\theta}}c_{\hat{\psi}} & c_{\hat{\theta}}s_{\hat{\psi}} & -s_{\hat{\theta}} \\ s_{\hat{\phi}}s_{\hat{\theta}}c_{\hat{\psi}} - c_{\hat{\phi}}s_{\hat{\psi}} & s_{\hat{\phi}}s_{\hat{\theta}}s_{\hat{\psi}} + c_{\hat{\phi}}c_{\hat{\psi}} & s_{\hat{\phi}}c_{\hat{\theta}} \\ c_{\hat{\phi}}s_{\hat{\theta}}c_{\hat{\psi}} + s_{\hat{\phi}}s_{\hat{\psi}} & c_{\hat{\phi}}s_{\hat{\theta}}s_{\hat{\psi}} - s_{\hat{\phi}}c_{\hat{\psi}} & c_{\hat{\phi}}c_{\hat{\theta}} \end{bmatrix} \begin{Bmatrix} x_C - \hat{x} \\ y_C - \hat{y} \\ z_C - \hat{z} \end{Bmatrix} = [T_I^B] \begin{Bmatrix} x_C - \hat{x} \\ y_C - \hat{y} \\ z_C - \hat{z} \end{Bmatrix} \quad (5.1)$$

The magnitude and phase angle of the error in the off-axis plane of the rocket are denoted Γ_e and γ_e, and are defined by Equations (5.2) and (5.3), respectively. The error magnitude is used in the firing decision and the error phase angle is used in the selection of pulse jet to be fired.

$$\Gamma_e = \sqrt{e_Y^2 + e_Z^2} \quad (5.2)$$

$$\gamma_e = \tan^{-1}(e_Z / e_Y) \quad (5.3)$$

5.1.2 Control Firing Logic

A schematic diagram of the lateral pulse jet firing logic is given in Figure 5.2.

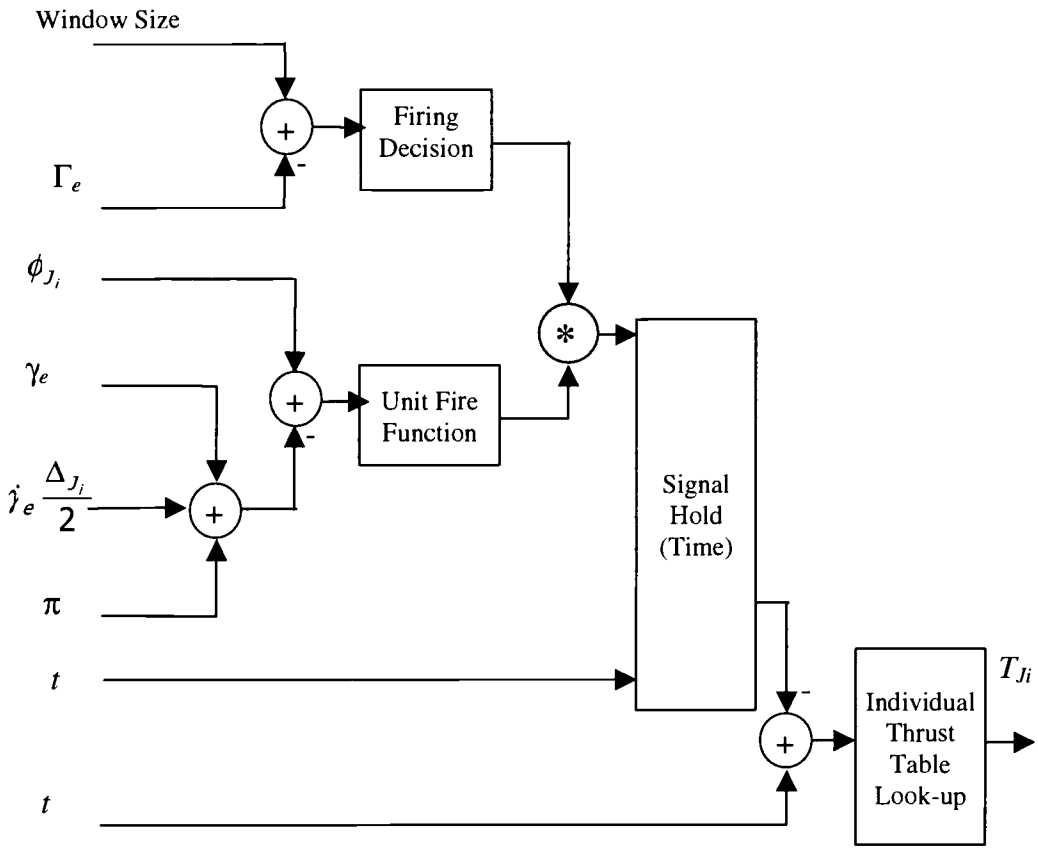

Figure 5.2 i^{th} Individual Lateral Pulse Jet Firing Logic.

At each computation cycle in the flight control system, a sequence of checks are conducted that govern firing of individual lateral pulse jets. The conditions that must be satisfied for an individual lateral pulse jet to fire are as follows.

A) The magnitude of the off-axis trajectory tracking error must be greater than a specified distance, namely *tracking window size,* e_{THRES}.

$$\Gamma_e > e_{THRES} \tag{5.4}$$

B) The time elapsed since the last lateral pulse jet firing must be greater than a specified duration. This condition implies a specified delay time between two consecutive firings is necessary.

$$t - t^* > \Delta t_{THRES} \tag{5.5}$$

where

t^* - Time of the most recent jet firing.

C) The projected angle between the trajectory tracking error and the individual pulse jet force under consideration is less than a specified angle.

$$\left| \phi_{J_i} - \pi - \gamma_e - \dot{\gamma}_e \frac{\Delta_{J_i}}{2} \right| < \delta_{THRES} \tag{5.6}$$

D) The individual pulse jet under consideration has not been fired.

The first two checks are valid for all lateral pulse jets while the last two checks are specific to a given lateral pulse jet. The flight control system contains only three parameters that must be tuned to a specific application, the tracking error window size (e_{THRES}), the required elapsed time between pulse jet firings (Δt_{THRES}), and the angle tolerance between the tracking error and the individual pulse jet force (δ_{THRES}).

5.2 Parabolic Proportional Navigation Guidance Law

Proportional Navigation Guidance (PNG) technique is well known in tactical and strategic missile design since World War II (Zarchan, 1990). PNG issues command accelerations that are calculated instantaneously during flight to a

target. Consider a line of sight (LOS) that is always directed from the missile to the target. The determined command accelerations are proportional to the LOS angular rate, $\dot{\lambda}$, and the missile closing velocity, V_C. Mathematically the guidance law can be stated as shown in Equation (5.7).

$$A_C = N' V_C \dot{\lambda} \tag{5.7}$$

In Equation (5.7) N' is the unitless proportional navigation constant that is typically chosen between 3 to 5 (Zarchan, 1990).

5.2.1 Horizontal Plane Guidance Law

Consider point P and T in a horizon plane as shown in Figure 5.3. Point P represents a moving projectile that is fired from a launcher towards a target at point T. The position of the target with respect to the inertial reference frame is defined by Equation (5.8)

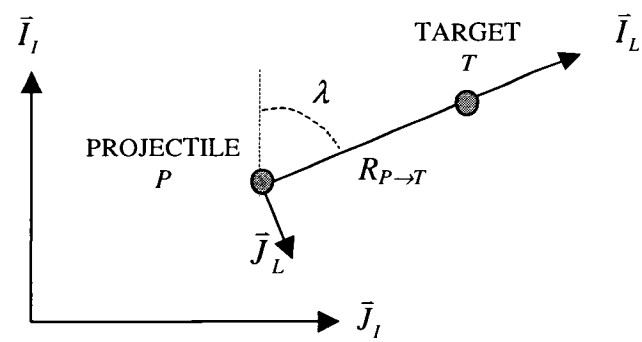

Figure 5.3 Line of Sight Frame Configuration.

$$\vec{r}_{T/I} = x_T \vec{I}_I + y_T \vec{J}_I + z_T \vec{K}_I \tag{5.8}$$

The magnitude of the distance from the projectile to the target that is projected on a horizontal plane is given by Equation (5.9).

$$R_{P\to T} = \sqrt{(x_T - \hat{x})^2 + (y_T - \hat{y})^2} \tag{5.9}$$

where the position of the projectile is the IMU estimation and is given by $\vec{r}_{P/I} = \hat{x}\vec{I}_I + \hat{y}\vec{J}_I + \hat{z}\vec{K}_I$.

The LOS frame $(\vec{I}_L, \vec{J}_L, \vec{K}_L)$ is defined with its origin at point P. The $\vec{I}_L$ unit vector lies along the horizontal plane projection of the line between the projectile and the target. The $\vec{J}_L$ unit vector lies on the horizontal plane and the $\vec{K}_L$ points down toward the Earth's center. The relationship between the inertial reference frame and the LOS frame is given by a rotation matrix defined by Equation (5.10),

$$\begin{Bmatrix} I_I \\ J_I \\ K_I \end{Bmatrix} = \begin{bmatrix} c_\lambda & -s_\lambda & 0 \\ s_\lambda & c_\lambda & 0 \\ 0 & 0 & 1 \end{bmatrix} \begin{Bmatrix} I_L \\ J_L \\ K_L \end{Bmatrix} = [T_L^I] \begin{Bmatrix} I_L \\ J_L \\ K_L \end{Bmatrix} \tag{5.10}$$

where the LOS angle λ is determined by Equation (5.11).

$$\lambda = \tan^{-1}\left(\frac{y_T - \hat{y}}{x_T - \hat{x}} \right) \tag{5.11}$$

The time derivative of Equation (5.11) provides the rate of change of λ.

$$\dot{\lambda} = \frac{-\dot{\hat{y}}(x_T - \hat{x}) + \dot{\hat{x}}(y_T - \hat{y})}{(R_{P\to T})^2} \tag{5.12}$$

Equation (5.12) has been simplified with the assumption that the target is stationary. The horizontal acceleration command magnitude is given by Equation (5.13).

$$A_{YC} = N'\dot{\lambda}u_L \tag{5.13}$$

$$\begin{Bmatrix} u_L \\ v_L \\ w_L \end{Bmatrix} = \begin{bmatrix} c_\lambda & s_\lambda & 0 \\ -s_\lambda & c_\lambda & 0 \\ 0 & 0 & 1 \end{bmatrix} \begin{Bmatrix} \dot{\hat{x}} \\ \dot{\hat{y}} \\ \dot{\hat{z}} \end{Bmatrix} \tag{5.14}$$

Figure 5.4 shows the flight control system block diagram of the horizontal guidance law.

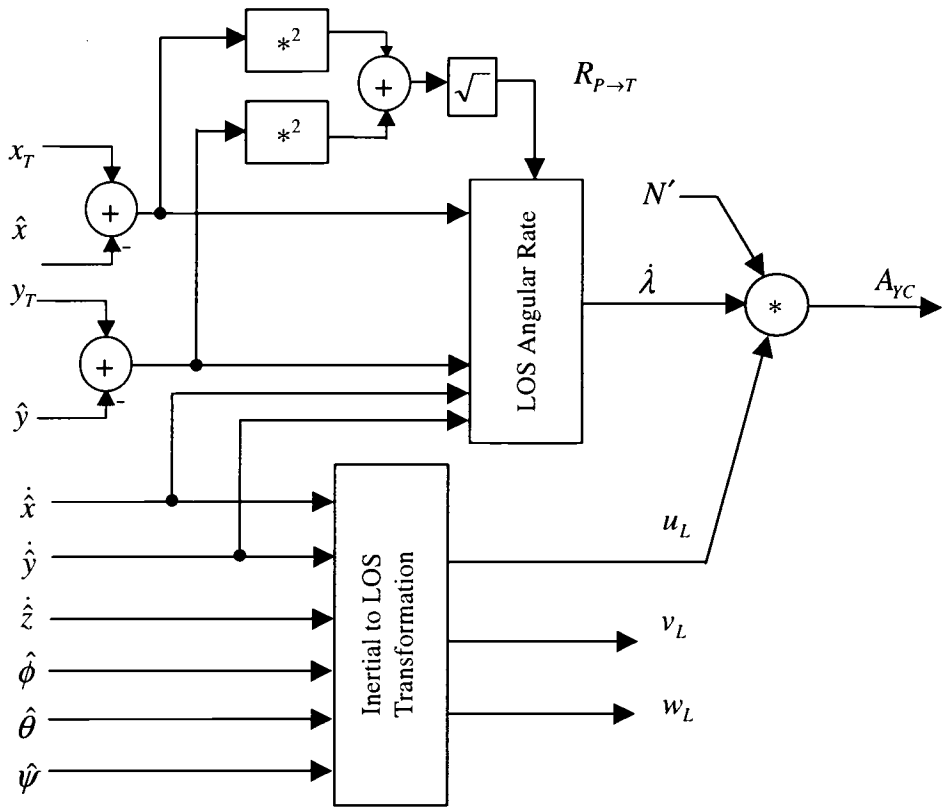

Figure 5.4 Proportional Navigation Guidance Law for the Horizontal Flight Control.

5.2.2 Vertical Plane Guidance Law

A parabolic guidance law is considered in the determination of command acceleration in the vertical LOS plane to compensate the weight force of the rocket. A desired parabolic trajectory is continuously updated during the flight. Figure 5.5 shows the desired parabolic trajectory that is also described by Equation (5.15) (Calise and El-Shirbiny, 2001).

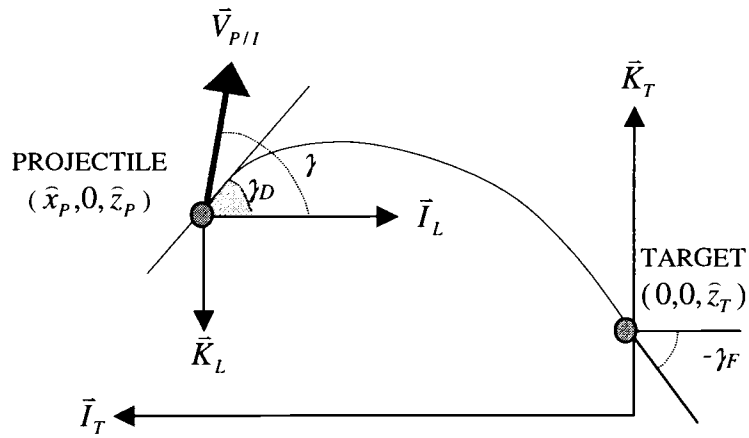

Figure 5.5 Parabolic trajectory in the LOS frame.

$$\hat{z}_P = \hat{z}_T + K_1 \hat{x}_P + K_2 \hat{x}_P^{\,2} \tag{5.15}$$

where

$\hat{x}_P, \hat{z}_P, \hat{z}_T$ - components of the projectile position and the target position that are defined in a target frame $(\vec{I}_T, \vec{J}_T, \vec{K}_T)$. The $\vec{K}_T$ axis crosses the target point. The vectors $\vec{I}_T$ and $\vec{K}_T$ are parallel but in opposite directions to $\vec{I}_L$ and $\vec{K}_L$.

K_1, K_2 - parabolic constants.

The desired flight path angle, γ_D, is determined by Equation (5.16).

$$\tan(\gamma_D) = \frac{d\hat{z}_P}{d\hat{x}_P} = K_1 + 2K_2 R_{P\to T} \tag{5.16}$$

One parabolic constant is determined by forcing the parabolic trajectory passes through both the position of the projectile and the position of the target. The other parabolic trajectory constant is computed by specifying the terminal flight path angle. The terminal flight path angle occurs when the projectile impacts the target and can be determined using available command ballistic trajectory calculated prior the launch.

$$K_1 = \tan(\gamma_F) \tag{5.17}$$

$$K_2 = \frac{-(K_1 R_{P\to T} + \hat{z}_T - \hat{z}_P)}{R_{P\to T}^{\ 2}} \tag{5.18}$$

The guidance command acceleration in the vertical LOS plane is determined by Equation (5.19). Figure 5.6 shows the diagram of the vertical guidance law.

$$A_{ZC} = \frac{V_L(\gamma_D - \gamma)}{\tau} \tag{5.19}$$

where

V_L – Magnitude of the projectile velocity in the LOS frame.

γ - Flight path angle of the projectile velocity in the LOS frame.

τ - Acceleration command time constant.

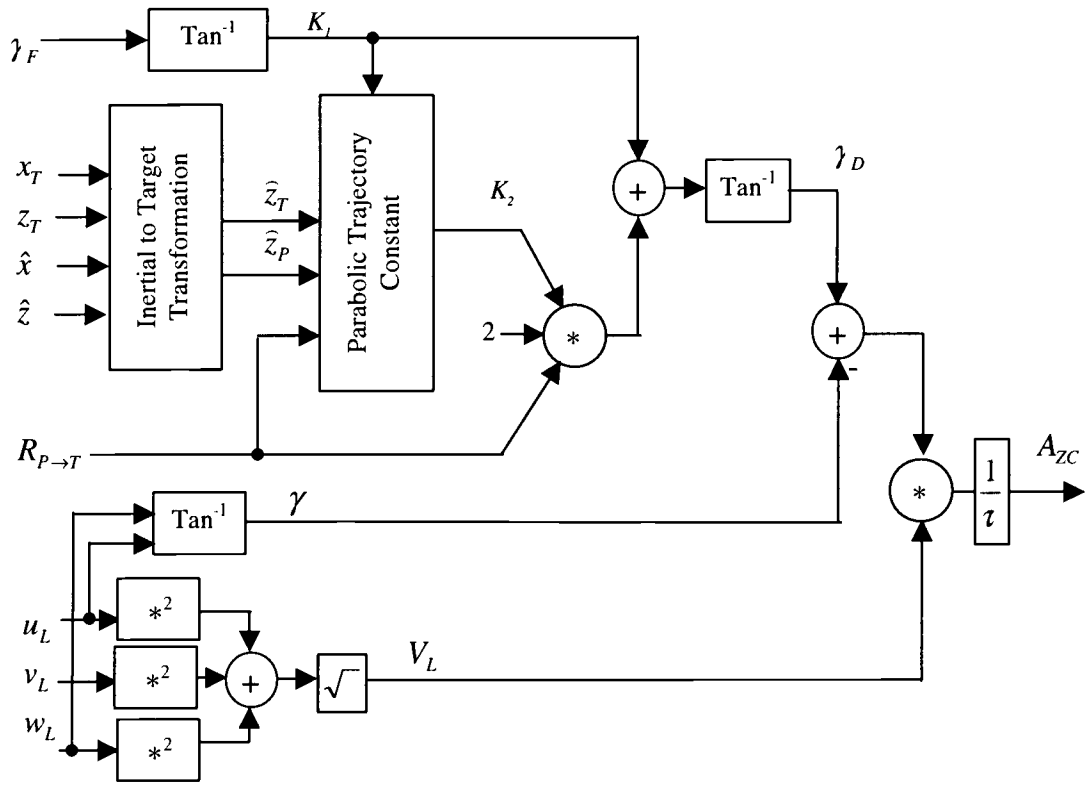

Figure 5.6 Parabolic Proportional Navigation Guidance Law for the Vertical Control.

The acceleration command in the LOS frame is given in Equation (5.20). It is transformed to the body reference frame using sequences of rotations shown in Equation (5.21).

$$A_{CL} = \begin{Bmatrix} -A_{ZC}\sin(\gamma) \\ A_{YC} \\ -A_{ZC}\cos(\gamma) \end{Bmatrix} \tag{5.20}$$

$$\begin{Bmatrix} A_{X_{CB}} \\ A_{Y_{CB}} \\ A_{Z_{CB}} \end{Bmatrix} = [T_I^B][T_L^I]A_{CL} \tag{5.21}$$

The off-axis command acceleration is then decomposed into the magnitude and phase angle using Equations (5.22) and (5.23).

$$\Gamma_{AC} = \sqrt{A_{Y_{CB}}{}^2 + A_{Z_{CB}}{}^2} \tag{5.22}$$

$$\gamma_{AC} = \tan^{-1}\left(A_{Z_{CB}} / A_{Y_{CB}} \right) \tag{5.23}$$

The implementation of the guidance law to the lateral pulse jet controller requires modification of the conditions A) and C) in the control firing logic (Section 5.1.2) to the following statements:

A) Magnitude of the off-axis command acceleration must be greater than a threshold acceleration, a_{THRES}.

$$\Gamma_{AC} > a_{THRES} \tag{5.24}$$

B) The time elapsed since the last lateral pulse jet firing must be greater than a specified duration, Δt_{THRES}. This condition implies a specified delay time between two consecutive firings is necessary.

$$t - t^* > \Delta t_{THRES} \tag{5.5}$$

where

t^* - Time of the most recent jet firing.

C) Projected angle between the off axis command acceleration and the individual pulse jet force under consideration is less than a specified angle, δ_{THRES}.

$$\left| \phi_{J_i} - \pi - \gamma_{AC} - \dot{\gamma}_{AC} \frac{\Delta_{J_i}}{2} \right| < \delta_{THRES} \tag{5.25}$$

where $\dot{\gamma}_{AC}$ is the time derivative of the γ_{AC}.

D) The individual pulse jet under consideration has not been fired.

The diagram of the parabolic propotional navigation guidance control firing logic is shown in Figure 5.7.

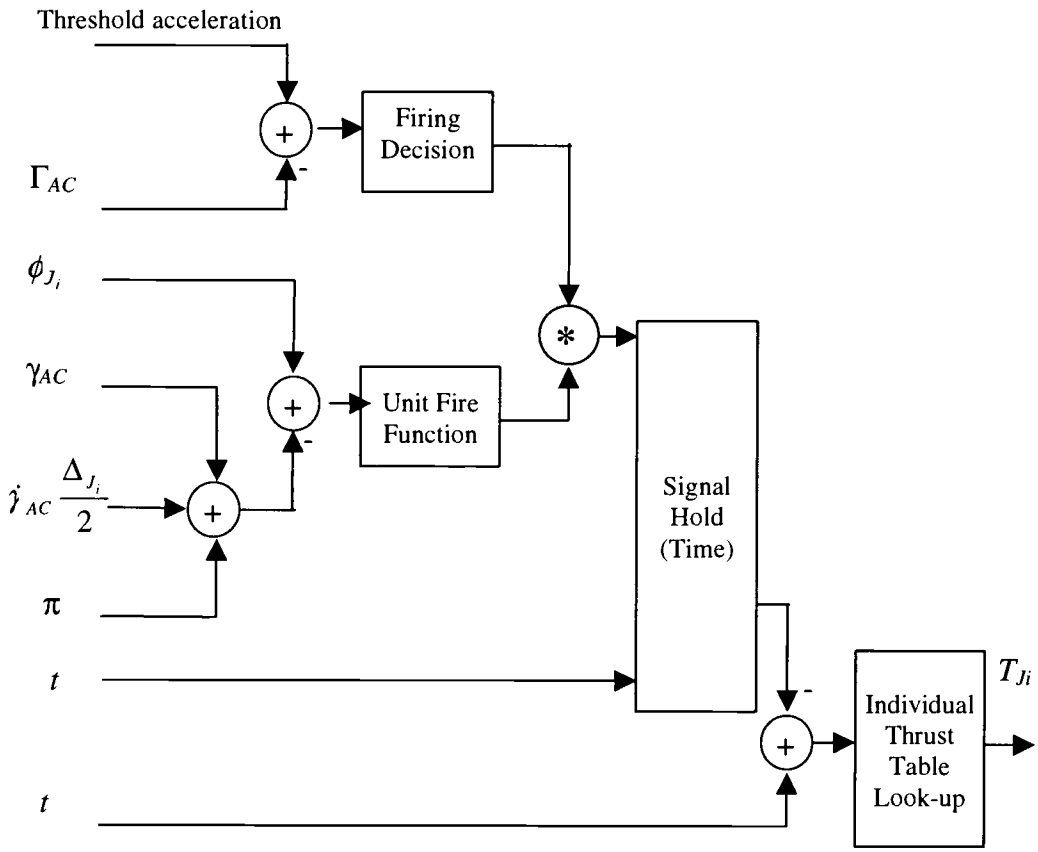

Figure 5.7 i^{th} Individual Lateral Pulse Jet Firing Logic.

5.3 Comparison of Control Laws

To investigate the ability of a lateral pulse jet ring to reduce impact point dispersion, the equations of motion described above are numerically integrated using an adaptive step-size Runge-Kutta algorithm. The rocket configuration used in the simulation study to follow is a representative direct fire rocket that is a 1.4 m long, fin stabilized rocket with three pop out fins on the rear of the round. The lateral pulse jet ring is located 1.16 m from the base of the rocket. The main rocket motor burns for 1.12 sec and imparts an impulse to the rocket of 6,212 N-s. During the main rocket motor burn, the forward velocity of the rocket is increased from 43.7 m/s to 767.5 m/s. The rocket weight, mass center location from the base of the rocket, roll inertia, and pitch inertia before and after burn is 10.4/7.21 kg, 0.85/0.86 m, 0.0077/0.0058 kg m^2, and 1.83/1.61 kg m^2, respectively. Nominally, the rocket exits the launcher with the following initial conditions: x=0.0 m, y=0.0 m, z=-30.5 m, ϕ=0.0 deg, θ=4.14 deg, ψ=0.0 deg, u=43.7 m/s, v=0.0 m/s, w=0.11 m/s, p=51.5 rad/s, q=-0.18 rad/s, and r=0.0 rad/s.

Figures 5.8 through 5.16 compare uncontrolled and controlled trajectories for the example rocket configuration against a nominal command trajectory which is the desired path of the rocket. The rocket is launched at an altitude of 30 m toward a target on the ground with altitude and cross range equal zero at a range of 3000 m. The ring contains 32 individual lateral pulse jets where each individual pulse jet imparts an impulse of 10 N-s on the projectile body over a time duration of 0.01 sec. The pulse jet elapsed time threshold is set to 0.2 sec. The pulse jet angle threshold is set to 0.2 deg. For the controlled rocket with the trajectory tracking flight control system the window size is 1.5 m. The controlled rocket with a proportional navigation flight control system has a window size setting of 6 m/s^2. These numbers are determined to be optimal numbers from trade studies where impact point dispersion was minimized. Figures 5.8 and 5.9 plot rocket altitude

and cross range versus range. At the target range of 3000 m, the uncontrolled rocket altitude error is slightly greater than 40 m while the cross range error is more than 100 m. Compared to the uncontrolled trajectory, the controlled rocket trajectory follows the commanded trajectory well for both control algorithms, with an impact error on the order of a couple meters. The off axis trajectory tracking error of the rocket with the trajectory tracking system, Γ_e, is plotted in Figure 5.10. While the uncontrolled rocket trajectory error is greater than 100 m, the trajectory tracking error for the lateral pulse jet controlled rocket remains under 3 m for the entire flight. The off axis commanded acceleration that is issued in the rocket with the proportional navigation guidance system is shown in Figure 5.11. The sequences of lateral pulse jet firing times in the trajectory tracking controlled rocket and the parabolic PNG controlled rocket are depicted in Figure 5.12. Nineteen of the possible 32 lateral pulse jets are fired in this particular example. Notice that pulses are fired at a rate that does not exceed 0.2 sec. The minimum required time between successive pulses, Δt_{THRES}, is an important design parameter of the flight control system. If Δt_{THRES} is set too low, the rocket does not have sufficient time to respond and many pulses will be fired, tending to over compensate for trajectory errors. On the other hand, if Δt_{THRES} is set too high, then only a small number of pulses can possibly be fired and control authority is wasted. In this instance, trajectory tracking will tend to build without pulse jet corrective action. The roll angle time history is shown in Figure 5.13 and it is seen that the roll response is essentially unaffected by the action of the lateral pulse jets as both the controlled and uncontrolled roll angle time histories are approximately equal. A comparison of pitch attitude for the uncontrolled and controlled trajectories is provided in Figure 5.14. While the nominal and uncontrolled trajectories show a steady decrease in pitch attitude as the rocket flies down range, the controlled trajectory shows oscillatory response due to the firing of pulse jets. Total pitch angle excursions of greater than 2 degrees are experienced toward the end of the trajectory. Similar oscillations are seen in the yaw angle time history shown in

Figure 5.15. The aerodynamic angle of attack of the nominal, uncontrolled, and controlled cases are shown in Figure 5.16. While the angle of attack for the nominal and uncontrolled cases remains relatively small and under 2 deg, the action of pulse jets induces angles of attack greater than 7 deg near the target.

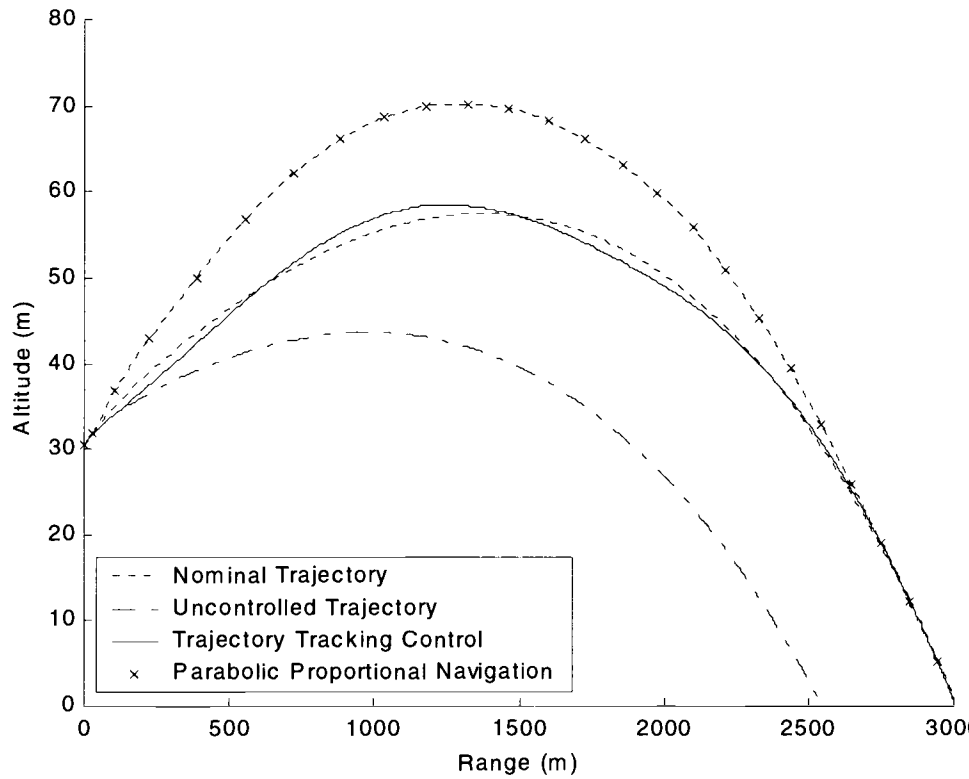

Figure 5.8 Altitude versus Range.

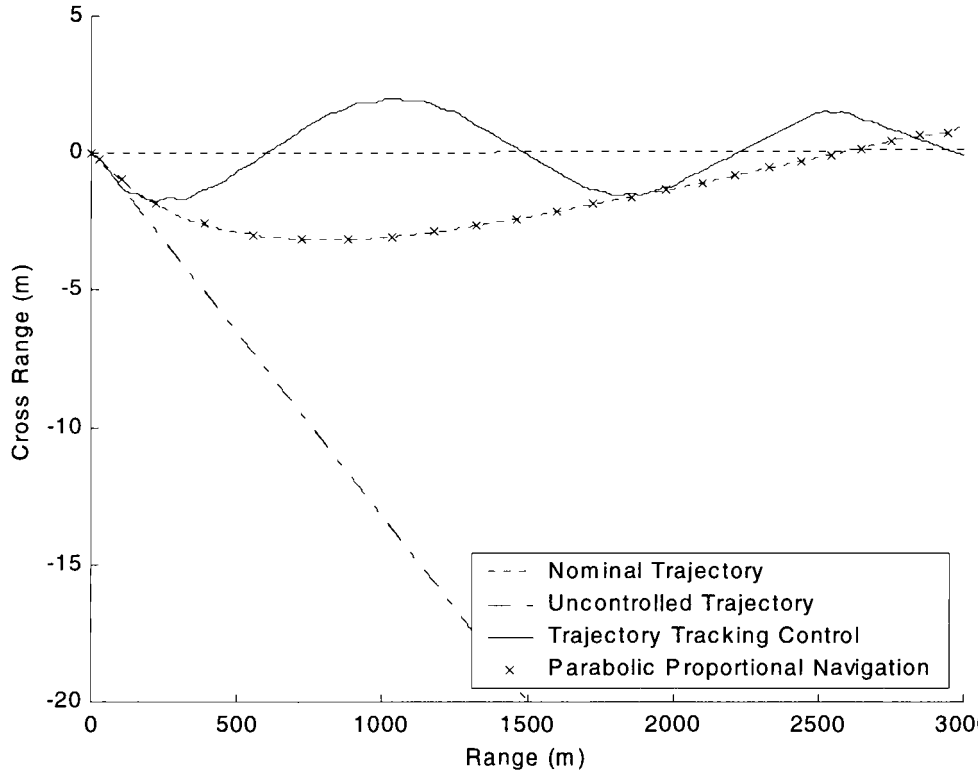

Figure 5.9 Cross Range versus Range.

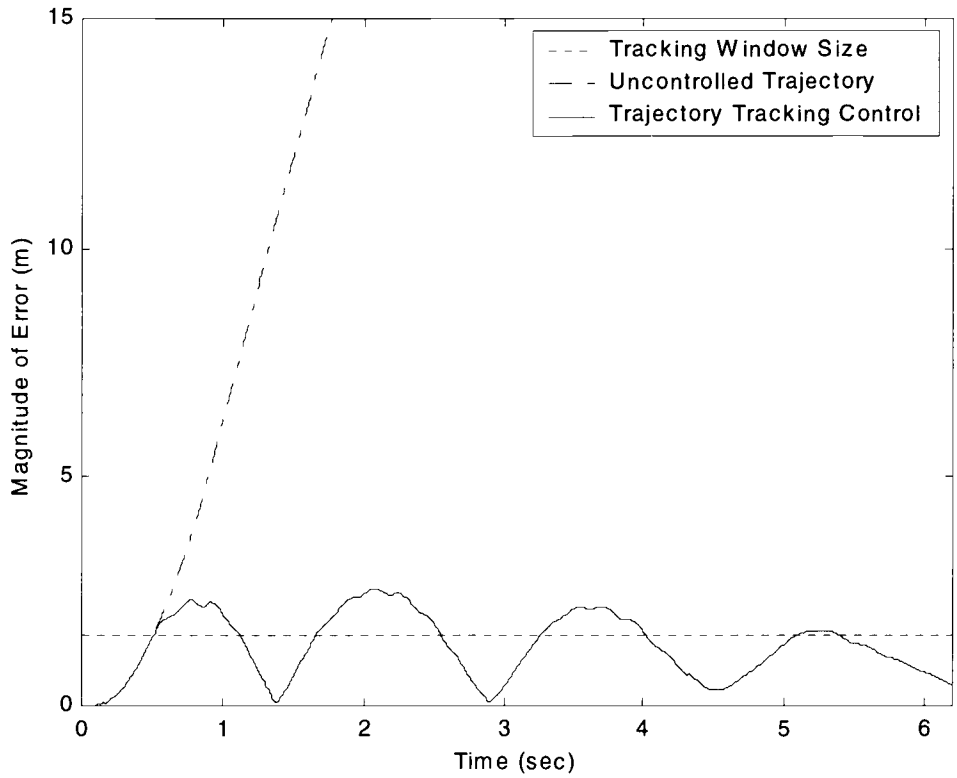

Figure 5.10 Trajectory Tracking Error versus Time of the Trajectory Tracking Controlled Rocket.

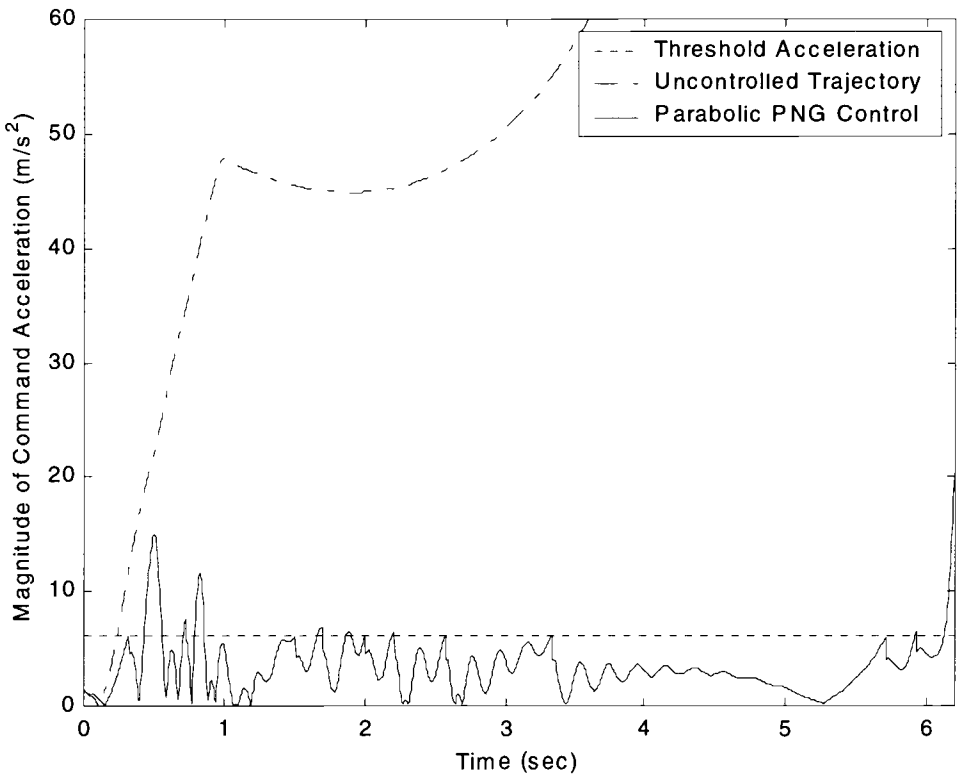

Figure 5.11 Trajectory Tracking Error versus Time of the Proportional Navigation Guidance Controlled Rocket.

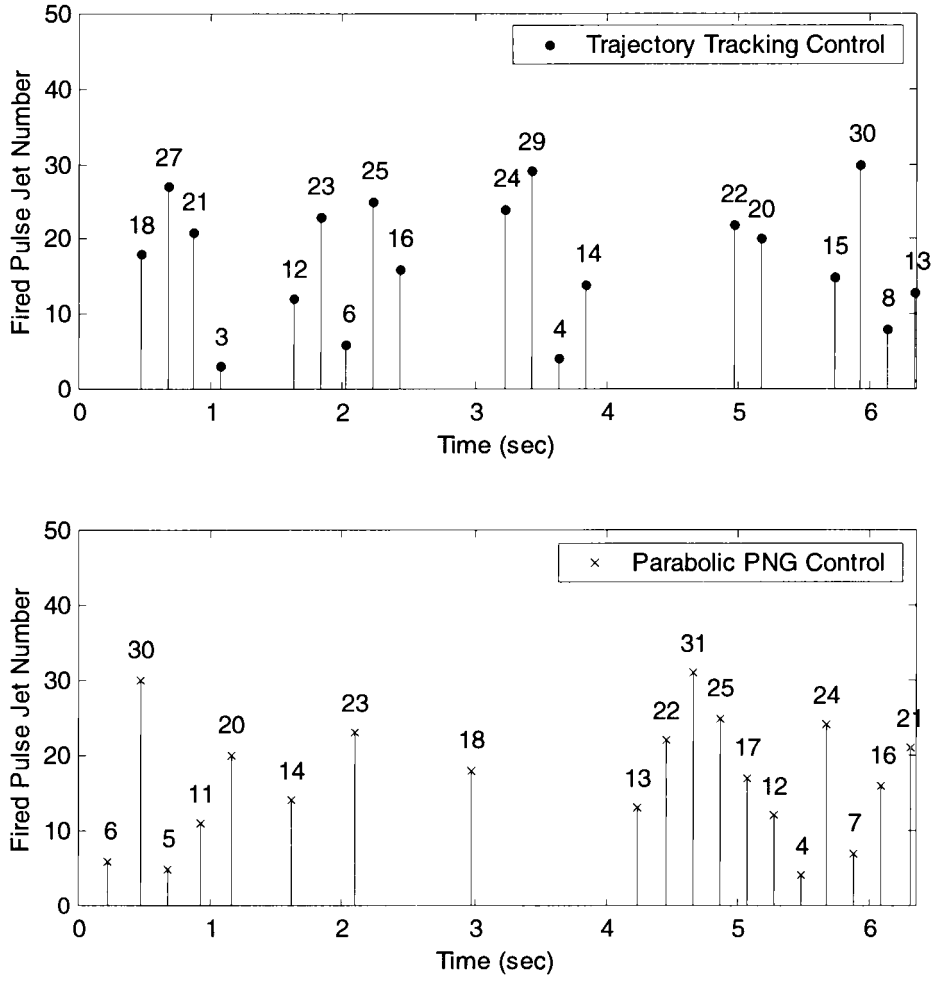

Figure 5.12 Pulse Jet Firing Time.

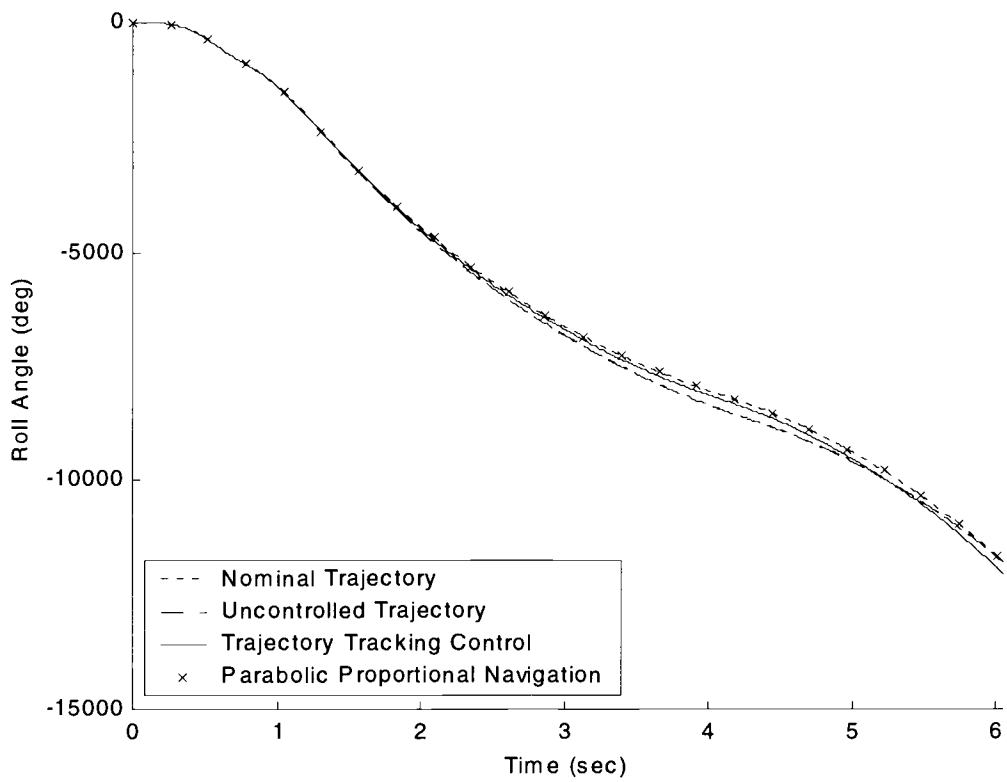

Figure 5.13 Roll Angle versus Time.

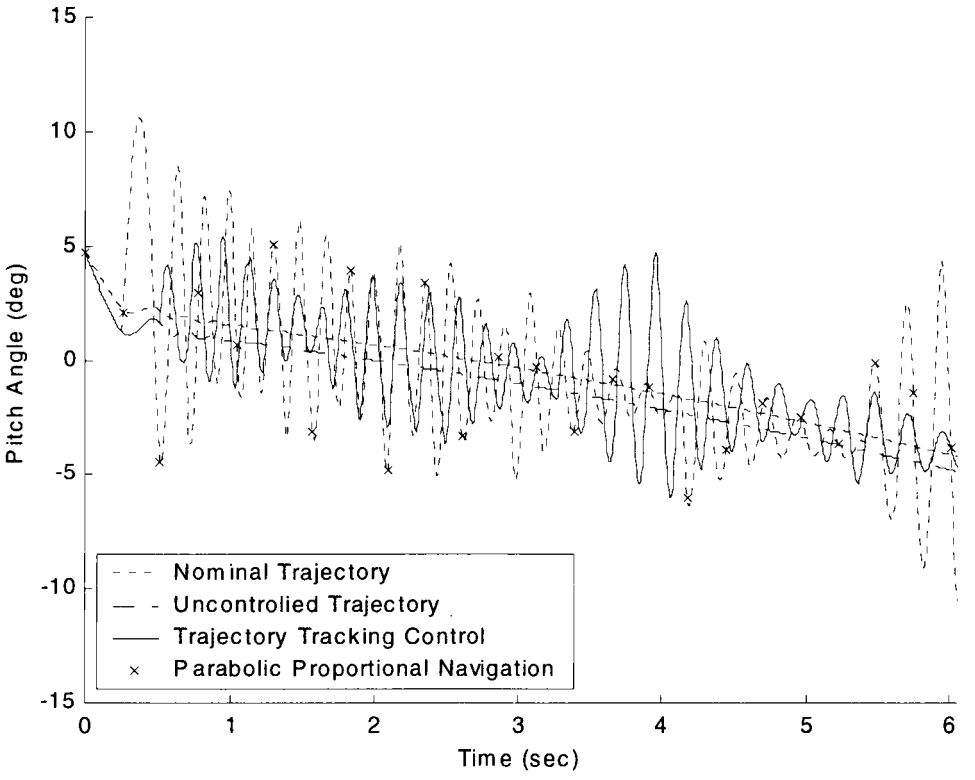

Figure 5.14 Euler Pitch Angle versus Time.

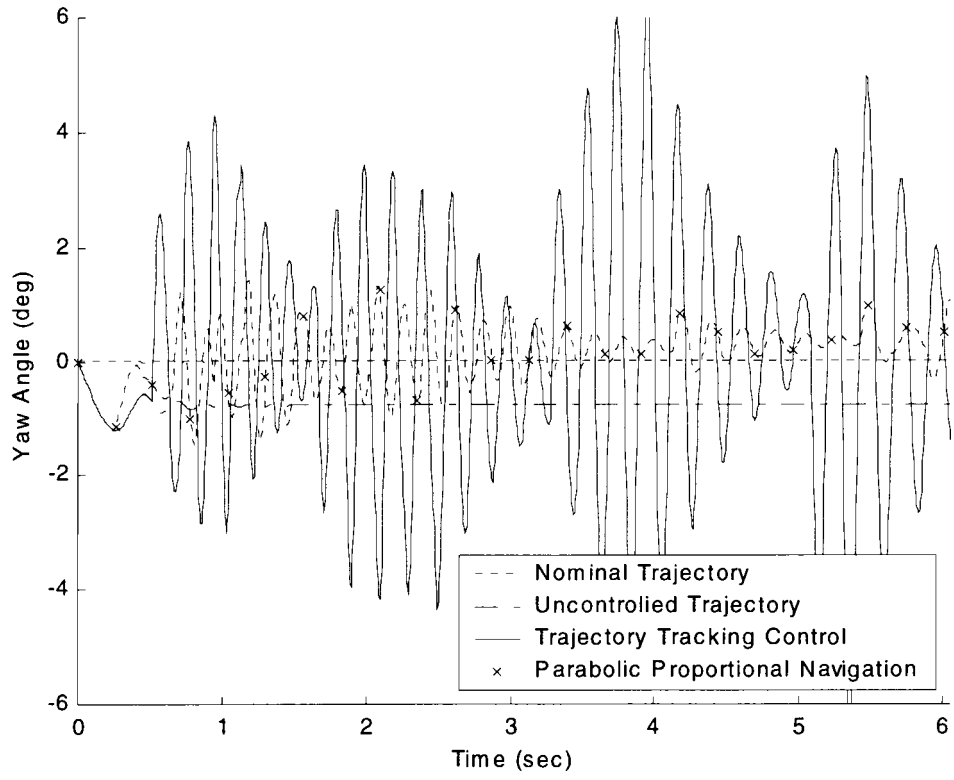

Figure 5.15 Euler Yaw Angle versus Time.

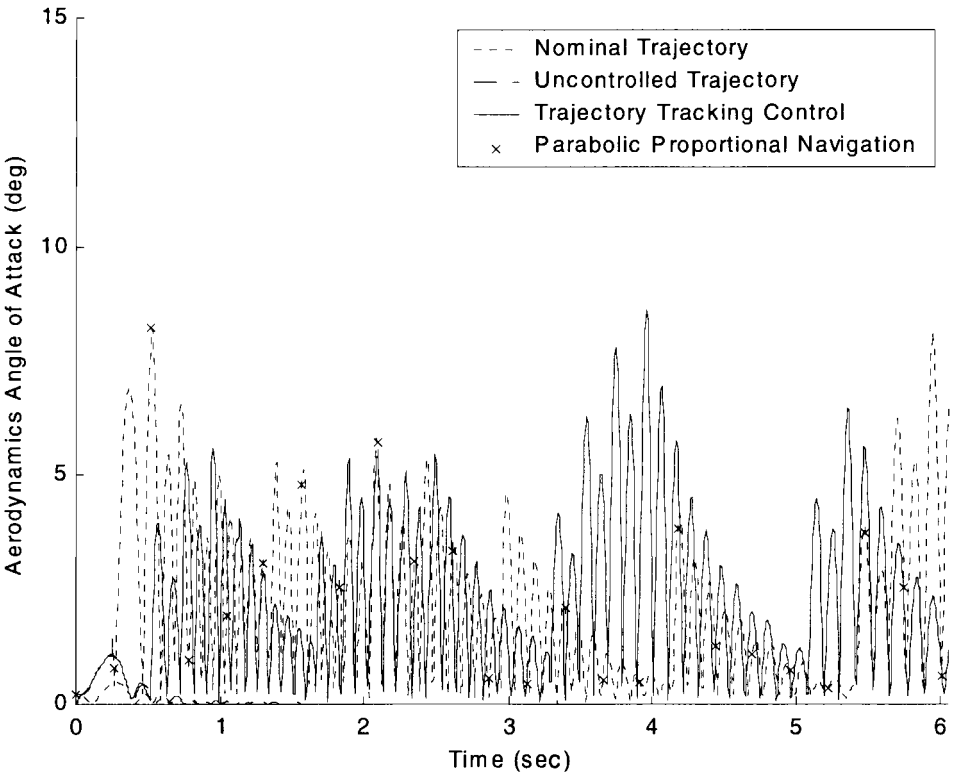

Figure 5.16 Aerodynamic Angle of Attack versus Time.

CHAPTER 6
PARAMETRIC STUDY OF CONTROL MECHANISM AND EFFECT OF SENSOR ERROR

6.1 Parametric Trade Study of Control Mechanism

The initial state of the rocket as it exits the launcher and enters free flight can be viewed as a random process. The random nature of the initial free flight state stems from many effects but perhaps most notably from launcher and rocket manufacturing tolerances combined with resulting launcher and rocket vibration. Random perturbations in initial free flight conditions creates target dispersion. Furthermore, for direct fire rockets, perturbations in initial off axis angular rates have been found to significantly contribution to the impact point error budget (Carter, Chase, and Whiteside, 1994; Bellamy, Chase, and Whiteside, 1995).

Consider a rocket that exists the launcher with the following initial conditions, x=0.0 m, y=0.0 m, z=-30.5 m, ϕ=0.0 deg, θ=4.14 deg, ψ=0.0 deg, u=43.7 m/s, v=0.0 m/s, w=0.11 m/s, p=51.5 rad/s, q=-0.18 rad/s, and r=0.0 rad/s. This rocket creates a trajectory directed to a target at 3000 m downrange, 0 m altitude and 0 m cross range. However perturbations on the initial pitch and yaw rates results in scatter of impact points about the target. Figure 6.1 illustrates impact points at a target range of 3000 m for the uncontrolled and controlled direct

fire rocket configurations with a sample size of 200 dispersions where the initial pitch rate and yaw rate are independent gaussian random variables. The mean value for pitch and yaw rate is –0.18 rad/sec and 0 rad/sec, respectively. The standard deviation for both pitch and yaw rate is 0.3 rad/sec. The dispersion radius is defined as the radius of a circle that emanates from the mean impact point and contains 67% of the impact points. The mean miss distance is the magnitude of the distance from the mean impact point to the target. The large circle in Figure 6.1 is the dispersion radius for the uncontrolled case which is equal to 149.9 m while the dispersion radius for the trajectory tracking controlled rocket configured with 32 lateral pulse jets, 5 N-s impulse each, and 1.5 m tracking window size, is 1.4 m and is not noticeable on the figure.

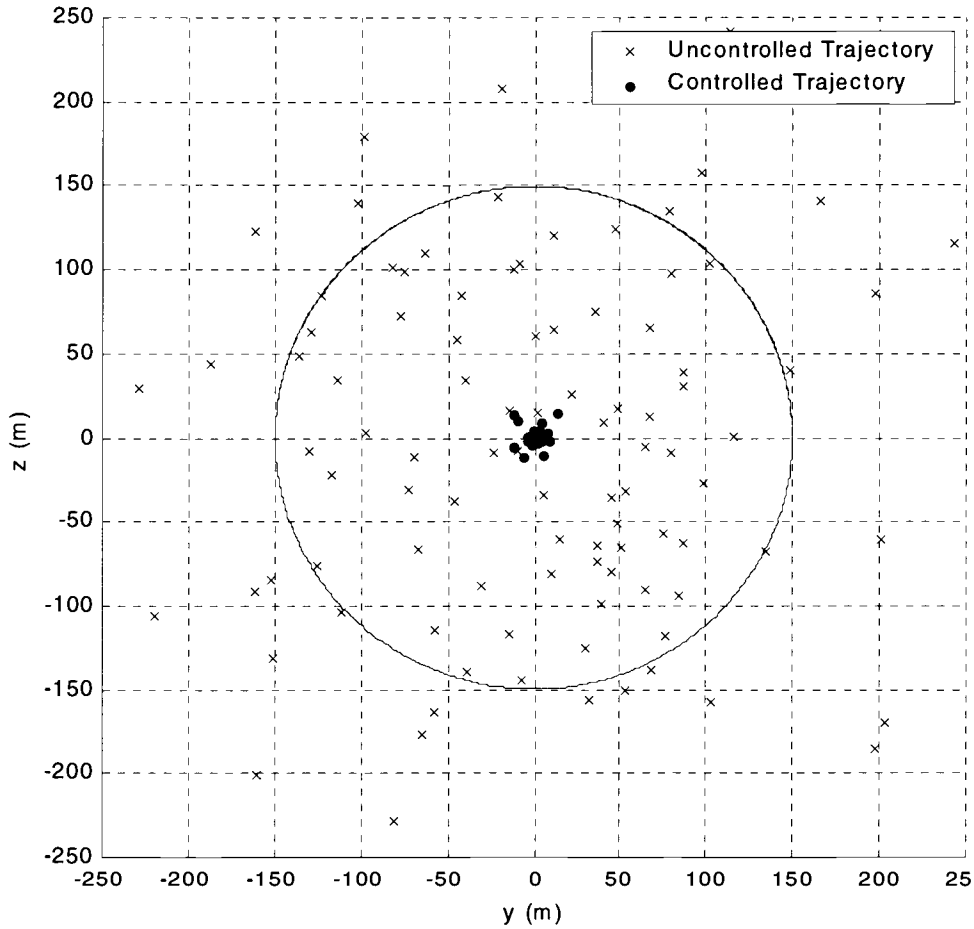

Figure 6.1 Impact Point Dispersion (Perturbed Initial Pitch and Yaw Rate).

The parametric study goal is to understand the effect of three control parameters; magnitude of the pulse jet impulse, the number of pulse jets, and the tracking window size, to the dispersion radius of the controlled rocket. Figures 6.2 through 6.4 show the relationship between dispersion radius, mean miss distance, number of pulse jets on the ring, and individual pulse jet impulse for three different trajectory tracking window sizes of 0.3 m, 1.5 m, and 3.0 m. As the number of individual pulse jets is increased, the total impulse contained in the pulse jet ring is increased. In the mean miss distance plots, the trajectory tracking window size is shown as a constant dashed line. When the impulse for the individual lateral pulse jets is small, dispersion radius is steadily reduced as the number of pulse jets or the jet impulse is increased. By viewing Figures 6.2 through 6.4, it is seen that the 1 N-s impulse is underpowered for the rocket. When the individual lateral pulse jet impulse is relatively large, adding more pulse jets can actually increase the mean miss distance. For a small tracking window size and large impulse, the dispersion radius oscillates as the total number of jets is increased. In this case, the lateral pulse jet impulse is so large compared to the trajectory tracking error that firing a particular pulse jet tends to over correct the tracking error leading to larger target dispersion. In these cases, the pulse jets are overpowered for the tracking error they seek to maintain. By contrasting Figures 6.2, 6.3, and 6.4 for a given pulse jet configuration, dispersion is generally reduced as the tracking window size is reduced. The exception to this rule is high impulse jets which do not show a definite trend due to the overshoot problem mentioned above.

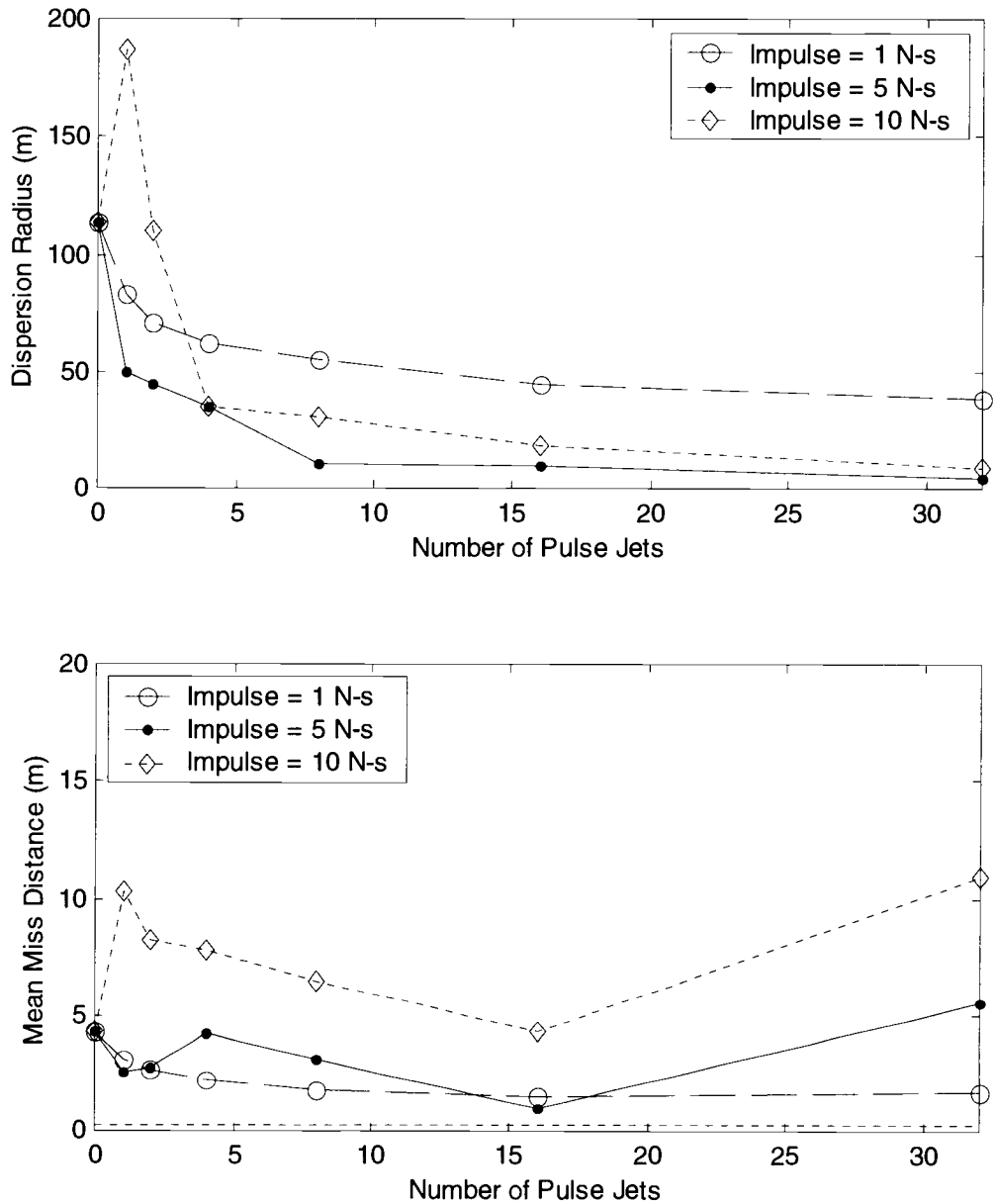

Figure 6.2 Dispersion Radius and Mean of Miss Distance versus Number of Pulse Jets and Pulse Jets Impulse for Trajectory Tracking Window Size of 0.3 m.

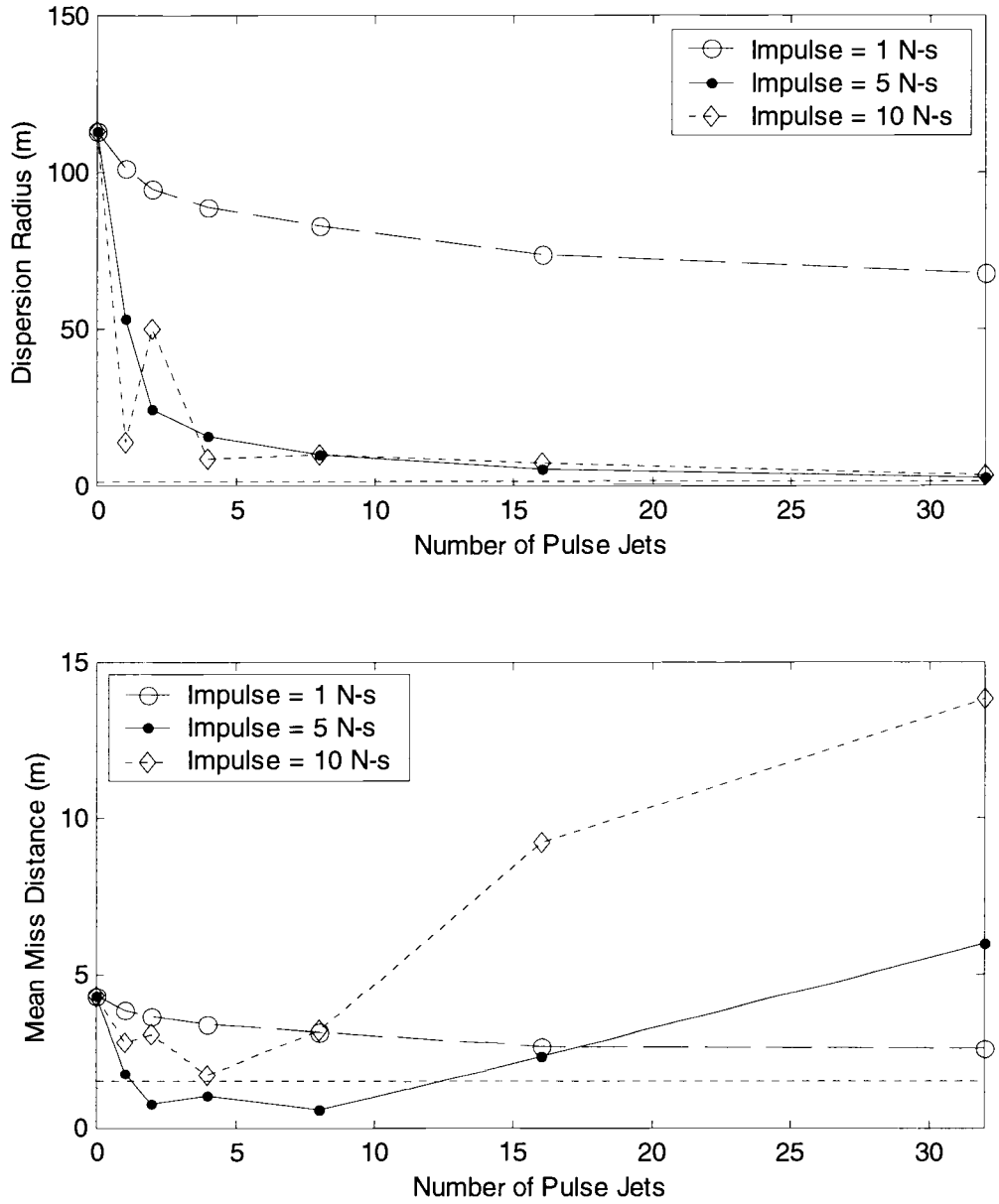

Figure 6.3 Dispersion Radius and Mean of Miss Distance versus Number of Pulse Jets and Pulse Jets Impulse for Trajectory Tracking Window Size of 1.5 m.

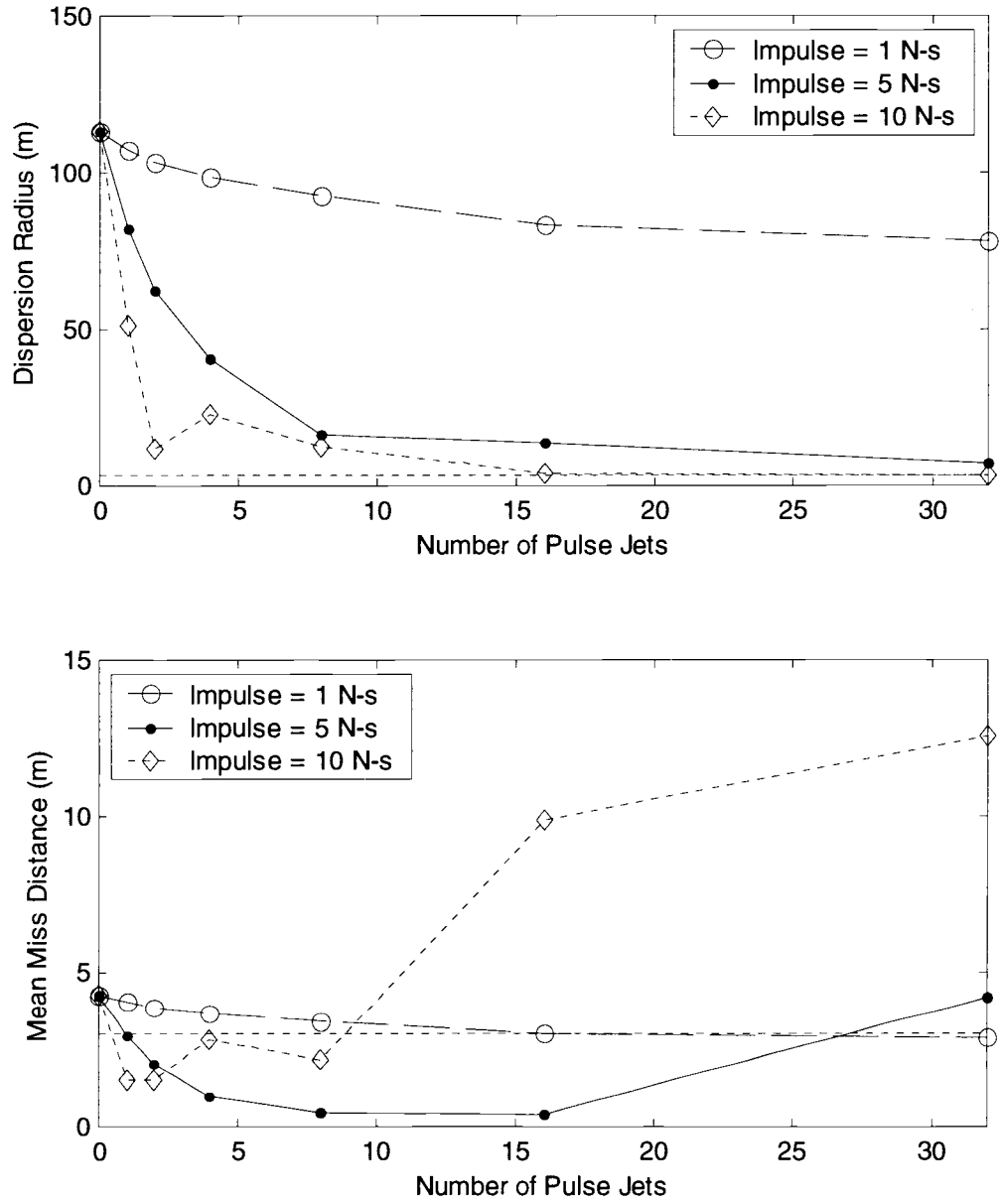

Figure 6.4 Dispersion Radius and Mean of Miss Distance versus Number of Pulse Jets and Pulse Jets Impulse for Trajectory Tracking Window Size of 3.0 m.

Figure 6.5 shows the relationship between dispersion radius, mean miss distance, number of pulse jets on the ring, and the total ring impulse for a trajectory tracking window size of 1.5 m. Each line on the figure represents lines of constant total ring impulse. For these traces, as the number of lateral pulse jets on the ring is increased, the impulse for an individual lateral pulse jet decreases proportionally so the total ring impulse remains constant. For relatively low total ring impulse, a single lateral pulse jet yields the lowest dispersion radius. The reason for this trend is that the effectiveness of a pulse jet on the trajectory decreases sharply as the projectile flies down range. Hence, a comparatively large and early trajectory correction provides more of an impact point modification than two pulses, each of half impulse strength, where one of the pulses occurs farther down range. As the total impulse on the ring is increased, the minimum dispersion radius is decreased. For relatively large total ring impulse, an optimum number of individual lateral pulse jets exists for a given trajectory tracking window size. In the example shown in Figure 6.5, a total ring impulse of 16 N-s split into 4 individual lateral pulse jets provides the optimum dispersion reduction. Figure 6.6 plots the dispersion radius versus the number of pulse jets for three different trajectory tracking window sizes. The total ring impulse for all data on the chart is 80 N-s. A single impulse increases the dispersion radius for trajectory tracking window sizes of 1.5 m and 3.0 m. This figure underlines the importance of properly selecting the number of pulse jets and the pulse jet impulse for a particular accuracy design requirement.

Figures 6.7 and 6.8 plot dispersion radius as a function of the atmospheric wind angle for the uncontrolled and controlled rocket configurations, respectively. An atmospheric wind angle of 0 deg corresponds to a direct head wind whereas an angle of 180 deg represents a direct tail wind. The uncontrolled rocket configuration is insensitive to direct head and tail winds as in these cases the rocket range is predominantly effected. On the other hand, side winds induce dispersion over 130 m. The controlled rocket configuration successfully suppresses dispersion to under 6 m for all wind directions.

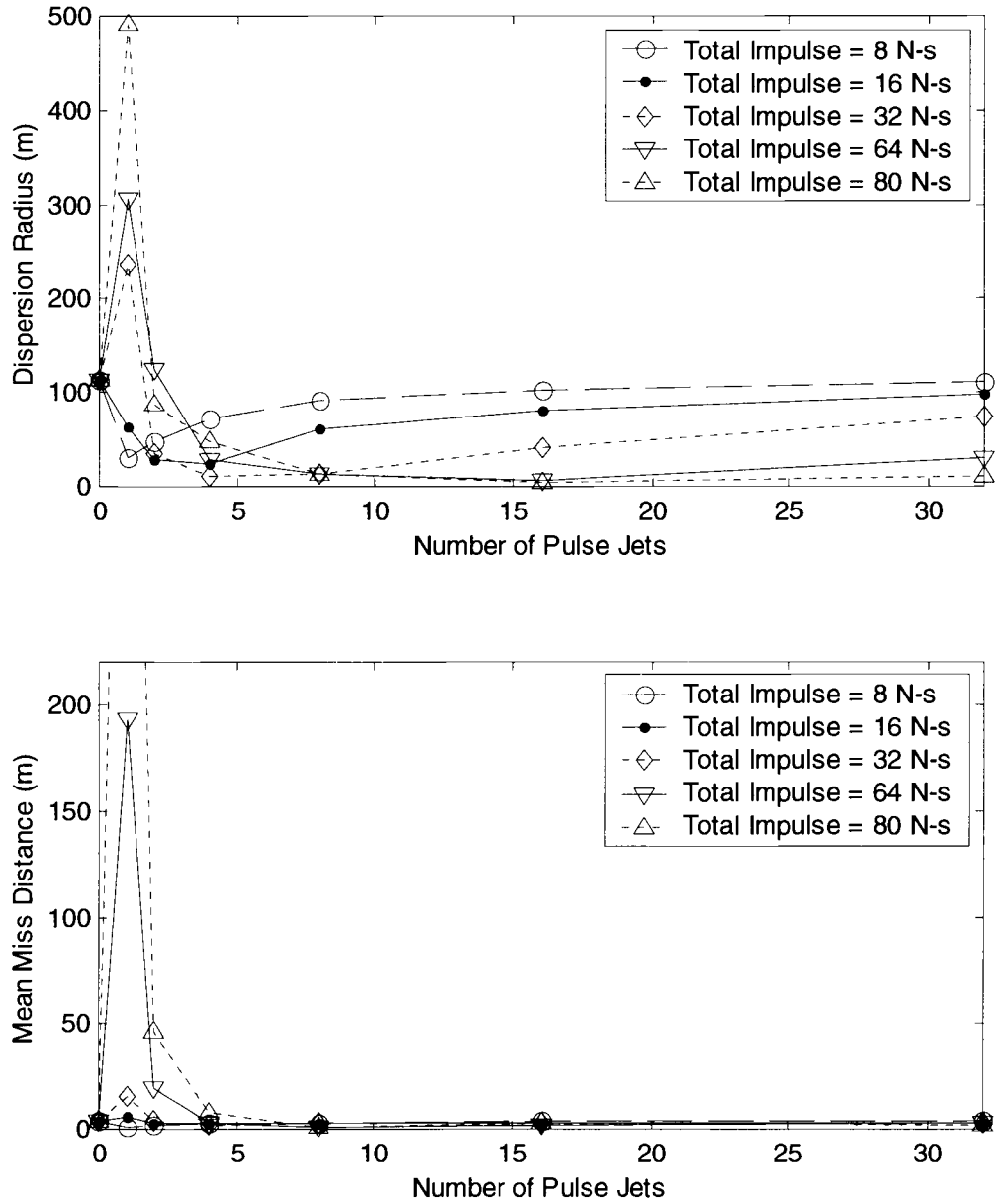

Figure 6.5 Dispersion Radius versus Number of Pulse Jets and Total Ring Impulse (Trajectory Tracking Window Size = 1.5 m).

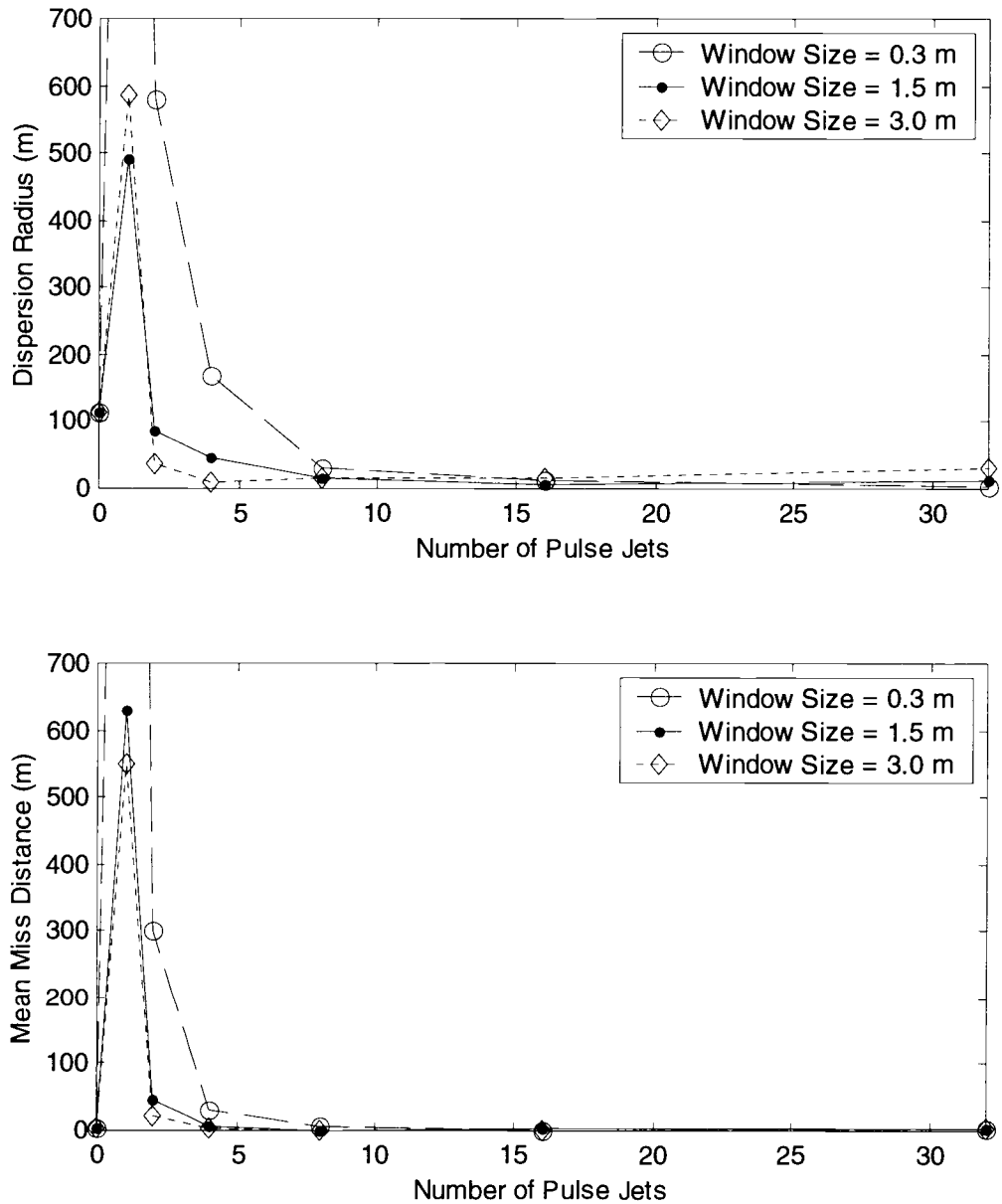

Figure 6.6 Dispersion Radius versus Number of Pulse Jets and Trajectory Tracking Window Size (Total Ring Impulse = 80 N-s)

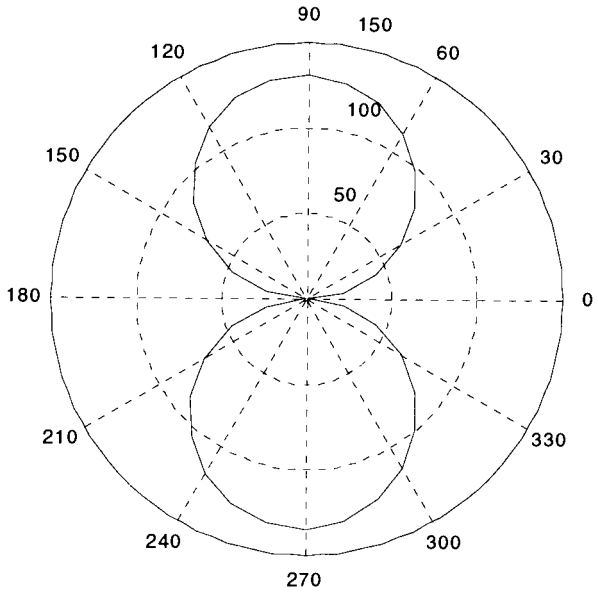

Figure 6.7 Dispersion Radius versus Atmospheric Wind Direction for the Uncontrolled Rocket (Atmospheric Wind Speed = 7.6 m/s, Number of Pulse Jets = 32, Pulse Jet Impulse = 20 N-s, Trajectory Tracking Window Size = 1.5 m)

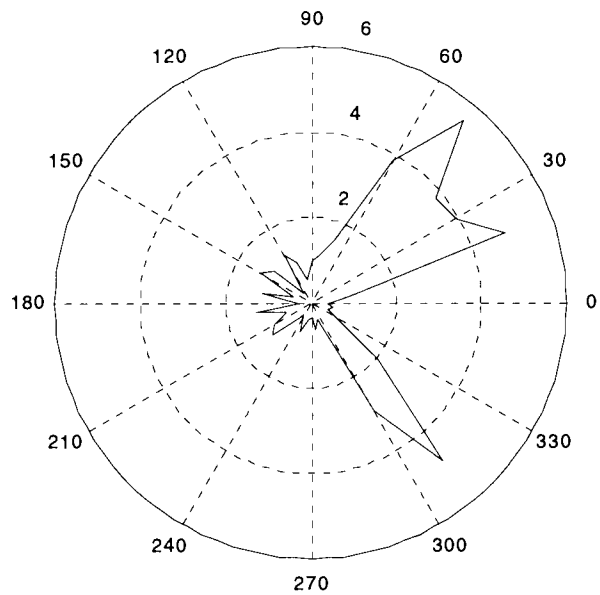

Figure 6.8 Dispersion Radius versus Atmospheric Wind Direction for the Controlled Rocket (Atmospheric Wind Speed = 7.6 m/s, Number of Pulse Jets = 32, Pulse Jet Impulse = 20 N-s, Trajectory Tracking Window Size = 1.5 m)

6.2 Comparison of Control Algorithms

Figure 6.9 presented the relationship between the dispersion radius, the mean miss distance and the number of pulse jets of controlled rockets using the trajectory tracking method and the parabolic PNG scheme. Both systems are equipped with the identical pulse jet configuration of 5 N-s impulse. The tracking window size of 1.5 m is chosen for the trajectory tracking system while the acceleration threshold of 6.0 m/sec^2 are optimized for the parabolic PNG system. For both control schemes the dispersion radius of the controlled rockets reduces as the number of pulse jets increases. The parabolic PNG induces slightly better dispersion radius reduction than the trajectory tracking control system in the region of high number of pulse jets. However, the trajectory tracking system reduces more dispersion radius when small number of pulse jets is used. In the lower plot in Figure 6.9 the mean miss distance of the controlled rockets increases in the region of low number of rockets. This increasing of error dues to the fact that the PNG algorithm relies on the assumption of a parabolic shape trajectory which does not accurately predict a path of a rocket with active thrust motor. Comparatively, the trajectory tracking system has advantage in the relatively smaller mean miss distance in all cases.

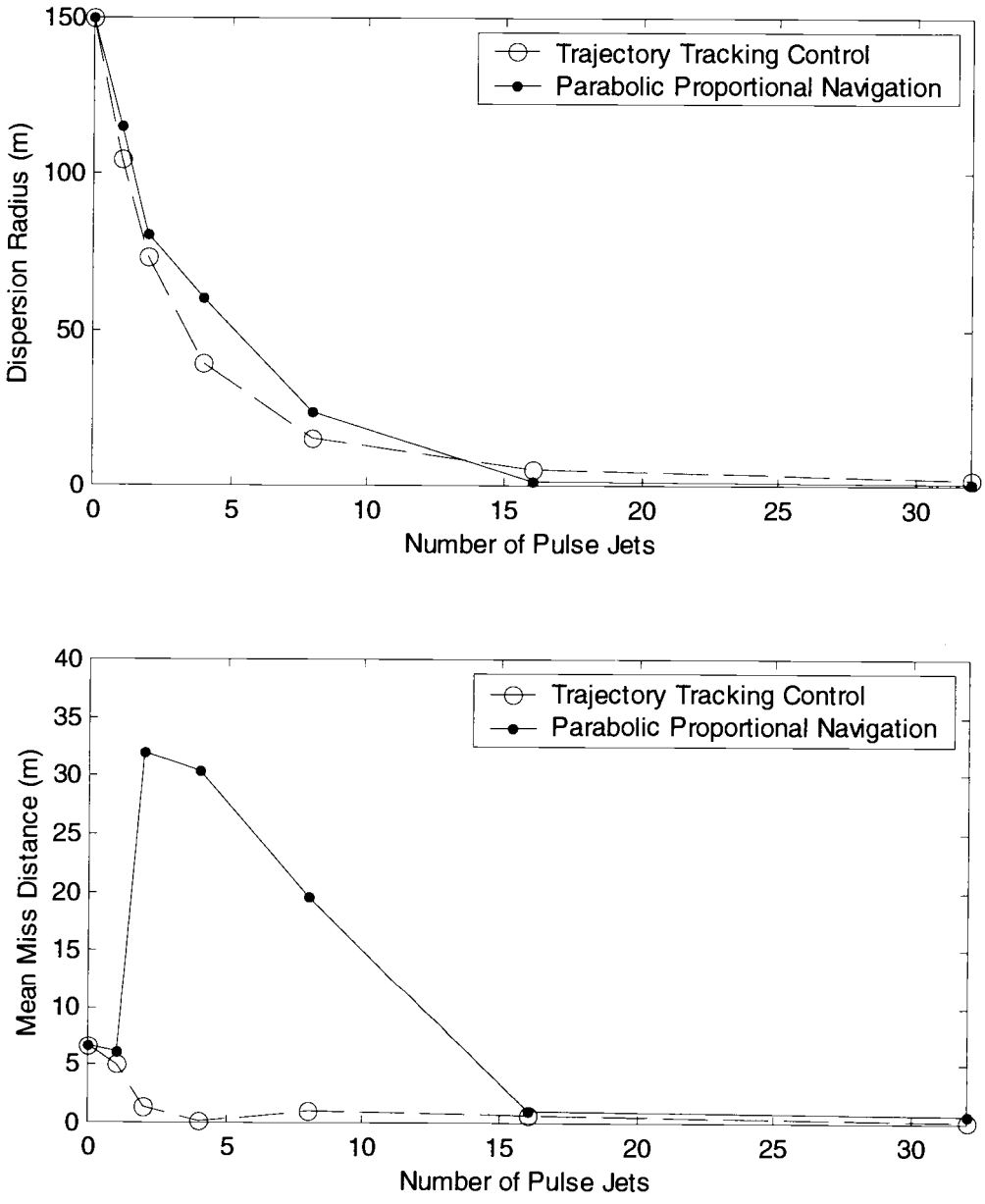

Figure 6.9 Comparison of Control Navigation System

6.3 Effect of Sensor Errors in Control Performance

6.3.1 Sensor Errors in Conventional IMU

A conventional IMU uses three accelerometers and three gyroscopes to sense the states of the rocket for the flight control system. Noises, bias, and cross axis sensitivity from these sensors produce errors in the measurement that reduce the accuracy of the control unit. In the parametric study to follow, the reference control mechanisms are configured with 5 Ns jet impulses and a 1.5 m tracking window size. Figures 6.9 to 6.15 show the relationship between dispersion radius, mean miss distance, and the number of pulse jets for different levels of noise, bias, and cross axis sensitivity in the accelerometers and the gyroscopes. Each accelerometers has Gaussian noise characteristics with 0 mean and 0.039 m/s^2 standard deviation, a bias of 0.981 m/s^2, and a cross axis sensitivity of 2%. The gyroscopes have Gaussian random noise characteristics with 0 mean and 0.01 rad/s standard deviation, a bias of 0.01 rad/s and a cross axis sensitivity of 2%. The IMU is located at 1.16 m from the projectile base on the $\vec{I}_B$ axis.

The effect of different levels of accelerometer noise on the dispersion radius and the mean miss distance is presented in Figure 6.10. The 100% noise level represents the baseline case described above. The 200% level indicates the actual noise level of the accelerometer is twice the noise of the IMU used in the calibration. The actual sensor bias and the cross axis sensitivity are identical to the calibration setting of the IMU. The noise at all levels induces little effect on the dispersion radius. However, mean miss distance increases with an increasing number of pulse jets when noise is present. Figure 6.11 shows the effect of accelerometer bias on dispersion radius and mean miss distance. The incorrect determination of the accelerometer cross axis sensitivity causes the higher mean miss distance in the results as shown in Figure 6.12.

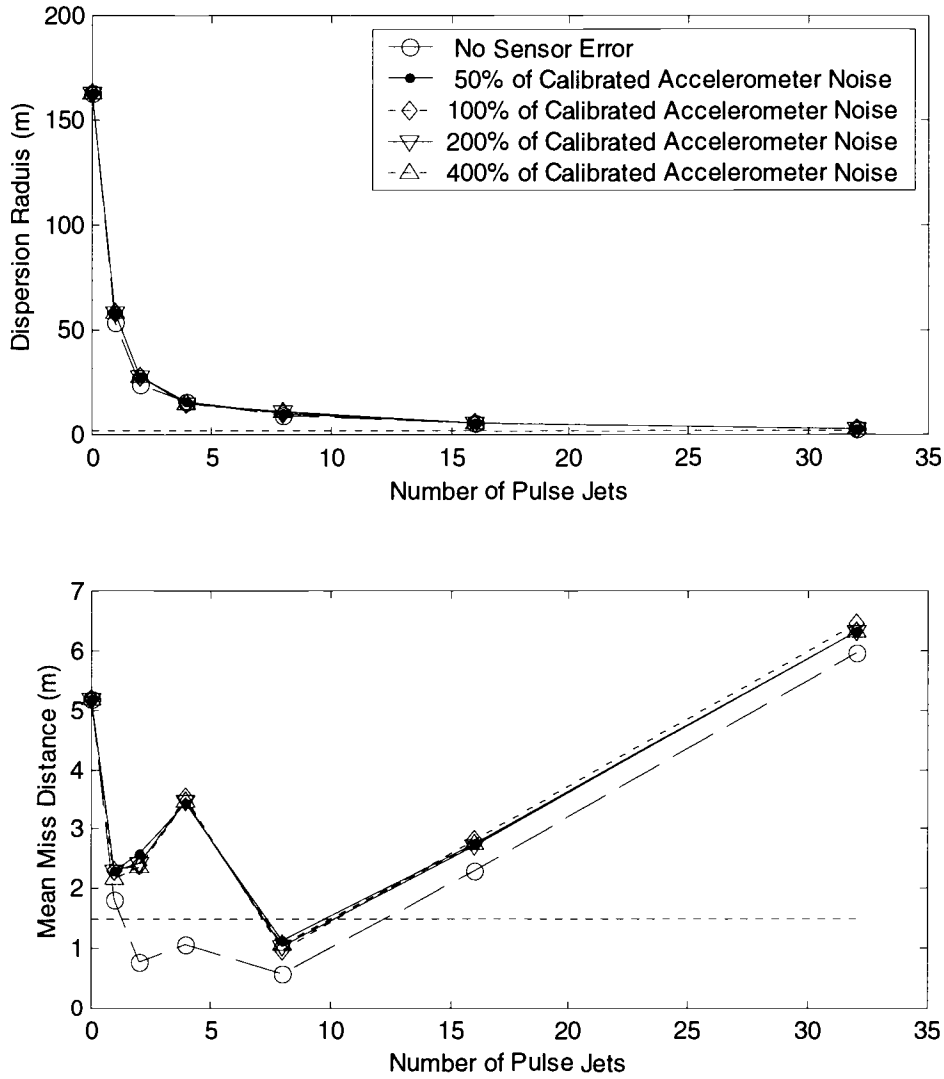

Figure 6.10 Effect of Accelerometer Noise on Conventional IMU.

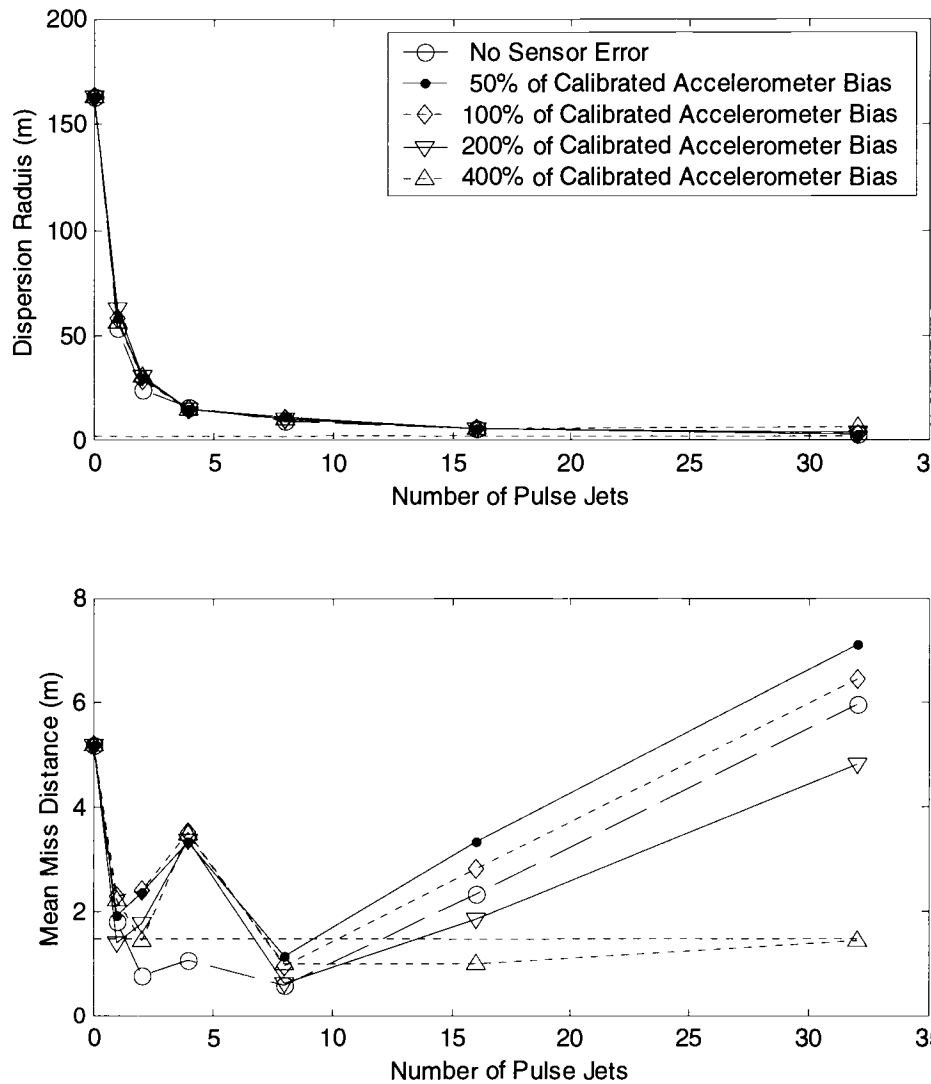

Figure 6.11 Effect of Accelerometer Bias on Conventional IMU.

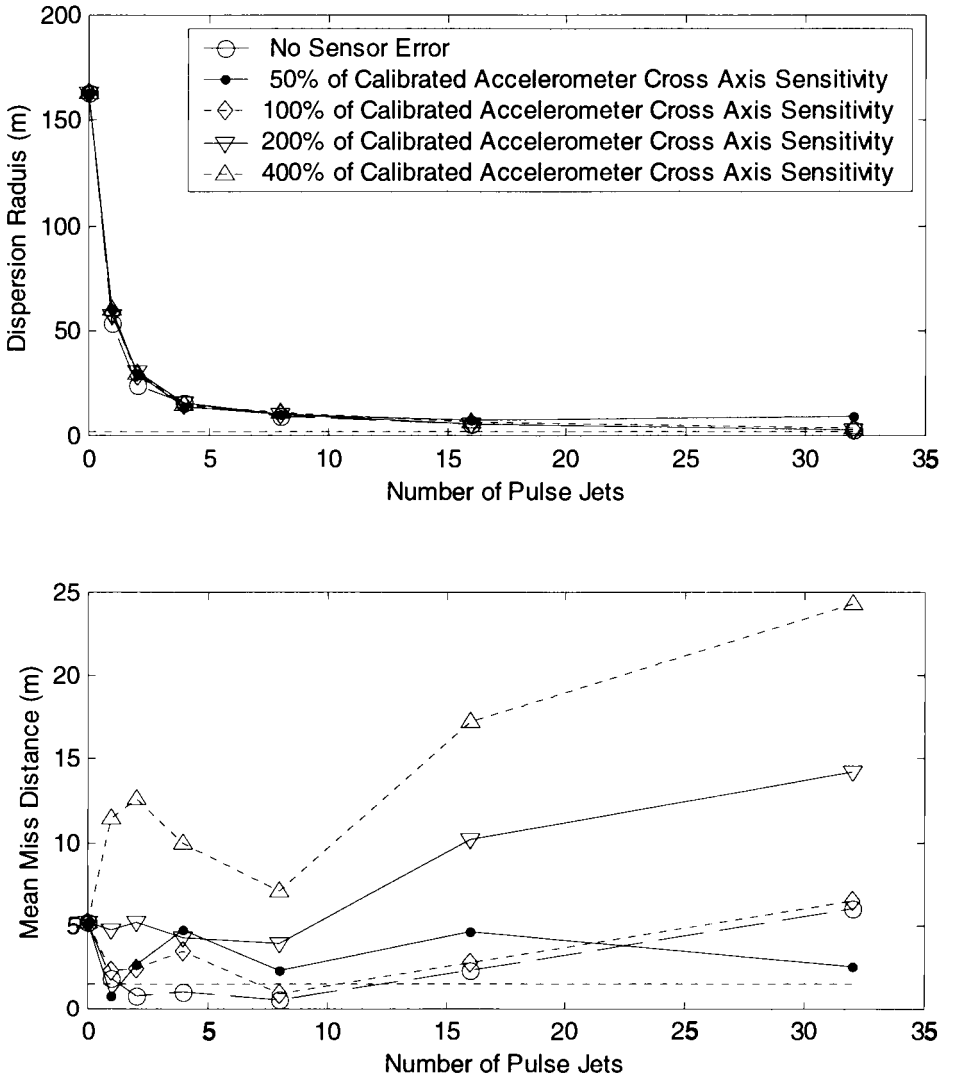

Figure 6.12 Effect of Accelerometer Cross Axis Sensitivity on Conventional IMU.

The trade study results of gyroscope noises, bias, and the cross axis sensitivity are shown in Figure 6.13, 6.14, and 6.15, respectively. The effect of different levels of gyroscope noise on the dispersion radius and the mean miss distance is presented in Figure 6.13. The 100% noise level represents the baseline case described above. The 200% level indicates the actual noise level of the gyroscope is twice the noise of the IMU used in the calibration. The actual sensor bias and the cross axis sensitivity are identical to the calibration setting of the IMU. In Figures 6.13 and 6.14 the dispersion radius reduces with increasing number of pulse jets in the same level at different levels of noise and bias. The trends of the mean miss distance are also closed together in all levels on noise and bias. However the dispersion radius and mean miss distance increase as the level of the cross axis sensitivity increases as shown in Figure 6.15. When comparing the effect of errors in accelerometers to the effect of errors in gyroscope to the control performance. The miss calibration of gyroscopes shows stronger error than to the accelerometers. The dispersion radius and the mean miss distance tremendously increase with incorrect setting of the cross axis sensitivity in the IMU. It can be concluded that performance of the control system is more sensitive to the measurement of angular rates than to the measurement of linear acceleration.

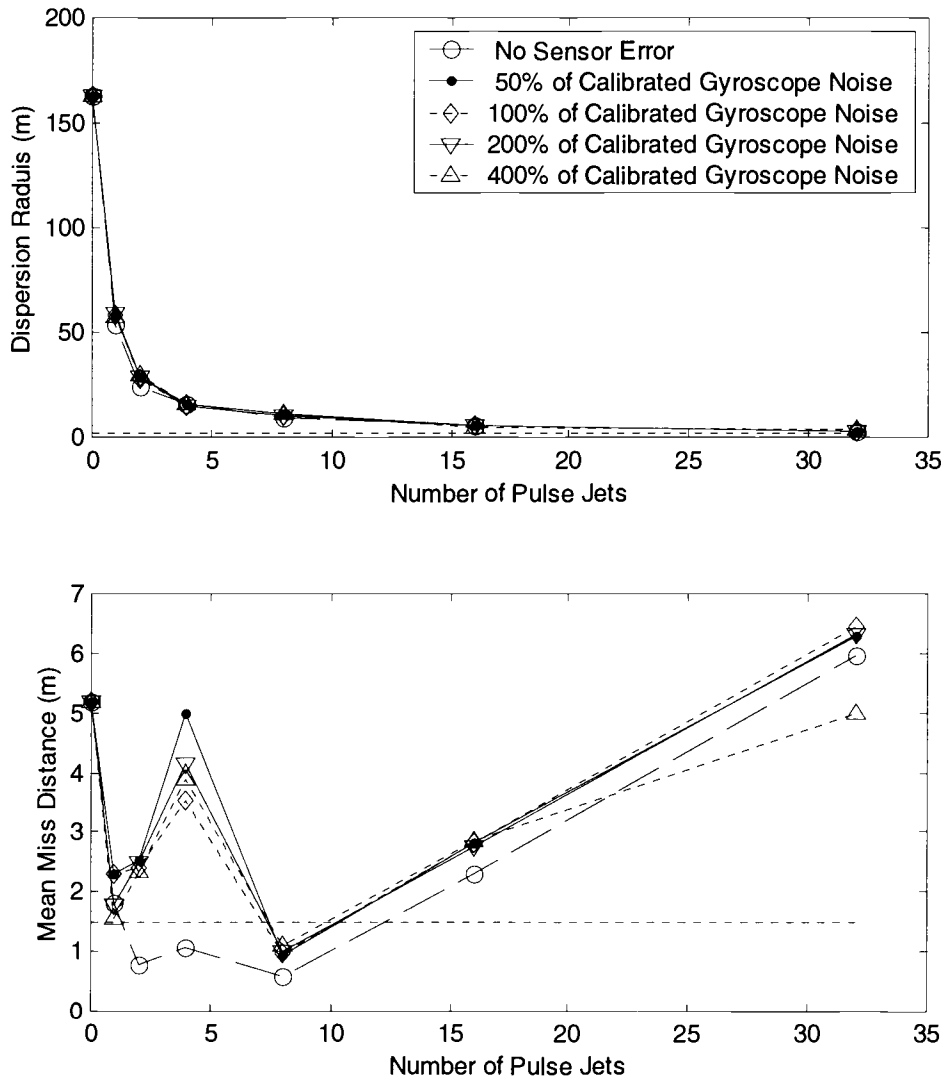

Figure 6.13 Effect of Gyroscope Noise on Conventional IMU.

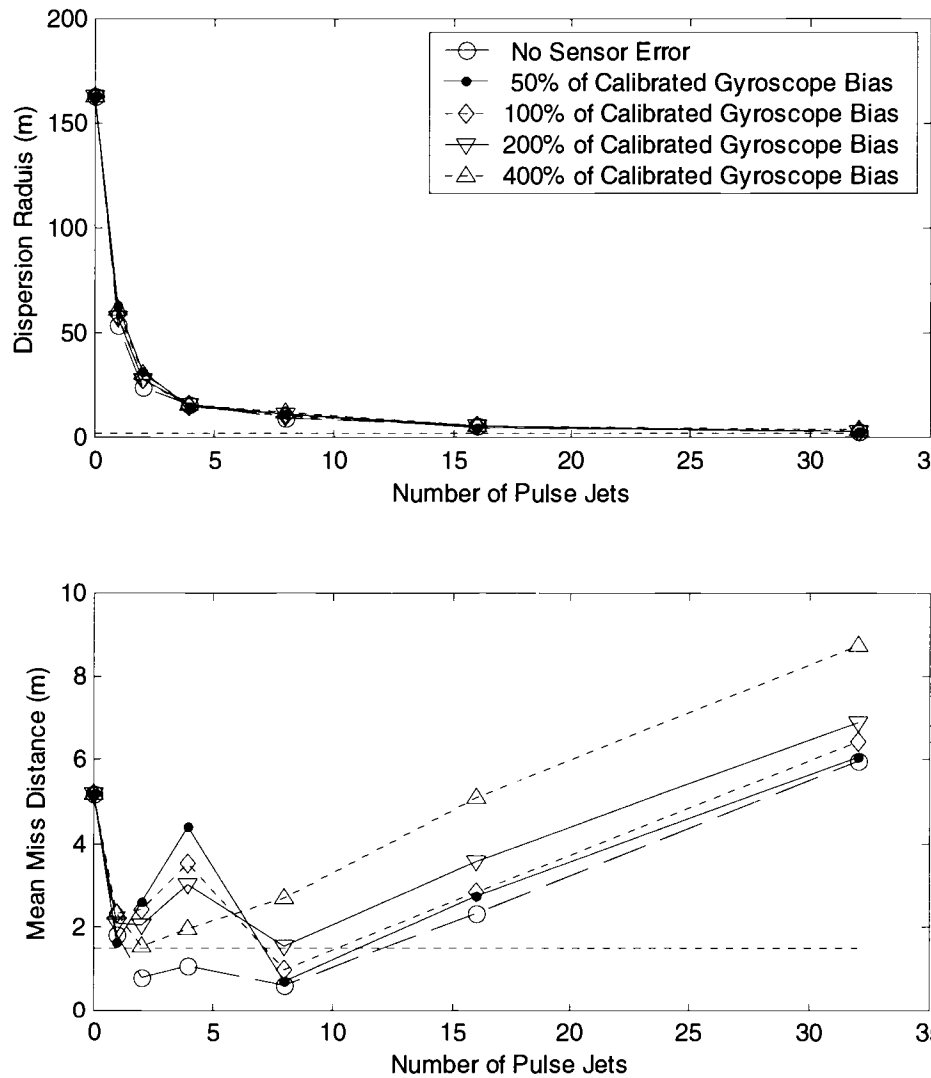

Figure 6.14 Effect of Gyroscope Bias on Conventional IMU.

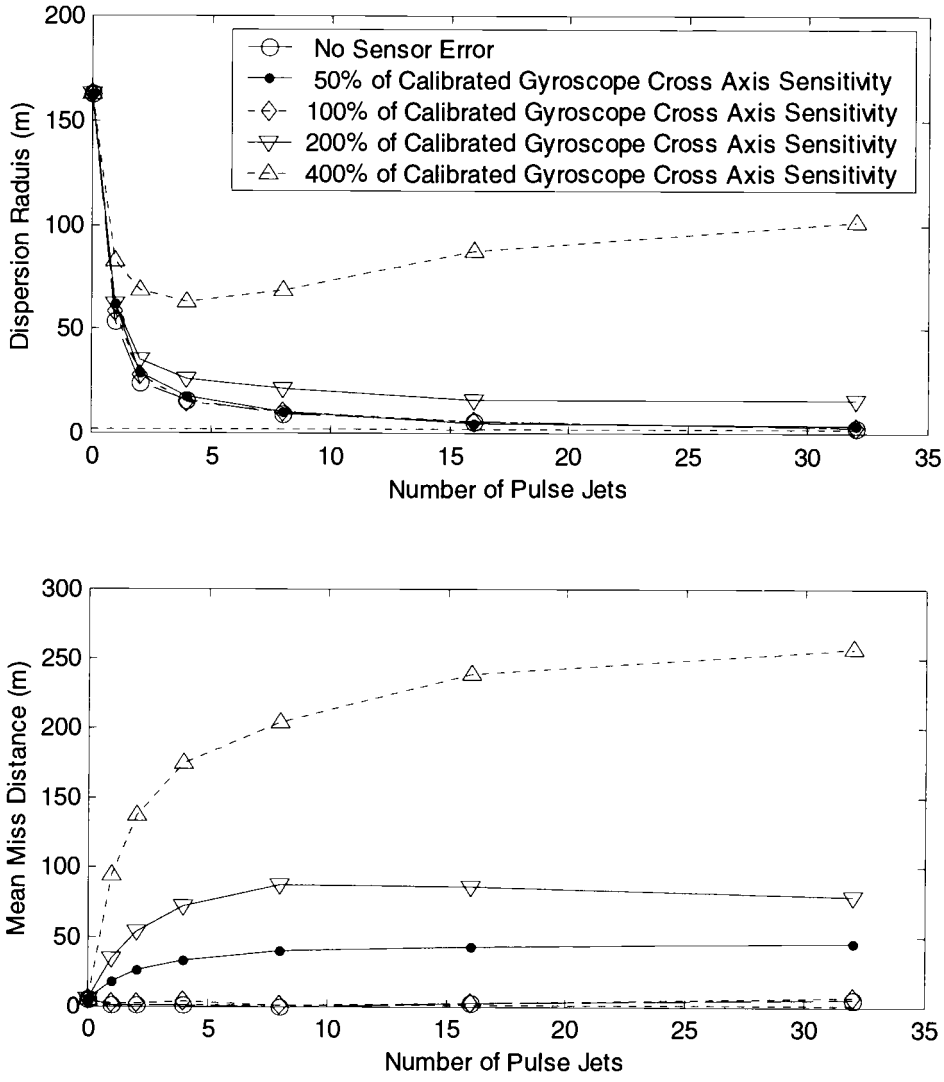

Figure 6.15 Effect of Gyroscope Cross Axis Sensitivity on Conventional IMU.

6.3.2 Sensor Errors in the Unconventional IMU Using Three Triaxial Accelerometer

The algorithm for determining angular rates using three non-coplanar triaxial accelerometers is governed to function as gyroscopes in the IMU. These accelerometers are located in L configuration as described in Section 4.3. In the study, the algebraic sign determination does not apply to the algorithm, thus the signs of p, q, r are assumed to be known. The manufacturer values of the accelerometer noise, bias, and cross axis sensitivity are identical to the accelerometers used in the parametric study of a conventional IMU. Figure 6.16 represents the relationship between the dispersion radius, the mean miss distance and the number of pulse jets at different levels of noise. The effects of accelerometer bias and cross axis sensitivity are shown in Figure 6.17 and 6.18, respectively. By comparing the dispersion radius decreasing trends among Figures 6.16, 6.17, and 6.18, the dispersion radius decreases with increasing number of pulse jets at all levels of noise and bias but at increasing level. This implies that dispersion radius is less sensitive to the accelerometer noise. However, the mean miss distance increases with increasing number of pulse jets when noisy accelerometers are used. The bias and cross axis sensitivity errors provide increasing in the dispersion radius and the mean miss distance. These error trends are expected, since the accelerometers function as gyroscopes in this estimation method.

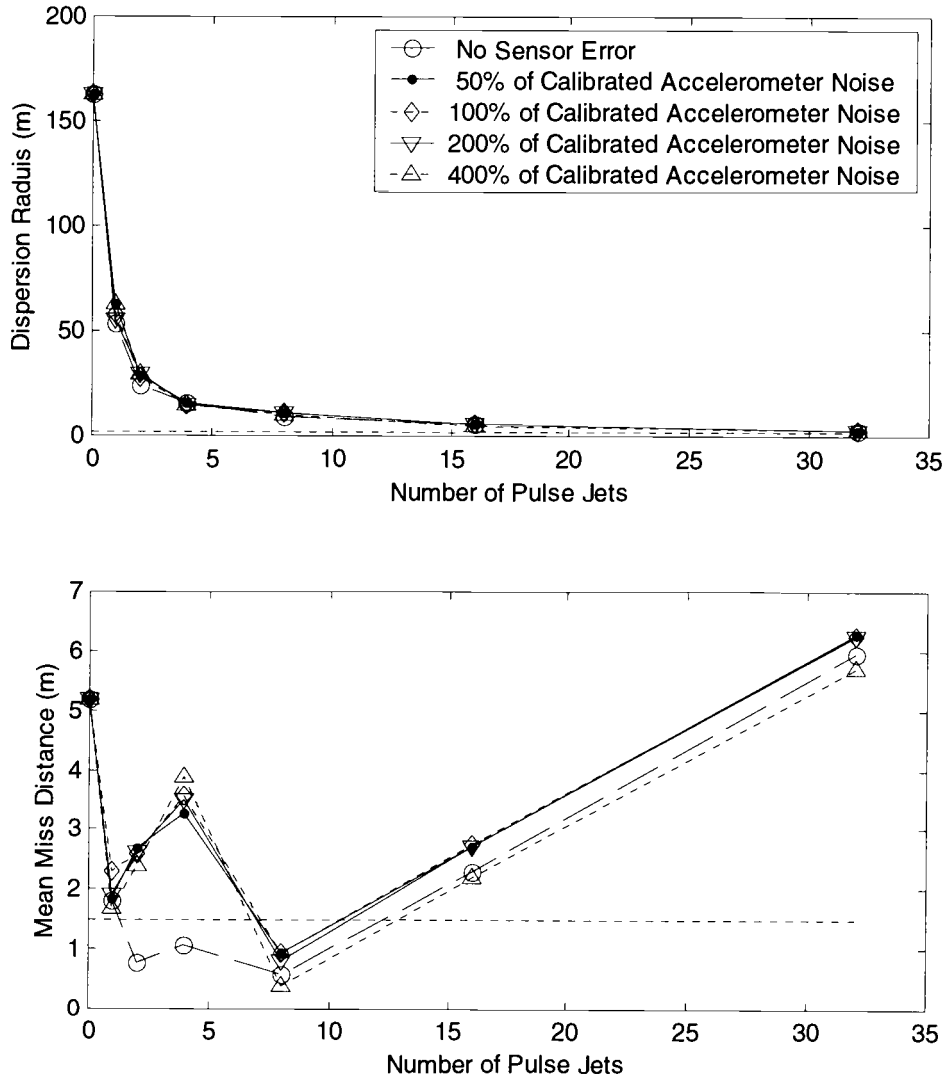

Figure 6.16 Effect of Accelerometer Noise on Three Triaxial Accelerometer Method.

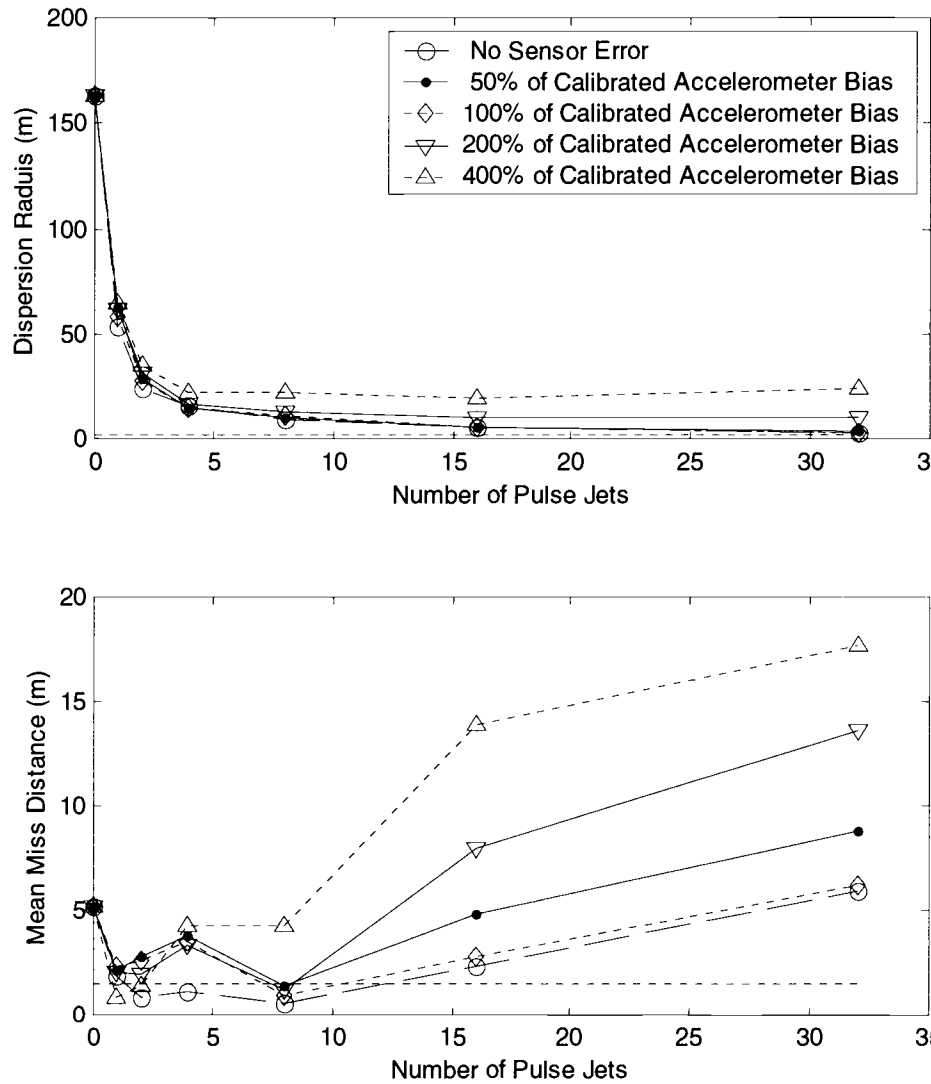

Figure 6.17 Effect of Accelerometer Bias on Three Triaxial Accelerometer Method.

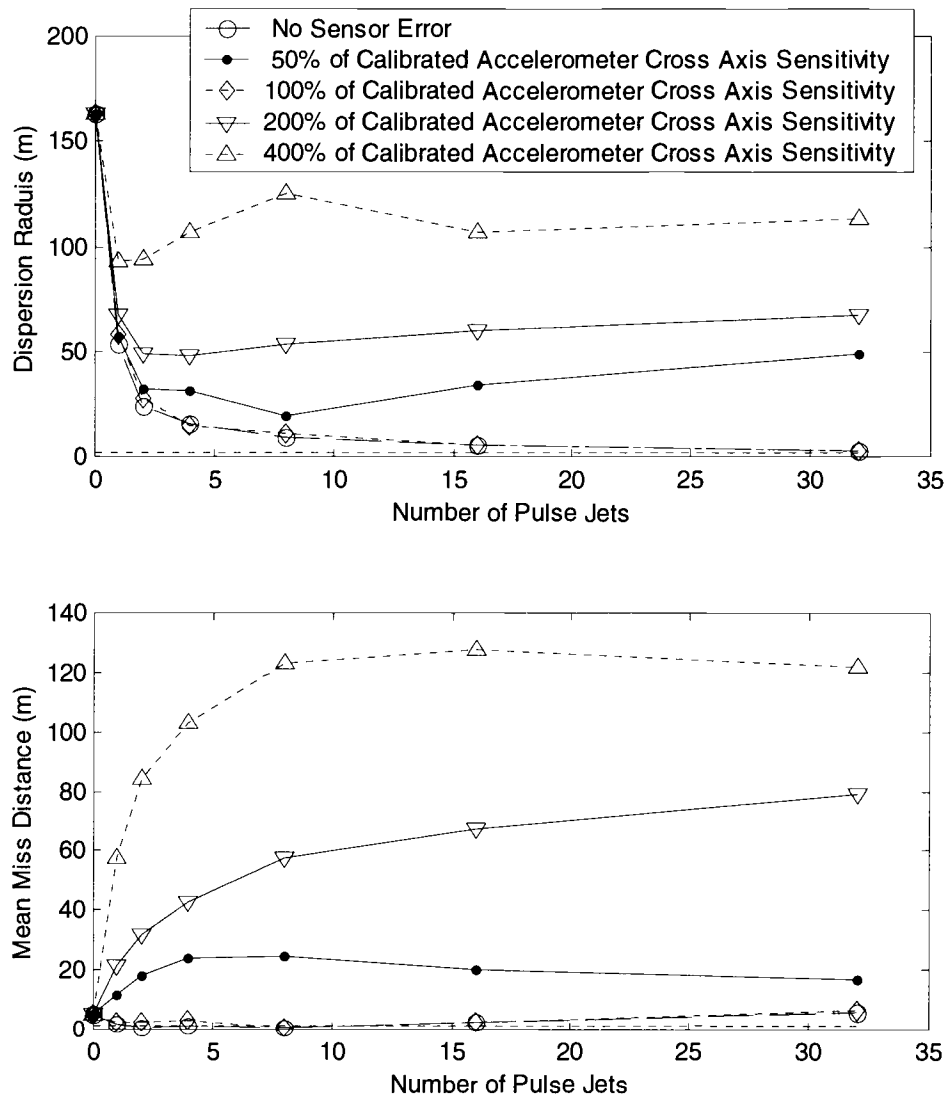

Figure 6.18 Effect of Accelerometer Cross Axis Sensitivity on Three Triaxial Accelerometer Method.

6.3.3 Sensor Errors in the Unconventional IMU Using Skin Mounted Sensor Fusion Algorithm

An array of 32 triaxial accelerometers, configured in 4 sensor rings with 8 accelerometers on each ring are mounted on the surface near the nose of the rocket. The first ring is 0.762 m from the rear end. Each ring are separated by 76.2 mm. The angular rates are determined using algorithm described in Section 4.4. In the determination of the acceleration at the IMU location, a set of accelerometers at the IMU point is calculated from each individual accelerometer. The averaged number from this set is then used in the IMU equation. The results from Figure 6.19, 6.20, and 6.21 show that the dispersion radius is sensitive to accelerometer noise, bias and the cross axis sensitivity. The dispersion radius and the mean miss distance increase as accelerometer noise increases. This increasing level is higher than in the three points method. However, when considering the effect of errors in the cross axis sensitivity, the mean miss distance increasing level in the sensor fusion method is less than in the three points method. It should be noted that the sensors in this algorithm resemble the O configuration mentioned in Section 4.3. The extensive study in Section 4.3 concludes that this configuration yields higher sensitive to the noise than those with the T and L configurations.

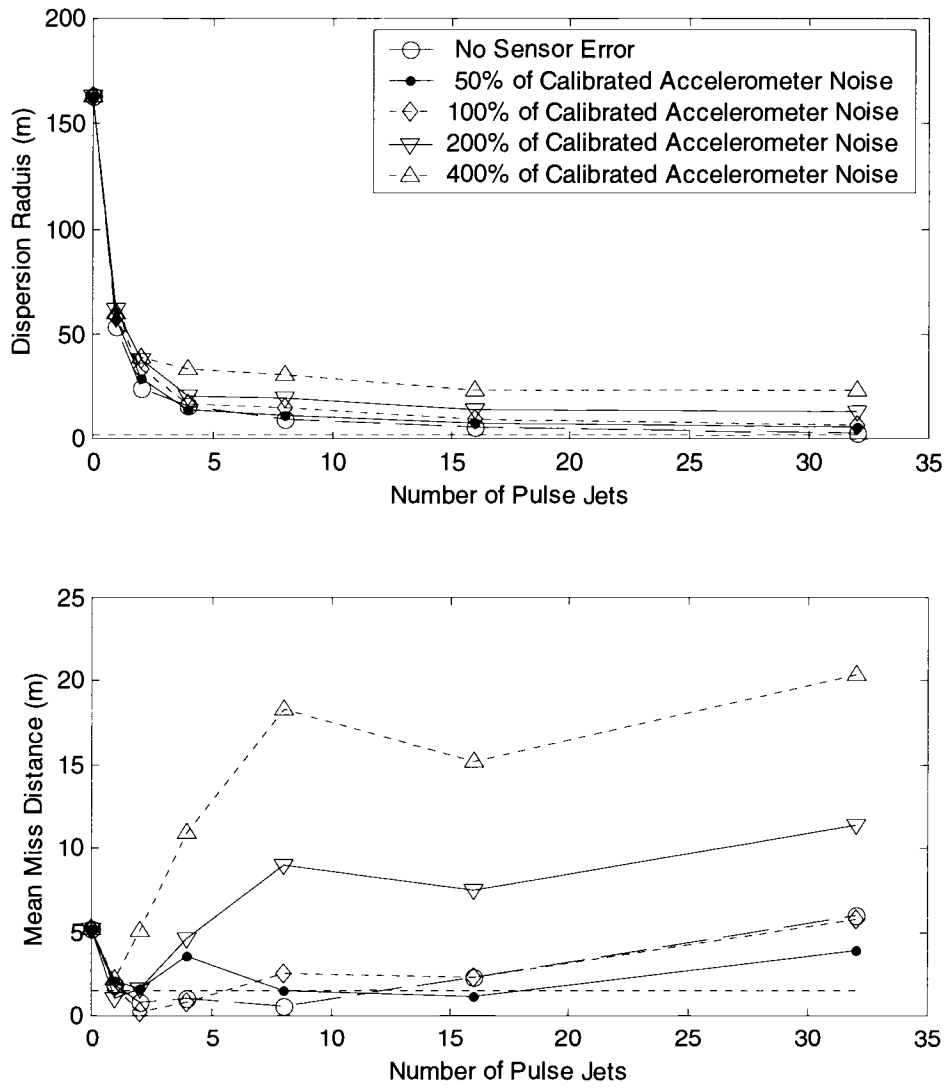

Figure 6.19 Effect of Accelerometer Noise on Skin Mounted Sensor Fusion Method.

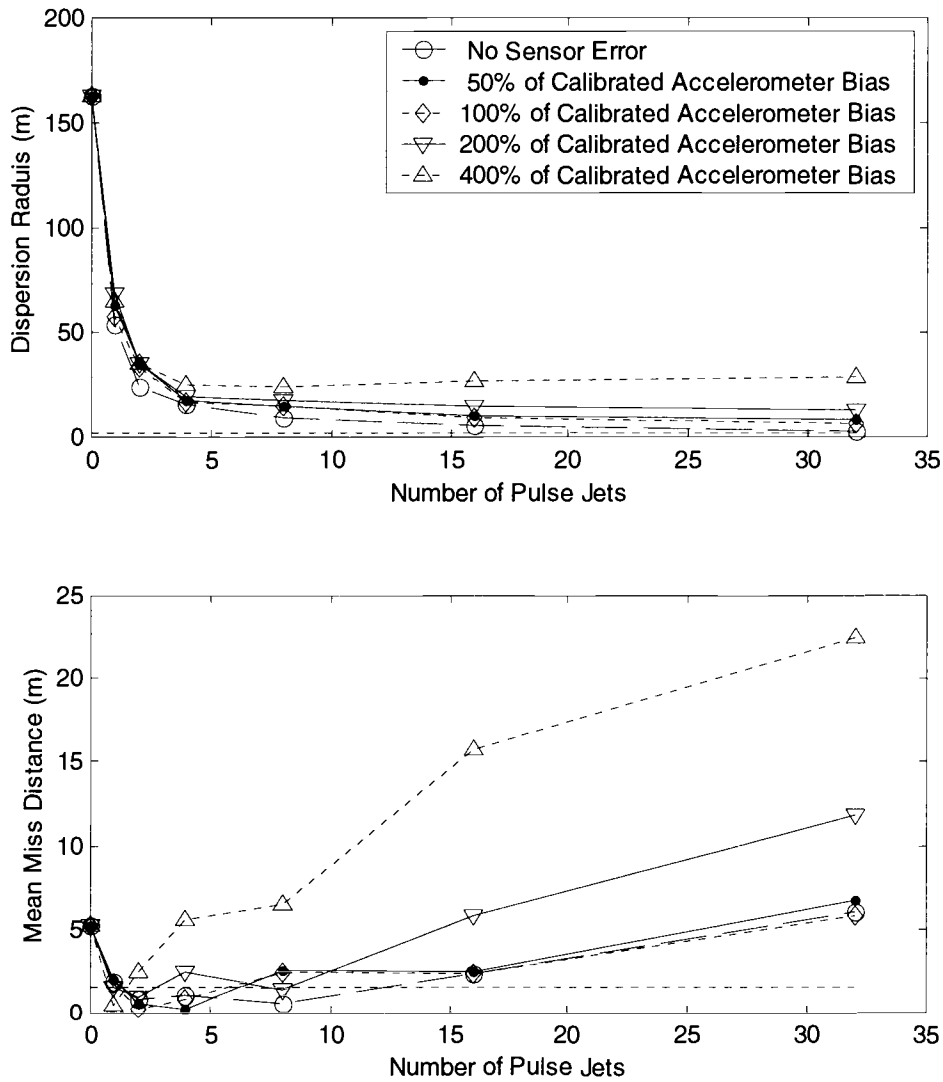

Figure 6.20 Effect of Accelerometer Bias on Skin Mounted Sensor Fusion Method.

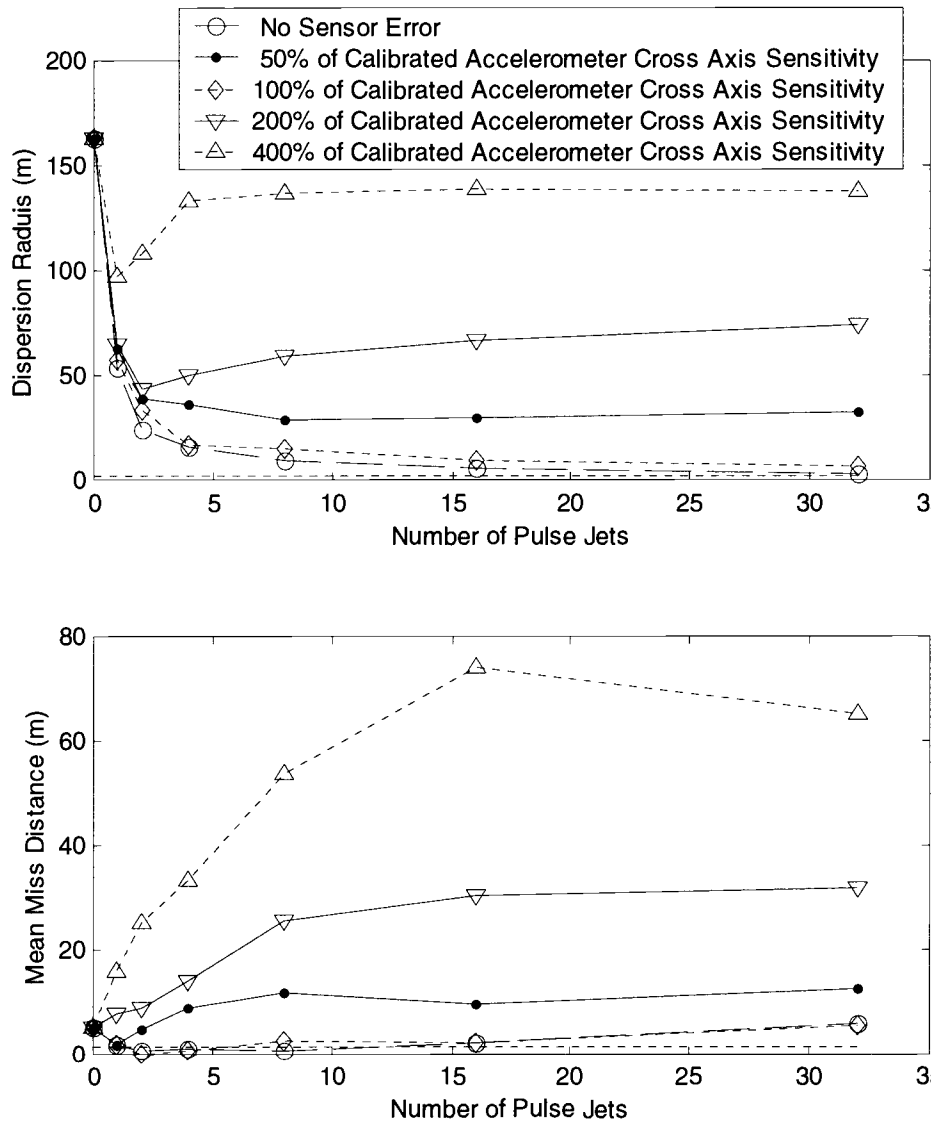

Figure 6.21 Effect of Accelerometer Cross Axis Sensitivity in Skin Mounted Sensor Fusion Method.

CHAPTER 7
CONCLUSIONS

7.1 Conclusions

A Flight control consisting of a lateral pulse jet control mechanism coupled to a flight control law and sensor suite is developed for a direct fire atmospheric rocket. Substantial reduction in impact point dispersion and inaccuracy of the controlled rocket is demonstrated using six degree of freedom model.

In designing the pulse jet control mechanism with a trajectory tracking control law, the tracking window size must be carefully selected in concert with the jet magnitude and number of pulse jets. A certain amount of individual pulse jet impulse amplitude is required in order to reduce the dispersion radius sufficiently. However, if the pulse jet impulse is too big and the tracking window size is improperly selected, the fired pulse jet will over correct the trajectory. The developed trajectory tracking control law and the considered parabolic and proportional navigation guidance law perform suitably with the lateral pulse jet control mechanism. The parabolic and proportional navigation provides least dispersion radius when large number of pulse jet is used. However, it increases the mean miss distance when small amount of pulse jets is configured on the rocket. The trajectory tracking control law consisting generates impact patterns nearly centered to the target in all range of the pulse jet numbers.

Sensor suite is a key component of the smart weapon control system. In using a conventional inertial measurement unit (IMU) in the flight control system, the control performance is more sensitive to the errors from gyroscopes than to the accelerometers, especially in mean miss distance. Unlike the sensor noise and bias

that their effects of on the dispersion radius are less severe, the errors in sensor cross axis sensitivity contributes more effect to the control performance.

A new, unconventional IMU that utilizes a combination of linear accelerometers in the estimation of angular velocity and angular acceleration is developed. The results are comparative to the estimation from gyroscopes. For the case where triaxial components of linear acceleration is known at three non colinear points, the kinematic equations must in general be transformed to a computational plane before a useful solution is obtained. In the application of the three points method to a skin mounted triaxial accelerometer sensor fusion, a solution is obtained without the need to transform the kinematic equations to a computational plane.

The sensitivity of the estimated angular rate to acceleration measurement in the three triaxial accelerometers method reduces with increasing rocket roll rates. This sensitivity also depends on how the accelerometers configured in the computational plane. The L configuration provides least sensitivity among the considered geometric configurations while worst case is found in the O configuration. In the skin mounted triaxial acceleration method, the most effective method to fuse the data is with one cluster that contains all the sensors. The use of many accelerometers fused in the estimation does not guarantee to reduce the sensitivity of the control performance to the errors. The selection of constellation among accelerometers in the data fusion process must be carefully taken into account. In all method the cross axis sensitivity contributes more effect to the control performance than the sensor noise and bias.

7.2 Recommendations for the Future Research

The research in the pulse jet control leaves variety of area open to be improved that includes:

1. A realistic model of the lateral pulse jet mechanism. Results from aerodynamic research in the interaction of the lateral jet to high velocity airflow should be applied to the pulse jet model, for example, the include of jet amplification factor as a function of rocket's Mach number and angle of attack.

2. The possibility of improving the trajectory tracking control scheme should be explored. For example, adaptive tracking window size as a function of rocket Mach's number and angle of attack should be applied in concert with the realistic pulse jet amplitude model.

3. More exploration on the sensor errors to the flight control system. Miss alignment and error in dimension of sensor locations should be included in the analysis by studying effects of errors in the $[T_{Ai}]$ and $[T_{Gi}]$ sensor matrices in the IMU model.

4. A technique that combines knowledge from the error analysis in various sensor configurations to the skin mounted sensor fusion should be established. For example, the selection of accelerometer group to form the relative acceleration matrix, A, and the relative position matrix, R, in the sensor fusion process should be done in the L configuration manner.

BIBLIOGRAPHY

Bellamy, R., Chase, W., and Whiteside, J. "Accuracy Analysis for the 2.75-inch MK66 Rocket." FTB-IR-23, U.S. Army Research, Development, and Engineering Center. Picatinny Arsenal, New Jersey, 1995.

Blakelock, J.H. Automatic Control of Aircraft and Missiles. Jon Wiley & Son, Inc., 1991.

Brandeis, J., and Gill, J. "Experimental Investigation of Super and Hupersonic Jet Interaction of Missile Configurations." Journal of Spacecraft and Rockets. Vol.35, No.3, May-June 1998.

Calise A. J. and El-Shirbiny, H.A. "An Analysis of Aerodynamic Control for Direct Fire Spinning Projectiles." Proceedings of the 2001 AIAA Guidance, Navigation, and Control Conference. Montreal, Canada, Paper Number AIAA 2001-4217, 2001.

Carter, R., Chase, W., and Whiteside, J. "Accuracy Analysis for the Advanced Rocket System." FTB-IR-14, U.S. Army Research, Development, and Engineering Center. Picatinny Arsenal, New Jersey, 1994.

Champigny, P., and Lacau, R.G. "Lateral Jet Control for Tactical Missiles." AGARD Special Course on Missile Aerodynamics. June 1984.

Costello, M.F. "Range Extension and Accuracy Improvement of an Advanced Projectile Using Canard Control." Proceedings of the 1995 AIAA Atmospheric Flight Mechanics Conference. Baltimore, MD, 1995.

Costello, M., and Anderson, D. "Effect of Internal Mass Unbalance on the Terminal Accuracy and Stability of a Projectile." Proceedings of the 1996 AIAA Flight Mechanics Conference. San Diego, CA, 1996.

Costello, M., and Agarwalla, R. "Improved Dispersion of a Fin-Stabilized Projectile Using a Passive Movable Nose." Journal of Guidance, Control, and Dynamics. Vol.23, No.5, September-October 2000.

Costello, M., and Jitpraphai, T. "Determining Angular Velocity and Angular Acceleration of a Projectile using Triaxial Acceleration Measurements." AIAA Atmospheric Flight Mechanics Conference, Denver, AIAA Paper 2000-4193, August 14-17, 2000.

D'Amico, W. "Revolutionary Technologies for Miniature Measurement Systems – Applications to Ground Testing." 36th Aerospace Sciences Meeting and Exhibit. Reno, NV, Paper Number 98-0234, 1998.

Davis. B.S. "Using Low Cost MEMS Accelerometers and Gyroscopes as Strapdown IMUs on Rolling Projectiles." 1998 IEEE Position, Location, and Navigation Symposium. Volume 1, Number 1, 1996.

Davis, B., Harkins, T., and Burke, L. "Flight Test Results of Miniature, Low-Cost, Spin, Accelerometer, and Yaw Sensors." 35th Aerospace Sciences Meeting and Exhibit. Reno, NV, Paper Number 97-0422, 1997.

Etkin, B. Dynamics of Atmospheric Flights. Wiley, John & Sons, Inc., NewYork, 1972.

Garnell, P. Guided Weapon Control Systems. 2nd.ed., Pergamon Press, 1980.

Gast, R., Morris, S., and Costello, M. "Simulation of Shot Impacts for the M1A1 Tank Gun." Journal of Guidance, Control, and Dynamics. Vol.23, No.1, 2000.

Genin, J., Hong, J., and Xu, W. "Accelerometer Placement for Angular Velocity Determination." ASME Journal of Dynamic Systems, Measurement, and Control. Vol. 119, 1997.

Gilman, B.G.. "Control Jet Interaction Investigation." Journal of Spacecraft. Vol.8, No.4, April 1971.

Ginsberg J. H. "Advanced Engineering Dynamics." Cambridge University Press. U.S.A., 1995.

Harkins, T.E., and Brown, T.G. "Practicability Issues in Deriving Angular Rates from Accelerometer Data for the 2.75" MK66 Rocket." U.S. Army Research Laboratory Technical Report. Aberdeen Proving Ground, ARL-MR-392, February 1998.

Harkins, T.E., Brown, T.G. "Using Active Damping as a Precision-Enhancing Technology for 2.75-Inch Rockets." U.S. Army Research Laboratory, Aberdeen Proving Ground. MD, ARL-TR-1772, 1999.

Jitpraphai, T. and Costello, M. "Dispersion Reduction of a Direct Fire Rocket Using Lateral Pulse Jets." Journal of Spacecraft and Rocket. Vol.38, No.5, 2001.

Kuo, C.Y., and Chiou, Y.C. "Geometric Analysis of Missile Guidance Command." IEEE Proc. – Control Theory Appl. Vol. 147, No. 2, March 2000.

Kurita, M., Okada, T., and Nakamura, Y. "The Effects of Attack Angle on Aerodynamics Interaction due to Side Jet from a Blunted Body in a Supersonic Flow." AIAA 39th Aerospace Sciences Meeting & Exhibit. AIAA Paper 2001-0261, Reno, 2001.

Liaw, D.C., Liang, Y-W., and Cheng, C-C. "Nonlinear Control for Missile Terminal Guidance." Journal of Dynamic Systems, Measurement, and Control. Vol. 122, December 2000.

Lim, T.W. "Sensor Placement for On-Orbit Modal Testing." Journal of Spacecraft and Rockets. Vol. 29 No.2, March 1992.

Merhav, S.J. "A Nongyroscopic Inertial Measurement Unit." Journal of Guidance. Vol.5, No.3, May-June 1982.

Nusholtz, G.S. "Geometric Methods in Determining Rigid Body Dynamics." Experimental Mechanics. Vol.33, No.2, 1993.

Padgaonkar, A.J., Krieger, K.W., and King, A.I. "Measurement of Angular Acceleration of a Rigid Body Using Linear Accelerometers." ASME Journal of Applied Mechanics. 1975.

Reinecke, W.G. "Penetration of a Lateral Sonic Gas Jet into a Hypersonic Stream." AIAA Journal. Vol.13, No.2, February 1975.

Rodriguez, A.A., and Sonne, M.L. "Evaluation of MissileGuidance and Control Systems on a Personal Computer." SIMULATION. June 1997.

Schuler, A. Grammatikos, A., and Fegley, K. "Measuring Rotational Motion with Linear Accelerometers." IEEE Journal of Aerospace and Electronic Systems. AES-3, May 1967.

Shin, Y.J. "Linearized Common Curvature Guidance Law for Homing Missiles." Proceedings of the American Control Conference. Albuquerque, New Mexico, June 1997.

Spaid, F.W., and Zukoski, E.E. "A Study if the Interaction of Gaseous Jets from Transverse Slots with Supersonic External Flows." AIAA Journal. Vol.6, No.2, February 1968.

Spaid, F.W. "Two-Dimensional Jet Interaction Studies at Large Values of Reynolds and Mach Numbers." AIAA Journal. Vol.13, No.11, November 1975.

Srivastava, B. "Computational Analysis and Validation for Lateral Jet Controlled Missiles." Journal of Spacecraft and Rockets. Vol.34, No.5, September-October 1997.

Srivastava, B. "Lateral Jet Control of a Supersonic Missile: Computational and Experimental Comparisons." Journal of Spacecraft and Rockets. Vol.35, No.2, March-April 1998.

Srivastava, B. "Asymmetric Divert Jet Performance of a Supersonic Missile: Computational and Experimental Comparisons." Journal of Spacecraft and Rockets. Vol.36, No.5, Septamber-October 1999.

Stoer, J. and Burlirsh, R. Introduction to Numerical Analysis. Springer-Verlag, NewYork, 1992.

Wang J., Xie, X., and Zhong, Y. "H∞ Controller Design of a Missile Cuidance and Control System." Proceedings of the American Control Conference. Albuqerque, New Maxico, June 1997.

Zarchan, P. "Tactical and Strategic Missile Guidance." Progress in Astronautics and Aeronautic. Vol. 124, American Institute of Aeronautics and Astronautics, Inc., Washington D.C., 1990.